

UNIVERSIDADE DE SÃO PAULO


Instituto de Física

## Emaranhamento multicolor para conexão de sistemas quânticos

Túlio Brito Brasil

Orientador: Marcelo Martinelli

Coorientador: Eugene Polzik (Universidade de Copenhague)



Tese de doutorado apresentada ao Instituto de Física da Universidade de São Paulo, como requisito parcial para a obtenção do título de Doutor em Ciências.

Banca Examinadora:

Prof. Dr. Marcelo Martinelli (Orientador) - Universidade de São Paulo

Prof. Dr. Cristiano Luis Pinto de Oliveira - Universidade de São Paulo

Prof. Dr. Gustavo Silva Wiederhecker - Universidade Estadual de Campinas

Prof. Dr. Alessandro Zavatta - Istituto Nazionale di Ottica

Prof. Dr. Ulrik Lund Andersen - Danmarks Tekniske Universitet

SÃO PAULO

2021

**FICHA CATALOGRÁFICA**  
**Preparada pelo Serviço de Biblioteca e Informação**  
**do Instituto de Física da Universidade de São Paulo**

Brasil, Túlio Brito

Emaranhamento, Oscilador paramétrico ótico, redes quânticas.  
São Paulo, 2021.

Tese (Doutorado) – Universidade de São Paulo, Instituto de Física,  
Depto. de Física Experimental

Orientador: Prof. Dr. Marcelo Martinelli

Área de Concentração: Ótica quântica

Unitermos: 1. Emaranhamento; 2. Oscilador paramétrico ótico; 3.  
Redes quânticas

USP/IF/SBI-027/2021

**UNIVERSITY OF SÃO PAULO**  
Physics Institute

**Multicolor entanglement to link quantum systems**

**Túlio Brito Brasil**

Supervisor: Marcelo Martinelli (University of São Paulo)

Co-supervisor: Eugene Polzik (University of Copenhagen)

Thesis submitted to the Physics Institute of the University of São Paulo in partial fulfillment of the requirements for the degree of Doctor of Science.

Examining Committee:

Prof. Dr. Marcelo Martinelli (Supervisor) - University of São Paulo

Prof. Dr. Cristiano Luis Pinto de Oliveira - University of São Paulo

Prof. Dr. Gustavo Silva Wiederhecker - University of Campinas

Prof. Dr. Alessandro Zavatta - Istituto Nazionale di Ottica

Prof. Dr. Ulrik Lund Andersen - Danmarks Tekniske Universitet

SÃO PAULO

2021

*To the small boy that once dreamed to be a scientist*



# Acknowledgements

I want to say thanks to my supervisor Marcelo Martinelli for the support over all the 7 years we worked together. It was a long self-discover-scientific journey from no experience in the lab, when I just started my masters at LMCAL, to today. This thesis wouldn't exist without all the "watch and learn" moments I had with you.

Paulo Nussenzeig, my second supervisor — never on paper but always in mind — also had a major impact on my career. I'm thankful for the counseling and advice on science in general.

To my co-supervisor, Eugene Polzik, I'm greatly in debt. It is a pleasure to work with you and be part of your team. I'm thankful for your mentorship.

In Brazil I had the opportunity to work with amazing people. At LMCAL I made true friends. To mention some of those I interacted more closely I would like to point: Renné Medeiros, Breno Teixeira, Ashok Kumar, Rayssa Bruzaca, Igor Konieczniak, Klara Theophilo, Carlos Gonzalez, Renato Ribeiro, Roger Kögler, Luiz Couto, Felipe Gewers, Alvaro Montaña, Raúl Rincón, Harold Rojas, Pablo Palácios, Barbara Ribeiro and Lucas Nunes.

When I moved to Denmark I also encountered a warm working environment. At QUANTOP I found a great diversity of colleagues from which I could learn a lot. I would like to mention and thank the interactions with: Valerii Novikov, Jun Jia, Ryan Yde, Jorg Muller, Jurgen Appel, Emil Zeuthen, Rodrigo Thomas, Ivan Galinskiy, Jonas Mathiassen, Christoffer Møller, Yeghishe Tsaturyan, Michal Parniak, Anders Simonsen, Michael Zugenmaier, Karsten Dideriksen, Christoffer Østfeldt, Rebecca Schmiege, Georg Enzian, Hans Stærkind, Signe Markussen, Jacob Hansen and Timo Zwettler.

The GWD project is in collaboration with the Danish Institute of Metrology (DFM). I want to say thanks to Mikael Østergaard Lassen and Hugo Kerdoncuff for the discussions.

I want to acknowledge support of University of São Paulo and University of Copenhagen. This study was financed in part by the Coordenação de Aperfeiçoamento de Pessoal de Nível Superior - Brasil (CAPES) - Finance Code 001. Also, this work was partially financed by the Conselho Nacional de Desenvolvimento Científico e Tecnológico (CNPq).



# Abstract

Light-matter interaction is a toolbox used to link, entangle, probe, and manipulate quantum systems. To power new quantum technologies, it's necessary to create entangled states where their unique correlations can be explored to gain advantages not allowed in classical physics. Furthermore, different systems need to interact with each other to leverage their strengths in performing specific tasks. Naturally, we face the challenge of creating entanglement between different electromagnetic spectrum ranges to build quantum hardware that is not limited to a particular system with one input/output port.

In this thesis, we explore the Optical Parametric Oscillator (OPO) as a source of multicolor entangled states. The OPO is a nonlinear optical device commonly used in quantum optics; is often used in simple monochromatic operations, but working on multicolor configurations reveals relevant possible applications. We study two of these conditions where multicolor entanglement is a promising resource.

- Two-color entanglement for quantum noise evasion in interferometric Gravitational Wave Detectors (GWD), as required in the proposal [1]. Generating entangled vacuum states at 1064 nm and 852 nm in sidebands down to audio frequencies, the OPO connects the interferometer and an ensemble of Cesium atoms. In this protocol, a negative mass reference frame formed by the atomic spin ensemble is used to overcome the quantum noise in the measured gravitational wave signal.

- Three-color entanglement for a quantum network between Rubidium atoms and silicon photonics. New technologies to achieve scalability have to be miniaturized, and this project addresses quantum networks to the realm of silicon photonics. Obtaining entanglement between wavelengths compatible with rubidium atoms (D1 line 795 nm) and CMOS technology (1608 nm), we pursue the idea to perform quantum teleportation protocols on-chip.

As a result for the first goal, we violate the separability criterion:  $\text{Var}[\hat{X}_-] + \text{Var}[\hat{Y}_+] \approx 0.32 < 2$ , down to 350 kHz. To the best of our knowledge, it corresponds to the highest two-color entanglement measured in continuous variables. This is the first step into the implementation of a link between a GWD and an atomic ensemble. As a result, calculations show that 6 dB sensitivity gain can be achieved.

Regarding the second goal, we obtain the OPO classical parameters. For the above oscillation threshold operation, phase noise that depends on temperature and intracavity power deteriorates three-color entanglement. We mitigate these contributions by obtaining phase matching for 795 nm and 1608 nm at temperature  $\approx -43^\circ\text{C}$  and an oscillation threshold of 5 mW. These results promise to solve long-standing technical problems that were limiting our group's earlier works to achieve an atom-light quantum interface.

**Keywords:** entanglement; optical parametric oscillator; quantum networks.



# Resumo

A interação luz-matéria é uma ferramenta usada para conectar, emaranhar, sondar e manipular sistemas quânticos. Para potencializar novas tecnologias quânticas, é necessário criar estados emaranhados, onde suas correlações exclusivas podem ser exploradas para obter vantagens que não são permitidas na física clássica. Além disso, diferentes sistemas precisam interagir uns com os outros para alavancar seus pontos fortes na execução de tarefas específicas. Naturalmente, enfrentamos o desafio de criar emaranhamento entre diferentes faixas do espectro eletromagnético para construir hardware quântico que não se limite a um sistema específico com uma porta de entrada/saída.

Nesta tese, exploramos o Oscilador Paramétrico Ótico (OPO) como uma fonte de estados emaranhados multicolor. O OPO é um dispositivo óptico não linear comumente usado em óptica quântica; no entanto, devido à complexidade envolvida na medição de correlações quânticas entre cores diferentes, a abordagem usual concentra-se em uma operação de estado monocromático. Estudamos duas condições onde o uso de emaranhamento multicolor é um recurso promissor:

- Emaranhamento de duas cores para redução de ruído quântico em interferômetros detectores de ondas gravitacionais (GWD), conforme requerido na proposta [1]. Gerando estados de vácuo emaranhados em 1064 nm e 852 nm com bandas laterais até frequências de áudio, o OPO fornece a conexão entre o interferômetro e um conjunto de átomos de césio. Neste protocolo, um referencial de massa negativa formado pelo conjunto de spin atômico é usado para remover o ruído quântico no sinal de onda gravitacional medido.

- Emaranhamento de três cores para uma rede quântica entre átomos de rubídio e fotônica de silício. Novas tecnologias para alcançar escalabilidade precisam ser miniaturizadas e este projeto direciona redes quânticas para o reino da fotônica de silício. Obtendo o emaranhamento entre comprimentos de onda compatíveis com átomos de rubídio (linha D1 795 nm) e tecnologia CMOS (1608 nm), buscamos a ideia de realizar protocolos de teletransporte quântico em chip.

Como resultado da primeira meta, violamos os critérios de separabilidade:  $\text{Var} [\hat{X}_-] + \text{Var} [\hat{Y}_+] \approx 0,32 < 2$ , até 350 kHz. Até onde sabemos, corresponde ao mais alto emaranhamento de cores distintas medido em variáveis contínuas. Este é o primeiro passo para a implementação de um link entre um GWD e um conjunto atômico. Usando esse resultado, os cálculos mostram que um ganho de sensibilidade de 6 dB pode ser alcançado.

Em relação ao segundo objetivo, obtemos os parâmetros clássicos do OPO. Para a operação acima do limiar de oscilação, o ruído de fase que depende da temperatura e da potência intracavidade deteriora o emaranhamento de três cores. Mitigamos essas contribuições obtendo casamento de fase para 795 nm e 1608 nm na temperatura  $\approx -43$  °C e um limiar de oscilação de 5 mW. Esses resultados prometem resolver problemas técnicos de longa data que estavam limitando trabalhos anteriores de nosso grupo para alcançar uma interface quântica átomo-luz.

**Palavras-chave:** emaranhamento; oscilador paramétrico ótico; redes quânticas.





# List of Figures

2.1	EPR paradox framework. . . . .	9
2.2	Representation of a coherent state in phase space. . . . .	16
2.3	Phase space representation of a squeezed coherent state. . . . .	18
2.4	Field fluctuation $\delta\alpha$ decomposed in terms amplitude and phase. . . . .	22
2.5	Balanced homodyne detection scheme. . . . .	23
2.6	Basic teleportation scheme. . . . .	24
3.1	Output power and efficiency in function of $\sigma$ . . . . .	32
3.2	Violation of the Duan criteria for signal and idler. . . . .	34
3.3	$V_1$ and $V_0$ in function of $\sigma$ and $\Omega'$ . . . . .	34
3.5	Mixing two fields with frequency and spatial mode in different polarizations. . . . .	36
3.6	Duan criterion for the Stokes operators for different values of the parameter $K$ . . . . .	37
3.7	NOPO cavity model. . . . .	39
3.8	Phasor diagram of parametric down-conversion. . . . .	41
4.1	Building blocks of the two-color entanglement source. . . . .	45
4.2	The 1064 light setup. . . . .	46
4.3	Measurements of amplitude noise of the Mephisto laser. a) From 0 Hz to 1.5 kHz, using the Stanford Research Systems SR780 FFT analyser. b) From 50 kHz to 2 MHz, using the Agilent E4405B spectrum analyser. The measured input power is $\approx 0.2$ mW. . . . .	47
4.4	The 852 light setup. . . . .	48
4.5	Relaxation oscillation and pump noise . . . . .	48
4.6	Sostis laser amplitude noise normalized to shot noise for frequencies from 0 Hz to 1 kHz (pump power = 10 W). . . . .	49
4.7	Sostis laser amplitude noise normalized to shot noise for frequencies from 0 Hz to 12 kHz (pump power = 10 W). . . . .	49
4.8	Picture of our PPKTP . . . . .	50
4.9	Wavelength phase matching vs temperature. . . . .	51
4.10	Pictorial scheme of the SFG and SPDC. . . . .	51
4.11	The SFG setup. . . . .	52
4.12	SFG phase matching vs temperature . . . . .	53
4.13	SFG efficiency measurements. . . . .	53
4.14	Bow-tie cavity scheme. . . . .	54
4.15	Waist size between the curved mirror and between the plane mirrors in the bow-tie cavity. . . . .	55
4.16	Horizontal and vertical waist sizes for a fixed distance $d_p = 347$ mm. . . . .	55
4.17	High order mode spacing for different cavity sizes. . . . .	56
4.18	Assembled optical parametric oscillator. . . . .	58
4.19	Measurement of reflection dip for spurious loss estimate. . . . .	59



4.20	Picture of the experimental setup for two-color EPR-state. . . . .	60
4.21	Experimental setup for EPR entanglement measurements. . . . .	60
4.22	Example of lock for one of the OPO wavelengths . . . . .	61
4.23	Picture of the experimental setup for two-color EPR-state. . . . .	61
4.24	Measurement of the parametric gain for different pump powers. . . . .	62
4.25	Entanglement measurement between 1064 nm and 852 nm. . . . .	63
4.26	Entanglement measurement between 1064 nm and 852 nm. . . . .	64
4.27	Squeezing measurement for different pump powers. . . . .	65
5.1	SNLO simulation of output wavelengths in function of poling period. . . . .	70
5.2	SNLO simulation of output wavelengths in function of the temperature. . . . .	71
5.3	Linear optical cavity with a nonlinear crystal. . . . .	72
5.4	Input mirror transmission and output mirror transmission spectrum. . . . .	73
5.5	Simulation of the oscillation threshold for a TROPO . . . . .	74
5.6	Assembled TROPO. . . . .	75
5.7	Transmission through the received PPKTP crystal (Raicol #1). . . . .	75
5.8	Reflection of the two surfaces of the crystal in function of the wavelength (Raicol #2). . . . .	76
5.9	TROPO output in function of crystal temperature . . . . .	77
5.10	TROPO threshold power in function of the signal wavelength. . . . .	77
5.11	TROPO signal wavelengths output in function of crystal temperature. . . . .	78
A.1	Representations of amplitude modulation. . . . .	86
A.2	Representations of phase modulation. . . . .	87
B.1	Intensity distribution of few Hermite-Gauss modes. . . . .	90
B.2	Main parameters of a Gaussian mode. . . . .	90
B.3	Mode matching example. . . . .	91
C.1	Graphic representations of the phase matching conditions. . . . .	95
C.2	Second harmonic generation process with QPM. . . . .	97
C.3	Kleinman-Boyd function $h_m(B, \xi)$ . . . . .	98

# List of Tables

4.1	Comparing the Mephisto laser to Mephisto + Nufern amplifier. . . . .	46
4.2	Sprout and Solstis main parameters. . . . .	47
4.3	PPKTP main parameters. . . . .	50
4.4	Parts used in the OPO construction . . . . .	57
4.5	Estimated efficiencies in the experimental setup. . . . .	63
5.1	LWE-142 and Diablo main parameters. . . . .	69



# Glossary

## Acronyms

**OPO:** Optical Parametric Oscillator  
**OPA:** Optical Parametric Amplifier  
**DOPO:** Degenerated Optical Parametric Oscillator  
**NOPO:** Nondegenerated Optical Parametric Oscillator  
**EPR:** Einstein-Podolsky-Rosen  
**GWD:** Gravitational Wave Detector  
**PZT:** Piezoelectric Transducer  
**HOM:** High-Order Mode  
**MM:** Mode Matching  
**RBW:** Resolution Bandwidth  
**VBW:** Video Bandwidth  
**PDH:** Pound-Drever-Hall  
**HD:** Homodyne Detector  
**SFG:** Sum-Frequency Generation  
**FSR:** Free Spectral Range  
**PPKTP:** Periodically Polled KTP  
**TEM:** Transverse Electromagnetic Mode  
**PBS:** Polarizing Beam Splitter  
**BS:** Beam Splitter  
**KTP:** Potassium Titanyl Phosphate ( $\text{KTiOPO}_4$ )  
**SQZ:** Squeezing  
**AR:** Antireflectivity  
**HR:** High Reflectivity  
**PID:** Proportional-Integral-Differential  
**ROC:** Radius of Curvature  
**SQZ:** Squeezing  
**ASQZ:** Antisqueezing  
**TEC:** Thermoelectric Cooler  
**PSD:** Power Spectrum Density  
**CM:** Covariance Matrix  
**MCC:** Mode Cleaner Cavity

## Terms

$\eta$ : efficiency of a process  
 $\alpha$ : amplitude of a coherent field  $|\alpha\rangle$   
 $\gamma$ : cavity decay rate

$\gamma'$ : total cavity decay rate

$\text{Var}[\hat{o}]$ : variance of an operator  $\hat{o}$

$\sigma$ : pump power normalized by oscillation threshold power

$\Omega$ : sideband frequency

$\omega$ : laser carrier frequency

$\Delta$ : cavity detuning

$w$ : waist size

$\mathcal{F}$ : cavity finesse

$\delta\nu$ : cavity bandwidth

$\Delta\nu$ : cavity free spectral range

$\lambda$ : laser wavelength

$\hat{\rho}$ : density operator describing a quantum state

$\mathcal{G}$ : parametric gain

# Contents

<b>1</b>	<b>Introduction</b>	<b>1</b>
1.1	Two-color entanglement for quantum noise evasion . . . . .	2
1.2	Entanglement for quantum networks . . . . .	3
1.3	Thesis structure . . . . .	4
<b>I</b>	<b>Basic concepts</b>	<b>7</b>
<b>2</b>	<b>Entanglement of light modes</b>	<b>9</b>
2.1	The Einstein-Podolsky-Rosen paradox . . . . .	9
2.2	Entanglement formal definition . . . . .	10
2.3	Entanglement criteria . . . . .	10
2.3.1	Sum of variances: bipartite case . . . . .	11
2.3.2	Sum of variances: tripartite case . . . . .	11
2.4	Electromagnetic field operators . . . . .	12
2.5	States and representations . . . . .	14
2.5.1	Fock states . . . . .	14
2.5.2	Quadrature states . . . . .	15
2.5.3	Coherent states . . . . .	15
2.5.4	Squeezed states . . . . .	17
2.5.5	The Wigner function . . . . .	17
2.6	Gaussian states . . . . .	20
2.6.1	Symplectic transformations . . . . .	20
2.7	Noise measurement techniques . . . . .	21
2.8	Homodyne detection . . . . .	23
2.9	Quantum teleportation . . . . .	24
2.9.1	Quantum teleportation in CV . . . . .	25
<b>3</b>	<b>Optical Parametric Oscillator</b>	<b>27</b>
3.1	Quantum description of OPOs . . . . .	27
3.1.1	Mean values . . . . .	30
3.1.2	Signal and idler output power . . . . .	31
3.1.3	Linearization . . . . .	32
3.2	Twin beams bipartite entanglement . . . . .	33
3.3	Tripartite entanglement . . . . .	33
3.4	Quantum fluctuations in polarization . . . . .	35
3.5	Phonon noise . . . . .	37
3.5.1	Phonon noise model . . . . .	38
3.6	Two-color entanglement source . . . . .	39

3.6.1	Nondegenerated parametric gain . . . . .	42
<b>II</b>	<b>Two-color entanglement</b>	<b>43</b>
<b>4</b>	<b>Two-color entanglement experiment</b>	<b>45</b>
4.1	Laser sources . . . . .	45
4.1.1	1064 nm light . . . . .	46
4.1.2	852 nm light . . . . .	46
4.2	The nonlinear crystal . . . . .	50
4.3	Sum-frequency generation . . . . .	50
4.4	OPO cavity design . . . . .	52
4.5	OPO assembly . . . . .	56
4.5.1	Intracavity losses . . . . .	57
4.6	Two-color setup . . . . .	59
4.6.1	Cavity locks . . . . .	59
4.6.2	Parametric gain . . . . .	59
4.6.3	Homodyne detection and estimated losses . . . . .	62
4.7	Entanglement measurements . . . . .	63
<b>III</b>	<b>Three-color entanglement</b>	<b>67</b>
<b>5</b>	<b>Towards three-color entanglement</b>	<b>69</b>
5.1	The pump laser . . . . .	69
5.1.1	The ordered PPKTP . . . . .	70
5.2	OPO cavity design . . . . .	71
5.3	Results for the received PPKTPs . . . . .	72
5.3.1	Raicol #1: coating . . . . .	72
5.3.2	Raicol # 2: coating, phase-matching, and threshold . . . . .	75
<b>6</b>	<b>Conclusion and future work</b>	<b>79</b>
	<b>Appendices</b>	<b>81</b>
<b>A</b>	<b>Light Modulation</b>	<b>83</b>
A.0.1	Oscillating functions and the simple harmonic oscillator . . . . .	83
A.0.2	Classical electromagnetical waves . . . . .	84
A.0.3	Light modulation . . . . .	85
<b>B</b>	<b>Gaussian beams and resonators</b>	<b>89</b>
<b>C</b>	<b>Nonlinear Optics</b>	<b>93</b>
C.0.1	Introduction to phase matching . . . . .	94
C.0.2	Quasi-phase matching . . . . .	96
C.1	Kleinman-Boyd parameters . . . . .	98





# Publications

- **T. B. Brasil**, V. Novikov, H. Kerdoncuff, M. Ø. Lassen, and E. S. Polzik, Generation of the two-color Einstein-Podolsky-Rosen state, *In preparation*.
- R. B. de Andrade, **T. B. Brasil**, and B. Marques, Three-color steering from an optical parametric oscillator above threshold, *In preparation*.
- H. Kerdoncuff, J. B. Christensen, **T. B. Brasil**, V. A. Novikov, E. S. Polzik, J. Hald, and M. Lassen, Cavity-enhanced sum-frequency generation of blue light with near-unity conversion efficiency, *Optics Express* **28**, 3975–3984 (2020).

## Chapter 1

# Introduction

Quantum mechanics makes predictions that could perplex those who are not familiar with its formalism [2]. The statistics of possible outcomes of a measurement are given by a density matrix  $\hat{\rho}$  — a mathematical object carrying complete information about a system [3]. When we apply the laws of quantum mechanics to composite systems, strange correlations emerge naturally. In the case of two or more systems sharing  $\hat{\rho}$ , so that we can not describe the total system by taking into account the individual states, we arrive in what is called an **entangled state**. As a consequence, predictions over one system are now conditioned on the states of other systems: no matter how far separated they are.

Einstein, Podolsky, and Rosen (EPR) first recognized the strangeness of entanglement predictions in 1935 [4]. In an attempt to complete quantum mechanics, by assuming local realism, they argue that the probabilistic outcome could be the evidence of a new theory having quantum mechanics as an approximation. They propose that this new theory would include hidden variables carrying the missing information. Finally, after Bohm supporting that a non-local theory containing hidden variables would be possible [5], John Bell in the 60's framed the path to prove that quantum mechanics nonlocal predictions are indeed correct [6], i. e. no local hidden variable theory can make the same predictions of quantum mechanics [7]. Using the ideas of Bell, several experiments showing a violation of local realism predictions were performed [8–10]. Some assumptions called "loop-holes" could still save the local hidden variable theories in the first demonstrations. However, in recent works [11], technical improvements made it possible to rule out local realism once for all [11]. Based on measurements, we know that nonlocality is part of nature.

Entanglement is a resource for new quantum technologies as quantum cryptography [12], teleportation [13], computation [14], and metrology [15]. For instance, in quantum cryptography, entanglement is used as a secure channel that forbids shared information from being hacked. Today a cryptography quantum protocol called quantum key distribution has commercial products used by banks and companies<sup>1</sup>. In quantum computers, systems in superposition and entangled process information. As a consequence, it leads to a speed-up in computational time [14]. For example, the best classical factoring algorithm uses superpolynomial time to factor the product of two primes. Shor's algorithm uses quantum mechanics to factor integers in polynomial time [18]. Because safety guaranteed in most classical cryptography protocols uses the computation work required to factorize large integers, a quantum computer large enough could jeopardize information security as we know it. We are living in an era of quantum technology.

The coherent control of robust quantum states can provide quantum information processing, but to transfer data is natural to think of light as the best candidate to carry it, because of its high speed and weak interaction with the propagation medium [19]. Still, to integrate different systems, we need quantum correlations between light in different wavelengths. The paradigm is to find the best approaches to execute specific tasks and interconnect them using multicolor quantum correlations in

---

<sup>1</sup>Notably, intercontinental quantum communication through satellites has been demonstrated [16, 17]

a network similar to a quantum internet [20], Fig. 1.1.

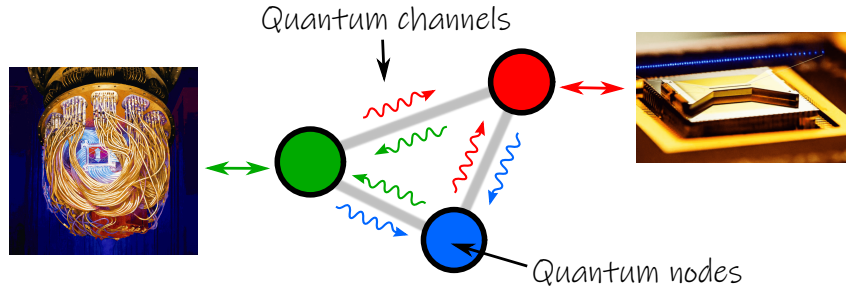


Figure 1.1: Illustration of a quantum internet. It will be composed of multicolor quantum channels connecting different nodes. Each node is one quantum hardware responsible to execute a specific quantum task.

Quantum variables are classified into continuous and discrete, according to their spectra of results. Each class has advantages and drawbacks for quantum information, as digital and analog processing in classical physics [21, 22]. We work in the continuous variables (CV) domain. In our case, the quadratures of the electromagnetic field have the same formalism of position and momentum of a particle [23]. Our system of choice to generate entanglement is the Optical Parametric Oscillator (OPO), using spontaneous parametric down-conversion process inside an optical cavity. The coupling of modes is done by the annihilation of one photon (pump) with the simultaneous creation of two photons<sup>2</sup> (signal and idler modes) resulting in a correlation among light fields. Moreover, creating a tunable quantum channel by changing the wavelengths.

In this thesis, we explore the OPO as a source of entangled states aiming to connect different quantum systems. The work is divided into two topics: two-color entanglement for quantum noise evasion in gravitational wave detectors and three-color entanglement for quantum networks. We proceed to introduce the two approaches and frame their relevance.

## 1.1 Two-color entanglement for quantum noise evasion

In interferometers used to detect gravitational waves, light monitors the motion of large mirrors that are driven by space-time ripples generated by cosmic events such as black hole collisions. The scale of displacement generated by GWs requires extreme levels of sensitivity reaching the limit where quantum effects matter [24].

From the fundamental laws of quantum mechanics, the continuous measurement of one variable imposes random disturbance in the system being measured, an effect called quantum back-action (QBA) [25]. In GWDs measurements, the motion sensitivity is dominated by the phase noise of light at high frequencies. However, if we try to reduce light phase fluctuations, it increases amplitude noise, which is the origin of the position QBA noise at low-frequencies. This is due to radiation pressure noise coming from the interaction between light and mechanics [26, 27]. We are faced with a quantum-originated short blanket problem called standard quantum limit (SQL).

Polzik and Khalili proposed to enhance the sensitivity of gravitational wave detectors beyond the SQL by measuring the signal in relation to a negative mass reference frame [1, 28]. Calculations show that broadband sensitivity improvement can be achieved with current technology. It follows from these results that the proposed scheme allows a sensitivity gain of about 6 dB across the entire sensitivity band of interest ( $< 1$  kHz), corresponding to almost an order of magnitude gain in the “visible” part of the Universe and a proportional increase in the event rate.

<sup>2</sup>The reverse process can also occur.

The proposal core includes the negative mass reference created by an atomic spin ensemble [29], and quantum correlated light at usual GWDs wavelength and light compatible with an atomic spin ensemble. We use an OPO to generate the entangled light used as the link between the interferometer and atomic spins. The OPO works to give entangled light at 1064 nm and 852 nm. For high-quality quantum correlations to be produced and detected, low-loss optical components and high quantum efficiency light detectors should be used. Also, precise control of the system parameters and isolation from noise coupling with the environment. This is a particular challenge in the low-frequency range, requiring an ultimate understanding of each part of our setup.

## 1.2 Entanglement for quantum networks

Quantum information is more sensitive to losses and decoherence than classical information. To send quantum states over long distances, we need to find ways to preserve them over inevitable losses. The non-cloning theorem says that we can not copy an unknown quantum state and build a noiseless amplifier [30]. Quantum repeaters use entanglement to overcome the lossy channel problem [31]. By breaking the task of sending a state over a long distance into several intermediary storage and entanglement swapping processes, leading to better efficiency than the simple transmission would allow [32].

This project incorporates the generation and manipulation of entangled states compatible with Rubidium transitions and telecom wavelengths. Atoms are the best candidates for quantum memories [33]. At the same time, the telecom wavelengths are optimum to be used in the new area of silicon photonics — which promises to bring scalability to optical quantum technologies — and/or be sent through optical fibers with minimal losses. Advances in silicon photonics made it the new platform for quantum technologies [34,35]. OPOs on chip [36–38] and CMOS compatible [39–41] have been demonstrated.

Our system is the ideal source of entangled states for a quantum repeater system. We have the convenience of link possible storage, processing, optimum transmission of quantum information, and scalability of quantum hardware from a single building block.

### 1.3 Thesis structure

This thesis presents results regarding two projects that share a similar theoretical framework. Details necessary to understand the main parts of the results are presented in the main body text. Some technical details are put as appendices. The thesis is structured as follows:

#### PART I: Theoretical framework

In chapter 2, we introduce the basic concepts regarding the entanglement of light modes and the EPR paradox. We define the formal definition of entanglement and present criteria to check the separability of bipartite and tripartite states. Then, we present the light operators of interest, the most common quantum states, and the Wigner representation. The Wigner function is used to define the set of Gaussian states, which comprises the kind of states this thesis focus on. To link the concepts with the experiment, we briefly describe the homodyne detection and shot noise calibration. Finally, as an application of the tools described, we analyze the essence of the quantum teleportation protocol.

In chapter 3, we describe the OPO. The triple resonant case is studied in detail, starting from the master equation that describes the dynamics of the intracavity fields. We focus on the above threshold operation, describing the classical field outputs and their quantum fluctuations. We show that the OPO produces entanglement between the twin fields and among twins and the pump beam. The conversion of quadrature entanglement into polarization entanglement is briefly explored as an alternative degree of freedom. One of the possible limitations to obtain a good degree of three-color entanglement is the phonon noise coupling to OPO output. We describe how the phonon noise couples to the phase quadrature and ways to mitigate it. Next, we describe the theory for the OPO used in the two-color experiment. We describe the quantum fluctuations in the nondegenerated OPO below the threshold and the EPR variables of interest.

#### PART II: Two-color entanglement

In chapter 5, we describe the building blocks of the two-color setup and the first experimental results obtained. The focus is on the low-frequency regime because it is the target frequency of gravitational wave detectors where the source is going to be applied. We do not try to describe how the source is going to be used in the original proposal [1, 28]. We start the chapter by presenting the laser sources used in the experiment, their amplitude noise, and overall stability. We then describe the nonlinear process of sum-frequency generation to produce the OPO pump beam. Next, the details of the cavity design to optimize the process efficiency are shown. Then, we follow characterizing the intracavity losses, describe the OPO operation, and parametric gain. Finally, the detection scheme is described, and the entanglement correlations are measured. We evaluate the amount of entanglement and the necessary steps to improve our EPR-state source.

#### PART III: Three-color entanglement

In chapter 6, the experimental setup developed for the three-color experiment is described. We present the pump laser, the nonlinear crystal characterizations, and the classical parameters for the triple resonant optical parametric oscillator. The oscillation threshold and wavelength tunability with temperature is measured.

#### Appendices

In appendix A, we introduce the framework of light modulation. The quadrature picture and how amplitude or phase modulation introduces sidebands. This is useful to define the light operators in the quantum regime.

In appendix B, the transverse modes of the electromagnetic field are presented together with the mode matching procedure.

Next, in appendix C, the basics of nonlinear optics tools are discussed. The  $\chi^{(2)}$  processes of three-wave mixing are used to introduce the phase-matching conditions. Later, the optimum focus parameters for improving the nonlinear efficiency are described. These tools are necessary for the proper design of OPOs.



## Part I

# Basic concepts





## Chapter 2

# Entanglement of light modes

This chapter introduces the main theory needed to understand the work described in this thesis, presents the notation, and standard terms used throughout the text. The term quantum correlation applies to any correlation that needs quantum theory for description. However, we understand that there are many layers of quantumness, from nonlocality to simple classical correlation. Understanding the degree and usefulness of each type is part of quantum information theory. Here we focus on describing quantum optics in continuous variables and using it to study entanglement generated by the optical parametric oscillator.

### 2.1 The Einstein–Podolsky–Rosen paradox

Unsatisfied with the implications of quantum theory, Einstein, Podolsky, and Rosen (EPR) published an article trying to show that quantum mechanics was not complete [4]. They took as premise that all physical theories should obey *local realism*, which is a composition of *reality* and *no-action-at-a-distance* premises. In their view, a complete theory is one where “every element of physical reality must have a counterpart in the physical theory” [4]. By reality, we should understand “If, without in any way disturbing a system, we can predict with certainty (i.e., with probability equal unity) the value of a physical quantity, then there exists an element of physical reality corresponding to this physical quantity” [4]. The no-action-at-a-distance says that action in a given system can not cause an immediate change in another system at a different location.



Figure 2.1: Representation of the EPR paradox. A source of EPR-states outputs two particles. One is sent to Alice and the other to Bob. Alice and Bob are two spatially separated observers that can perform measurements on their respective systems.

We may apply the local realism criteria to a system consisting of two particles separated by a distance  $L$ , with a wavefunction  $\psi(x_A, x_B) = \int \exp[i(x_A - x_B)p/\hbar]dp$  where  $x_A$  and  $x_B$  are the position of particles A and B, respectively. This state could be described, in momentum space, as  $\psi(p_A, p_B) = \int \exp[i(p_A + p_B)x/\hbar]dx$ , where  $p_A$  and  $p_B$  are the momentum of particles A and B. Choosing which quantity to measure in one system, we can predict with probability equal to unity either the position or the momentum of the other particle. But, Heisenberg’s uncertainty relations tell us that position and momentum can not have the simultaneous assignment of precise values. They, therefore, argued that quantum mechanics is correct but not complete, and the state of the particle

should be previously given by some factor that is not included in the wavefunction. As an alternative, they proposed another theory with “hidden variables” that contain information of the physical reality. This argument, sometimes called the “EPR paradox”, should be best seen as an incompatibility of quantum mechanics and local realism.

In response to the EPR article [42], Niels Bohr showed no contradiction between the quantum mechanics of composed systems and the uncertainty relations. The commutator  $[x_A - x_B, p_A + p_B] = 0$ , allows measuring the relative position and the sum of momentum with no bounded precision. But, repeated measurements of a given observable in one system show a strong dispersion in the results. The local information is necessarily degraded for the sake of the strong correlations between the individual subsystems.

## 2.2 Entanglement formal definition

The appropriate treatment of entanglement requires the density operator  $\hat{\rho}$  to describe the composed system. If a system is in a mixture of states  $|\psi_i\rangle$ , then [3]

$$\hat{\rho} = \sum_i \mu_i |\psi_i\rangle \langle \psi_i|, \quad (2.2.1)$$

where  $\sum_i \mu_i = 1$  (convex sum),  $\mu_i \geq 0$  and  $i \in \{1, 2, 3, \dots\}$ . If there is only one value of  $\mu_i \neq 0$ , we say that the system is in a pure state, otherwise the system is in a mixed state. A system formed by  $N$ -subsystems is separable when its density operator can be written as a convex sum of product states

$$\hat{\rho}_{\text{sep}} = \sum_i \mu'_i \hat{\rho}_i^{(1)} \otimes \hat{\rho}_i^{(2)} \otimes \dots \otimes \hat{\rho}_i^{(N)}. \quad (2.2.2)$$

When it is not possible to write the state of the system in the form (2.2.2), we say that the operator describes a system in a non-separable state or *entangled state*. Entanglement may involve only some subgroups of the quantum system. We may consider, for instance, the possibilities of combinations between the constituents of the total system. For example, the density operator

$$\hat{\rho}_{\text{semisep}} = \sum_i^N \mu'_i \hat{\rho}_i^{(1,2,\dots,s)} \otimes \hat{\rho}_i^{(s+1)} \otimes \dots \otimes \hat{\rho}_i^{(N)}, \quad (2.2.3)$$

has  $s$  non-separable subsystem components  $\hat{\rho}_i^{(1,2,\dots,s)}$  and separable subsystems. A system in which none of its subsystems can be separated from others is called completely non-separable or totally entangled. For a system with  $k$  non-separable partitions, we say that the system has  $k$ -partite entanglement.

## 2.3 Entanglement criteria

The definition of entanglement is not operational, in the sense of not providing a rule to determine whether the state is separable or not. There is a need to use entanglement criteria, which can be applied directly to the data obtained in the laboratory. There are several widely used criteria whose applications are chosen accordingly to the system used [43, 44].

One method of testing the complete inseparability of a system is to break it down into smaller subparts and check the inseparability between all possible combinations. A simple test is to divide the system into two parts, in every possible way, verifying the inseparability for each case. For a two-mode system, there is just one possible bipartition, revealing a bipartite entanglement. The same

can be done for a three-part system, checking now for the three possible bipartitions, verifying the presence of tripartite entanglement, and so on [45]. We now introduce the main criteria used in the study of entanglement in this thesis.

### 2.3.1 Sum of variances: bipartite case

We will focus on criteria that use inequalities involving the sum of variances for bipartite and tripartite systems. An important criterion developed by Duan *et al.* [46, 47] allows analyzing the inseparability of bipartite systems<sup>1</sup>. Starting from a separable density operator

$$\hat{\rho}_{\text{sep}} = \sum_i p_i \hat{\rho}_{i1} \otimes \hat{\rho}_{i2}, \quad (2.3.1)$$

and considering a general pair of EPR-like operators as

$$\hat{X}_-^a = |a| \hat{x}_1 - \frac{1}{a} \hat{x}_2, \quad (2.3.2)$$

$$\hat{Y}_+^a = |a| \hat{y}_1 + \frac{1}{a} \hat{y}_2, \quad (2.3.3)$$

such that  $[\hat{x}_j, \hat{y}_{j'}] = 2i\delta_{jj'}$ , where  $a$  is arbitrary real number. The operators  $\hat{X}_-^a$  and  $\hat{Y}_+^a$  are said to form an EPR pair [4]. Those are linear combinations of canonically conjugated operators with continuous eigenvalues that have null commutators. It is possible to show that any state of the form (2.3.1) must satisfy the inequality

$$\text{Var}[\hat{X}_+^a] + \text{Var}[\hat{Y}_-^a] \geq a^2 + a^{-2}. \quad (2.3.4)$$

Where we choose  $a$  in such a way to minimize the sum of variances (2.3.4). If the sum of the variances in the inequality above is less than the lower limit imposed for separable states, the system is entangled. Usually we are interested in a symmetric combination of quadratures where  $a = 1$ , so we define  $[\hat{X}_{\text{EPR}}, \hat{Y}_{\text{EPR}}] \equiv [\hat{x}_1 - \hat{x}_2, \hat{y}_1 + \hat{y}_2] = 0$ . The Duan sum of variances  $V_D$  must satisfy for a separable state the inequality

$$V_D \equiv \text{Var}[\hat{X}_{\text{EPR}}] + \text{Var}[\hat{Y}_{\text{EPR}}] \geq 4. \quad (2.3.5)$$

However, not all entangled states violate Duan's inequality. The criterion is sufficient to demonstrate that the system is entangled, but it is not necessary [46]. Note that the criterion can be easily applied to an experimental situation, depending only on the variances of  $\hat{X}_{\text{EPR}}$  and  $\hat{Y}_{\text{EPR}}$ . A complete reconstruction of the density operator is not necessary.

### 2.3.2 Sum of variances: tripartite case

The Duan criterion can be generalized to test the inseparability of systems with more than two parts. The extension was made by Van Loock and Furusawa in [45]. Here we describe the case of three components. Introducing the observables

$$\hat{u} = h_1 \hat{x}_1 + h_2 \hat{x}_2 + h_3 \hat{x}_3, \quad \text{and} \quad \hat{v} = g_1 \hat{y}_1 + g_2 \hat{y}_2 + g_3 \hat{y}_3, \quad (2.3.6)$$

where  $[\hat{x}_j, \hat{y}_j] = 2i\delta_{jj'}$ ,  $j \in \{1, 2, 3\}$ ,  $h_j$  and  $g_j$  are free real parameters. By dividing the system into

---

<sup>1</sup>The same criteria was obtained by Simon in an article submitted a month after the submission of Duan's paper [47]

bipartitions, we have

$$\hat{\rho}_{\text{bisep1}} = \sum \mu_i \hat{\rho}_i^{(1)} \otimes \hat{\rho}_i^{(2,3)}, \quad (2.3.7)$$

$$\hat{\rho}_{\text{bisep2}} = \sum \mu_i \hat{\rho}_i^{(2)} \otimes \hat{\rho}_i^{(1,3)}, \quad (2.3.8)$$

$$\hat{\rho}_{\text{bisep3}} = \sum \mu_i \hat{\rho}_i^{(3)} \otimes \hat{\rho}_i^{(1,2)}, \quad (2.3.9)$$

leading to three inequalities that must be respected by the partially separable systems, and can be written as

$$\hat{\rho}_{\text{bisep1}} \implies \text{Var}[\hat{u}] + \text{Var}[\hat{v}] \geq 2(|h_1 g_1| + |h_2 g_2 + h_3 g_3|), \quad (2.3.10)$$

$$\hat{\rho}_{\text{bisep2}} \implies \text{Var}[\hat{u}] + \text{Var}[\hat{v}] \geq 2(|h_2 g_2| + |h_1 g_1 + h_3 g_3|), \quad (2.3.11)$$

$$\hat{\rho}_{\text{bisep3}} \implies \text{Var}[\hat{u}] + \text{Var}[\hat{v}] \geq 2(|h_3 g_3| + |h_1 g_1 + h_2 g_2|). \quad (2.3.12)$$

Each of these inequalities, if violated, excludes the possibility of the density operator being written in the form used to deduce it. For example, if the inequality (2.3.10) is violated, then the state of the system can not be described in the form (2.3.7). For a completely separable state the following condition must be satisfied [45]

$$\sum_i \mu_i \hat{\rho}_i^{(1)} \otimes \hat{\rho}_i^{(2)} \otimes \hat{\rho}_i^{(3)} \implies \text{Var}[\hat{u}] + \text{Var}[\hat{v}] \geq 2(|h_1 g_1| + |h_2 g_2| + |h_3 g_3|), \quad (2.3.13)$$

while all physical density operators must satisfy the inequality

$$\forall \hat{\rho} \implies \text{Var}[\hat{u}] + \text{Var}[\hat{v}] \geq 2|h_1 g_1 + h_2 g_2 + h_3 g_3|. \quad (2.3.14)$$

The choices of the free constants  $h_j$  and  $g_j$  must be made to leverage the kind of correlations in the system of study. In general, a choice is made in which the right-hand side of the (2.3.14) cancels out. After analysis and selection of the parameters, we reach three inequalities that allow the characterization of tripartite entanglement

$$V_{12} = \text{Var}[\hat{x}_1 - \hat{x}_2] + \text{Var}[\hat{y}_1 + \hat{y}_2 + g_3 \hat{y}_3] \geq 4, \quad (2.3.15)$$

$$V_{13} = \text{Var}[\hat{x}_1 + \hat{x}_3] + \text{Var}[\hat{y}_1 - \hat{y}_3 + g_2 \hat{y}_2] \geq 4, \quad (2.3.16)$$

$$V_{23} = \text{Var}[\hat{x}_2 + \hat{x}_3] + \text{Var}[\hat{y}_2 - \hat{y}_3 + g_1 \hat{y}_1] \geq 4, \quad (2.3.17)$$

the index of  $V_{ij}$  indicate that the inequality is a separability test between partitions  $i$  and  $j$ . A violation of two of the inequalities (2.3.15) - (2.3.17), is a sufficient condition to demonstrate tripartite entanglement. We use the Van Loock and Furusawa inequalities to test tripartite entanglement in the OPO above the oscillation threshold.

## 2.4 Electromagnetic field operators

In this session, we introduce the formalism we use to describe modes of the electromagnetic field. The reader with no familiarity with light modulation should start with Appendix A. The quantization of the electromagnetic field in a box gives an electric field that is described by the operator [23]

$$\hat{\mathbf{E}}(\mathbf{r}, t) = i \sum_{ks} \sqrt{\frac{2\pi\hbar\omega_k}{V}} \left[ \boldsymbol{\epsilon}_{ks} \hat{a}_{ks} e^{i(\mathbf{k}\cdot\mathbf{r} - \omega_k t)} - \boldsymbol{\epsilon}_{ks}^* \hat{a}_{ks}^\dagger e^{-i(\mathbf{k}\cdot\mathbf{r} - \omega_k t)} \right], \quad (2.4.1)$$

where  $[\hat{a}_{ks}, \hat{a}_{k's'}^\dagger] = \delta_{kk'}\delta_{ss'}$  and the sum is made over the complete set of  $k$ -vectors and polarization modes  $s$ . Taking the box volume to infinity, the field in the paraxial regime propagating in a specific direction, can be describe as a continuum of modes. In this case, the quantized electromagnetic field can be expressed as

$$\hat{E}(\mathbf{r}; t) = \Phi(\mathbf{r})\{\hat{E}^{(+)}(t) + \hat{E}^{(-)}(t)\}, \quad (2.4.2)$$

where we define

$$\hat{E}^{(+)}(t) = \int_0^\infty \frac{d\omega}{2\pi} \sqrt{\frac{2\pi\hbar\omega}{\mathcal{A}c}} \hat{a}_\omega e^{-i\omega t}, \quad \text{and} \quad \hat{E}^{(-)}(t) = [\hat{E}^{(+)}(t)]^\dagger, \quad (2.4.3)$$

the function  $\Phi(\mathbf{r})$  is the spatial profile of the beam<sup>2</sup>,  $\mathcal{A}$  is the effective cross-sectional area and  $\hat{a}_\omega$  is the mode annihilation operator of the field with oscillation frequency  $\omega$ . The commutation relations are

$$[\hat{a}_\omega, \hat{a}_{\omega'}^\dagger] = 2\pi\delta(\omega - \omega'), \quad \text{and} \quad [\hat{a}_\omega, \hat{a}_{\omega'}] = [\hat{a}_\omega^\dagger, \hat{a}_{\omega'}^\dagger] = 0. \quad (2.4.4)$$

In (2.4.3), the description takes into account all possible frequencies. But, we are interested in describing a laser field that is a intense quasimonochromatic beam propagating with an optical frequency  $\omega_l$ . For such light fields it is interesting to define a temporal mode associated with the annihilation operator  $\hat{a}(t)$  where the field takes the form  $\hat{E}(t) \approx \mathcal{K}_l[\hat{a}(t)e^{-i\omega_l t} + \hat{a}^\dagger(t)e^{i\omega_l t}]/2$ , by defining

$$\hat{a}(t) \approx \int_{-\infty}^\infty \frac{d\Omega}{2\pi} \hat{a}_\Omega e^{-i\Omega t} = \mathbb{F}^{-1}\{\hat{a}(\Omega)\}, \quad (2.4.5)$$

$$\hat{a}^\dagger(t) \approx \int_{-\infty}^\infty \frac{d\Omega}{2\pi} \hat{a}_{-\Omega}^\dagger e^{-i\Omega t} = (\mathbb{F}^{-1}\{\hat{a}(\Omega)\})^\dagger, \quad (2.4.6)$$

where  $\mathcal{K}_l \equiv \sqrt{4\pi\hbar\omega_l/(\mathcal{A}c)}$ , and  $\hat{a}_{\pm\Omega} \equiv \hat{a}_{\omega_l \pm \Omega}$ ; the approximations in (2.4.5) and (2.4.6) are valid for  $|\Omega| \ll \omega_l$ .  $\hat{a}(t)$  is the quantum analog of a slow varying envelop amplitude of the quasimonochromatic field, equivalent to description in the laser's rotating frame. The operator  $\hat{a}(\Omega)$  lives in the Fourier space. We can build the field quadrature operators in time domain as

$$\hat{p}(t) \equiv \hat{a}(t) + \hat{a}^\dagger(t) = \int_{-\infty}^\infty \frac{d\Omega}{2\pi} (\hat{a}_\Omega + \hat{a}_{-\Omega}^\dagger) e^{-i\Omega t} = \mathbb{F}^{-1}\{\hat{p}(\Omega)\}, \quad (2.4.7)$$

$$\hat{q}(t) \equiv -i[\hat{a}(t) - \hat{a}^\dagger(t)] \equiv -i \int_{-\infty}^\infty \frac{d\Omega}{2\pi} (\hat{a}_\Omega - \hat{a}_{-\Omega}^\dagger) e^{-i\Omega t} = \mathbb{F}^{-1}\{\hat{q}(\Omega)\}. \quad (2.4.8)$$

so we can write the field operator as  $\hat{E}(\mathbf{r}; t) = \mathcal{K}_l\Phi(\mathbf{r})[\hat{p}(t) \cos \omega_l t + \hat{q}(t) \sin \omega_l t]$ . In (2.4.7) and (2.4.8) we define the Fourier transform of the quadrature operators  $\hat{p}(\Omega) \equiv \hat{a}_\Omega + \hat{a}_{-\Omega}^\dagger$ ,  $\hat{q}(\Omega) \equiv -i(\hat{a}_\Omega - \hat{a}_{-\Omega}^\dagger)$ , meaning that in the frequency domain the quadrature operators care information on the modes  $\Omega$  and  $-\Omega$  defined in relation to the laser carrier frequency  $\omega_l$ . Notice that  $\hat{p}^\dagger(\Omega) = \hat{p}(-\Omega)$  and  $\hat{q}^\dagger(\Omega) = \hat{q}(-\Omega)$ , therefore, non-Hermitian operators. We can also write the annihilation operator  $\hat{a}_{\pm\Omega}$  decomposed into quadrature operators corresponding to the frequency modes  $\omega_l + \Omega$ , we have

$$\hat{a}_\Omega = [\hat{p}(\Omega) + i\hat{q}(\Omega)]/2, \quad \text{and} \quad \hat{a}_\Omega^\dagger = [\hat{p}(\Omega) - i\hat{q}(\Omega)]/2. \quad (2.4.9)$$

Since (2.4.9) is linking two different pictures of the electromagnetic field description, it can lead to confusion. Defining a quadrature decomposition to the single mode picture

$$\hat{a}_\Omega = p_\Omega + iq_\Omega, \quad \text{and} \quad \hat{a}_\Omega^\dagger = p_\Omega - iq_\Omega. \quad (2.4.10)$$

---

<sup>2</sup>Check Appendix B.

Here  $p_\Omega$  and  $q_\Omega$  are Hermitian operators. We can writing the vector  $\mathbf{Z}(\Omega) = [\hat{p}(\Omega), \hat{q}(\Omega), \hat{p}(-\Omega), \hat{q}(-\Omega)]^T$  and  $\mathbf{Z}_\Omega = [\hat{p}_\Omega, \hat{q}_\Omega, \hat{p}_{-\Omega}, \hat{q}_{-\Omega}]^T$  we can relate the two descriptions by

$$\mathbf{Z}_\Omega = \mathbb{L}\mathbf{Z}(\Omega), \quad (2.4.11)$$

where

$$\mathbb{L} = \frac{1}{2} \begin{bmatrix} 1 & i & 1 & -i \\ -i & 1 & i & 1 \\ 1 & -i & 1 & i \\ i & 1 & -i & 1 \end{bmatrix}, \quad (2.4.12)$$

$\mathbb{L}$  is in fact unitary,  $\mathbb{L}^{-1} = \mathbb{L}^\dagger = \mathbb{L}$ .

The modulation of a carrier frequency implies necessarily in the generation of pairs of sidebands. By modulating a carrier in amplitude or phase, correlated sidebands emerge with balanced power distribution, as describes in Appendix A.

## 2.5 States and representations

To complete the description of the quantum electromagnetic field and understand the limits where the quantum formalism is necessary we focus now on the states of the field. We also introduce the phase space representation in terms of the Wigner function that we use to describe the OPO's dynamics. Also, we define the set of Gaussian states.

### 2.5.1 Fock states

The energy of the quantum electromagnetic field takes the form of a sum of independent quantum harmonic oscillators Hamiltonians, each one corresponding to a specific field mode [23]. Considering for the moment a single-mode subspace, we will only deal with the operators  $\hat{a}$  and  $\hat{a}^\dagger$ . This system has Hamiltonian

$$\hat{H} = \hbar\omega \left( \hat{a}^\dagger \hat{a} + 1/2 \right), \quad (2.5.1)$$

the eigenstates of this Hamiltonian are the vectors  $|n\rangle$  that satisfy the eigenvalue equation  $\hat{a}^\dagger \hat{a} |n\rangle = \hat{n} |n\rangle = n |n\rangle$  having the ortonormality propriety and completeness

$$\langle n | n' \rangle = \delta_{nn'}, \quad \sum_{n=0}^{\infty} |n\rangle \langle n| = \hat{\mathbb{I}}. \quad (2.5.2)$$

The eigenstates of the number operator  $\hat{n}$  constitute the simplest basis for the Hilbert space of the electromagnetic field, thus form the starting point for the study of the quantum properties of the electromagnetic field. These states are known as *Fock states*. From the bosonic commutation relation follows that Fock states obey the fundamental relations  $\hat{a} |n\rangle = \sqrt{n} |n-1\rangle$  and  $\hat{a}^\dagger |n\rangle = \sqrt{n+1} |n+1\rangle$ . The called vacuum state  $|0\rangle$  is the minimum energy state. It is defined as  $\hat{a} |0\rangle = 0$  and has a null mean number of photons.

We can write a general Fock state  $|n\rangle$  in terms of the vacuum state  $|0\rangle$

$$|n\rangle = \frac{(\hat{a}^\dagger)^n}{\sqrt{n!}} |0\rangle. \quad (2.5.3)$$

For a multimode description of the field, we can write the state as  $|n_{ks}\rangle$ , meaning that the mode  $(\mathbf{k}, s)$  has  $n_{ks}$  photons. The full state state is the tensor product of states for each mode. The generation of

on-demand states with well-defined photon numbers is an experimental challenge [48]. Fock states are highly nonclassical states.

### 2.5.2 Quadrature states

As discussed in section 2.4, for quadratures operators  $\hat{x} = \hat{a} + \hat{a}^\dagger$ , and  $\hat{y} = -i(\hat{a} - \hat{a}^\dagger)$ , the commutation relation is given by  $[\hat{x}, \hat{y}] = 2i$ . To satisfy the canonical commutation relation implies that the eigenstates of the quadratures can be defined as  $\hat{x}|x\rangle = x|x\rangle$  and  $\hat{y}|y\rangle = y|y\rangle$  which have a continuous spectrum, assuming values between  $-\infty$  and  $+\infty$  [3]. Moreover, the eigenstates are orthogonal

$$\langle x|x'\rangle = \delta(x - x'), \quad \langle y|y'\rangle = \delta(y - y') \quad (2.5.4)$$

complete

$$\int_{-\infty}^{+\infty} dx |x\rangle \langle x| = \int_{-\infty}^{+\infty} dy |y\rangle \langle y| = \hat{\mathbb{I}}, \quad (2.5.5)$$

and related by Fourier's transform

$$|x\rangle = \frac{1}{\sqrt{2\pi}} \int_{-\infty}^{+\infty} dy e^{-iyx} |y\rangle. \quad (2.5.6)$$

Because they are not normalized they do not correspond to physical states that can be produced in the laboratory, but they are of fundamental importance in the description of the phase space. We can think of writing a wave function in the  $\hat{x}$  representation, for instance, this allows us to write a wave function for a Fock state in the space of quadratures as

$$\Psi_n(x) = \langle x|n\rangle = \frac{1}{\sqrt{2^n \sqrt{\pi}}} H_n(x) e^{-x^2/2}, \quad (2.5.7)$$

where  $H_n$  represents a Hermite polynomial of degree  $n$ . The squared modulus of this wave function describes the probability density for measurements of quadrature  $\hat{x}$  in state  $|n\rangle$ . In the same way we can find  $\tilde{\Psi}_n(y) = \langle y|n\rangle$  as

$$\tilde{\Psi}_n(y) = \frac{1}{\sqrt{2\pi}} \int_{-\infty}^{+\infty} dx \Psi_n(x) e^{-ixy}. \quad (2.5.8)$$

Both the distributions  $|\Psi_n(x)|^2$  and  $|\tilde{\Psi}_n(y)|^2$  can be measured by the homodyne detection [49]. Substituting  $\hat{x}$  and  $\hat{y}$  into the Heisenberg uncertainty relation we have

$$\text{Var}[\hat{x}]\text{Var}[\hat{y}] \geq 1. \quad (2.5.9)$$

For a Fock state the relation is  $\text{Var}[\hat{x}]\text{Var}[\hat{y}] = (n + 1/2)^2$ , where  $\text{Var}[\hat{x}] = \text{Var}[\hat{y}] = n + 1/2$ . It shows that the noise in the quadratures of the field in a Fock state is symmetrically distributed between  $\hat{x}$  and  $\hat{y}$  and increases linearly with the number of photons.

### 2.5.3 Coherent states

A classical wave can have well defined amplitude and phase. We have seen that in the quantum theory of the electromagnetic field the complex amplitude of the field is replaced by the annihilation operator  $\hat{a}$ . To look for quantum states with well defined amplitude and phase, we can investigate the eigenstates of the operator  $\hat{a}$ , as  $\hat{a}|\alpha\rangle = \alpha|\alpha\rangle$ . In this case, the expected values of the quadratures of



the field correspond to the classic values:

$$\langle \alpha | \hat{x} | \alpha \rangle = \alpha + \alpha^*, \quad \langle \alpha | \hat{y} | \alpha \rangle = -i(\alpha - \alpha^*). \quad (2.5.10)$$

Expanding the state  $|\alpha\rangle$  in terms of Fock states we arrive at the normalized state

$$|\alpha\rangle = e^{-|\alpha|^2/2} \sum_{n=0}^{\infty} \frac{\alpha^n}{\sqrt{n!}} |n\rangle, \quad (2.5.11)$$

which is called a coherent state. It corresponds to a superposition of an infinity of Fock states. The probability to find the system in a state  $|n\rangle$  is a Poisson distribution  $P(n) = |\alpha|^{2n} e^{-|\alpha|^2} / n!$ , which is characteristic of random and uncorrelated processes. Among other important properties of  $P(n)$ , its variance is equal to its mean. Thus, for a coherent state

$$\text{Var}[\hat{n}] = \langle \hat{n} \rangle = |\alpha|^2. \quad (2.5.12)$$

The coherent states form an overcomplete set, which can be stated as

$$\frac{1}{\pi} \int d^2\alpha |\alpha\rangle \langle \alpha| = \hat{\mathbb{I}}. \quad (2.5.13)$$

To formalize some properties, it is interesting to introduce the *displacement operator* defined as

$$\hat{D}(\alpha) \equiv \exp(\alpha \hat{a}^\dagger - \alpha^* \hat{a}). \quad (2.5.14)$$

A state  $|\alpha\rangle$  can then be seen as a displaced vacuum state, Fig. 2.2, since  $|\alpha\rangle = \hat{D}(\alpha) |0\rangle$ . The coherent states are known to be states that saturate Heisenberg's uncertainty relation to quadrature operators,  $\text{Var}[\hat{x}] = \text{Var}[\hat{y}] = 1$ , therefore

$$\text{Var}[\hat{x}]\text{Var}[\hat{y}] = 1, \quad \forall \alpha. \quad (2.5.15)$$

To examine the time evolution of a coherent state, we apply the evolution operator to the Hamiltonian

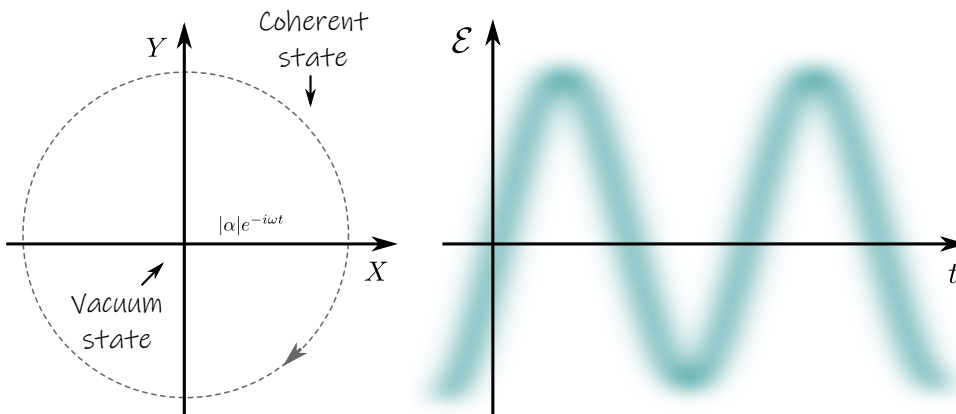


Figure 2.2: (Left) Representation of a coherent state in phase space. (Right) Time evolution of the electric field in a coherent state.

(2.5.1) for a single-mode  $e^{-i\hat{H}t/\hbar} |\alpha\rangle = |\alpha e^{-i\omega t}\rangle e^{-i\omega t/2}$  then we see that the evolution of a coherent state leads to another coherent state with a different phase, Fig. 2.2. The uncertainties in the quadratures are independent of the amplitude of the state; therefore, the state continues to preserve its uncertainty relation saturation properties.

### 2.5.4 Squeezed states

A quadrature that its noise is less than the vacuum noise characterizes a nonclassical state of light that a statistical mixture of coherent states can not describe. These are called squeezed states of light<sup>3</sup>. The first squeezing demonstration was done using an atomic system [54], followed by a nonlinear fiber generation [55]. The single-mode squeezed vacuum state  $|\xi\rangle$  is defined by the application of a unitary squeezing operator

$$\hat{S}(\xi) = \exp \left[ (\xi \hat{a}^{2\dagger} - \xi^* \hat{a}^2) / 2 \right], \quad \xi = r e^{i\varphi}, \quad (2.5.16)$$

on the vacuum state  $|\xi\rangle = \hat{S}(\xi) |0\rangle$ . It is interesting to expand the squeezing operator and express the state  $|\xi\rangle$  in terms of the Fock states, resulting in

$$|\xi\rangle = \frac{1}{\sqrt{\cosh r}} \sum_{n=0}^{\infty} e^{in\varphi} (\tanh r)^n \frac{\sqrt{(2n)!}}{n! 2^n} |2n\rangle. \quad (2.5.17)$$

We see that only Fock states with even numbers of excitations are present. The so-called squeezed coherent states are defined by

$$|\alpha, \xi\rangle = \hat{D}(\alpha) \hat{S}(\xi) |0\rangle, \quad (2.5.18)$$

that is, a coherent squeezed state is obtained by the application of the displacement operator on the squeezed vacuum. Now consider a more general quadrature  $\hat{x}(\theta)$ , where

$$\hat{x}(\theta) = \hat{a} e^{-i\theta} + \hat{a}^\dagger e^{i\theta}, \quad (2.5.19)$$

taking the variances in the quadratures defined by the parameter  $\xi$  (2.5.16) we obtain

$$\text{Var}[\hat{x}(\varphi/2)] = e^{2r}, \quad \text{Var}[\hat{x}(\varphi/2 + \pi/2)] = e^{-2r}, \quad (2.5.20)$$

showing that the quadratures still satisfy the minimum conditions of the Heisenberg inequality. However, it is now possible to have quantum noise smaller than the vacuum noise in one of the quadratures, Fig. 2.3. This suppression of noise in one quadrature is compensated by excess noise in the conjugated quadrature,  $\text{Var}[\hat{x}(\varphi/2)] \text{Var}[\hat{x}(\varphi/2 + \pi/2)] = 1$ . We will see that squeezed noise and entanglement are deeply connected.

There are several practical applications of phase noise or amplitude squeezing. It can be used to improve the accuracy of some experiments to limits below standard quantum noise. For example, every interferometer that uses beam splitters contains inputs that are not used; such unused inputs are actually, in quantum theory, input ports for the vacuum  $|0\rangle$  insert noise into the system. C. Caves proposed using squeezed vacuum in these entries, [56] which reduces the quantum noise in the system and, consequently, the greater precision of the interferometer; this effect was demonstrated experimentally in [57].

### 2.5.5 The Wigner function

Wigner introduced a phase space distribution for a quantum system with probability distribution properties, revealing to be useful to calculate expected values of physical quantities [58]. However, the Wigner function can have negative values, so it can not be a probability function and is called a quasiprobability function. This function is useful in the field of quantum optics, especially in the

<sup>3</sup>List of reviews on squeezed light [22, 50–53].

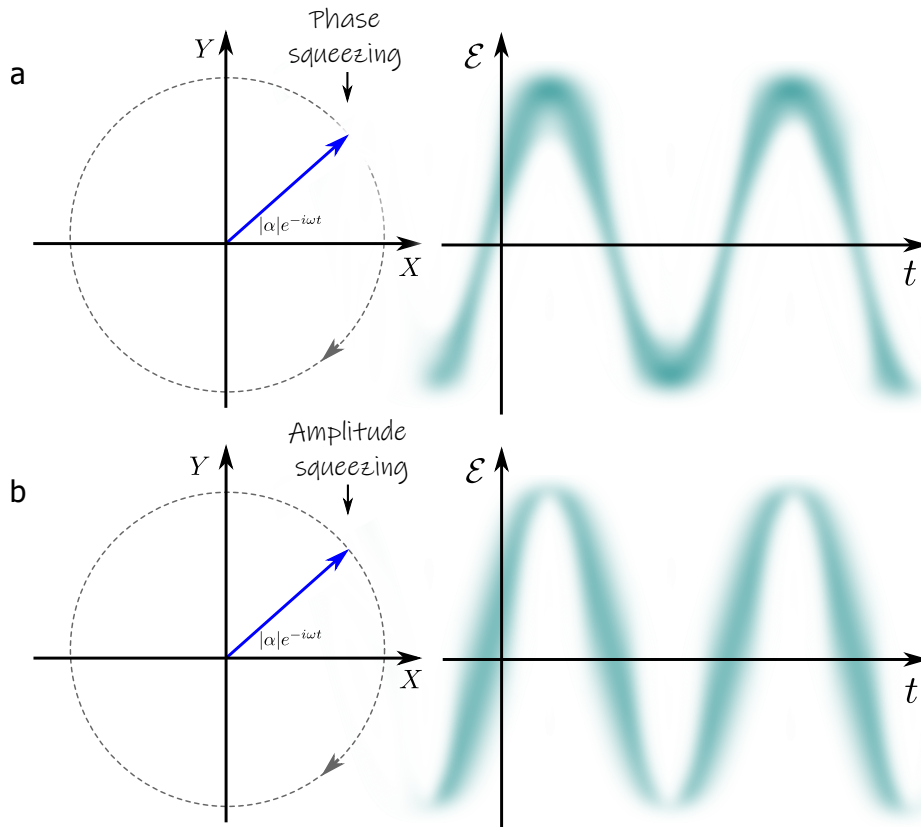


Figure 2.3: Phase space representation of a squeezed coherent state, (a-left) squeezing in perpendicular to the intense field phasor (phase squeezing), (b-left) squeezing along the direction of the intense field phasor (amplitude squeezing). The ellipse represents squeezed quantum noise. The dashed circle represents the noise distribution for a coherent state. Time evolution of the electric field for a phase squeezed state (a-right), and for amplitude squeezing state (b-right).

characterization of nonclassical states. For an in-depth discussion of the phase space in quantum optics, see [59]. In the theory of probabilities, we can describe a distribution by the Fourier transform of its characteristic function. We define the Wigner function

$$\mathcal{W}(\alpha) = \frac{1}{\pi^2} \int d^2\beta \Xi(\beta) e^{-(\beta\alpha^* - \beta^*\alpha)}, \quad (2.5.21)$$

as the two-dimensional Fourier transform<sup>4</sup> of the characteristic function  $\Xi(\beta)$ , defined as

$$\Xi(\beta) = \text{Tr}[\hat{\rho} \exp(\beta\hat{a}^\dagger - \beta^*\hat{a})]. \quad (2.5.22)$$

The integral over the whole space is normalized

$$\int d^2\alpha \mathcal{W}(\alpha) = 1. \quad (2.5.23)$$

To gain some familiarity we can calculate the Wigner function for some common states. For a coherent state  $|\gamma\rangle$  we have

$$\mathcal{W}_c(\alpha) = \frac{2}{\pi} \exp(-2|\alpha - \gamma|^2). \quad (2.5.24)$$

The calculation for a Fock state  $|n\rangle$  gives

$$\mathcal{W}_n(\alpha) = \frac{2}{\pi} (-1)^n e^{-2|\alpha|^2} L_n(4|\alpha|^2), \quad (2.5.25)$$

where  $L_n$  are the Laguerre's polynomials, where we see that  $\mathcal{W}_n$  can be negative. For instance, for  $n = 1$  we will have  $\mathcal{W}_1(\alpha)$ , which is negative for the whole region where  $|\alpha| < 1/4$ . The Wigner function can be used to spotlight nonclassical states when it has negative values, as in the case of Fock states  $|n\rangle$ .

We can calculate expected values as averages in the phase space. Given an operator  $\hat{G}$  corresponding to a physical observable we can rewrite it as

$$\hat{G} = \frac{1}{\pi} \int d^2\gamma \text{Tr}[\hat{G}\hat{D}^\dagger(\gamma)]\hat{D}(\gamma). \quad (2.5.26)$$

And its expected value  $\langle\hat{G}\rangle$  will be given by

$$\langle\hat{G}\rangle = \text{Tr}(\hat{\rho}\hat{G}) = \frac{1}{\pi} \int d^2\gamma \text{Tr}[\hat{G}\hat{D}^\dagger(\gamma)]\text{Tr}[\hat{\rho}\hat{D}(\gamma)], \quad (2.5.27)$$

we can reverse (2.5.21) getting  $\text{Tr}[\hat{\rho}\hat{D}(\gamma)] = \int d^2\alpha \mathcal{W}(\alpha) e^{\gamma\alpha^* - \gamma^*\alpha}$  this way we have

$$\langle\hat{G}\rangle = \pi \int d^2\alpha \mathcal{W}(\alpha) \mathcal{W}_{\hat{G}}(\alpha), \quad (2.5.28)$$

where  $\mathcal{W}_{\hat{G}}$  is the Wigner function associated with the operator  $\hat{G}$ , defined by the change of  $\hat{\rho}$  by  $\hat{G}$ , in (2.5.21). For example, the Wigner function will serve as probability density in the calculation of moments of the field in symmetric order,

$$\langle\hat{a}^r(\hat{a}^\dagger)^s\rangle = \int d^2\alpha \mathcal{W}(\alpha) \alpha^r (\alpha^*)^s. \quad (2.5.29)$$

<sup>4</sup>In (2.5.21)  $\alpha$  is a complex number, such that  $\alpha = x + iy$  and the integral is calculated over the element of integration  $d^2\alpha = dx dy$  in  $\mathbb{R}^2$ .

The Wigner function of a squeezed vacuum state, defined by (2.5.16) and (2.5.17), is given by

$$\mathcal{W}_\xi(\alpha) = \frac{2}{\pi} \exp(-2|\alpha \cosh r - \alpha^* e^{i\varphi} \operatorname{senhr}|^2). \quad (2.5.30)$$

It can be seen that the contour ellipses of the Wigner function (cuts at a given height in the phase space) are proportional to quadrature noise. It is this visual appeal and calculation properties that make the Wigner function so useful in quantum optics.

## 2.6 Gaussian states

A fundamental framework for continuous variables quantum information is the set of Gaussian states [60,61]. We described how a longitudinal mode of the field, of frequency  $\omega$ , can be represented by quadrature operators  $\hat{x}_\omega$  and  $\hat{y}_\omega$ , satisfying  $[\hat{x}_\omega, \hat{y}_{\omega'}] = 2i\delta(\omega - \omega')$ , which can be written according to the bosonic operators of creation  $\hat{a}_\omega^\dagger$  and annihilation as  $\hat{a}_\omega = (\hat{x}_\omega + i\hat{y}_\omega)/2$ . Consider the case of  $N$  modes labeled by  $k \in \{1, \dots, N\}$ , which  $N$  Hilbert spaces  $\mathcal{H}_k$  are associated. Introducing the vector of quadratures  $\hat{\mathbf{r}} \equiv (\hat{x}_1, \hat{y}_1, \dots, \hat{x}_N, \hat{y}_N)^T$  we can write the canonical commutation relation in the compact form

$$[\hat{\mathbf{r}}_l, \hat{\mathbf{r}}_m] = 2i\mathbb{J}_{lm}^N, \quad (l, m = 1, \dots, 2N), \quad (2.6.1)$$

where

$$\mathbb{J}^N \equiv \bigoplus_{k=1}^N \mathbb{J}, \quad \text{and} \quad \mathbb{J} \equiv \begin{pmatrix} 0 & 1 \\ -1 & 0 \end{pmatrix}. \quad (2.6.2)$$

The symbol  $\bigoplus$  denotes the direct sum. We say that a state  $\hat{\rho}$  is Gaussian if the corresponding characteristic function is Gaussian

$$\Xi(\boldsymbol{\xi}) = \exp \left[ -\boldsymbol{\xi}^T \frac{\mathbb{V}}{2} \boldsymbol{\xi} + i\mathbf{d}^T \boldsymbol{\xi} \right], \quad (2.6.3)$$

with  $\boldsymbol{\xi} \in \mathbb{R}^{2N}$ . The state  $\hat{\rho}$  is fully characterized by its displacement  $\mathbf{d} \equiv \langle \hat{\mathbf{r}} \rangle$ , and its covariance matrix (CM)  $\mathbb{V}$ . A generic CM element is defined as

$$\mathbb{V}_{lm} \equiv \langle \delta \hat{\mathbf{r}}_l \delta \hat{\mathbf{r}}_m + \delta \hat{\mathbf{r}}_m \delta \hat{\mathbf{r}}_l \rangle / 2, \quad (2.6.4)$$

where  $\delta \hat{\mathbf{r}}_l \equiv \hat{\mathbf{r}}_l - \langle \hat{\mathbf{r}}_l \rangle$ . The fact that the CM is a  $2N \times 2N$  real and symmetric matrix imply the *bona fide* condition

$$\mathbb{V} + i\mathbb{J}^N \geq 0, \quad (2.6.5)$$

which is equivalent to the uncertainty principle [61]. The Wigner function of a Gaussian state is given by

$$\mathcal{W}(\mathbf{r}) = \frac{1}{(2\pi)^N \sqrt{\det \mathbb{V}}} \exp \left[ -\frac{1}{2} (\mathbf{r} - \mathbf{d})^T \mathbb{V}^{-1} (\mathbf{r} - \mathbf{d}) \right]. \quad (2.6.6)$$

The covariance matrix contains all the information necessary to characterize a Gaussian state. For a state of  $N$ -modes,  $2N^2 + 3N$  real parameters are required to a full description; first-order and second-order moments determine the state entirely.

Restricting our analysis to the set of Gaussian states, violation of the entanglement criteria discussed in section 2.3 are sufficient and necessary conditions to demonstrate entanglement [61].

### 2.6.1 Symplectic transformations

Any possible physical operation applied to a system described by the quadrature vector should preserve the canonical commutation relations. A general linear transformation such that

$$\mathbb{S} : \hat{\mathbf{r}} \longrightarrow \hat{\mathbf{r}}' \equiv \mathbb{S}\hat{\mathbf{r}}, \quad (2.6.7)$$

to be an allowed transformation must satisfy the condition

$$\mathbb{S}\mathbb{J}^{(N)}\mathbb{S}^T = \mathbb{J}^{(N)}. \quad (2.6.8)$$

The set of all  $2N \times 2N$  real matrices that satisfy equation (2.6.8) is called a *real symplectic group*  $S_p(2N, \mathbb{R})$ ; elements of this group are called *symplectic transformations*. Each symplectic transformation  $\mathbb{S}$  acting on phase space corresponds to a unitary transformation  $\hat{U}_{\mathbb{S}}$  in the Hilbert space. The relation between them is determined by

$$\hat{U}^\dagger \hat{\mathbf{r}} \hat{U} = \mathbb{S}\hat{\mathbf{r}}. \quad (2.6.9)$$

Those transformation map Gaussian states into Gaussian states and are called *Gaussian operations*. An arbitrary symplectic transformation, as in (2.6.7), is equivalent to a transformation in the Wigner function

$$\mathcal{W}(\mathbf{r}') = \mathcal{W}(\mathbb{S}^{-1}\mathbf{r}), \quad (2.6.10)$$

and the effect on the CM is

$$\mathbb{V} \longrightarrow \mathbb{S}\mathbb{V}\mathbb{S}^T. \quad (2.6.11)$$

Squeezing, phase shifts, and beam mixing in a beamsplitter are examples of symplectic transformations [61], Therefore they do not change the Gaussian character of the initial state.

## 2.7 Noise measurement techniques

There is no detector fast enough to measure fields in the optical frequency domain<sup>5</sup>. The usual photodetectors are sensitive to the temporal averages of light intensity. Typically, photodetectors are based on the photoelectric effect, generating photocurrents proportional to incident photons' flux [62]. In [63], we see that we can associate the current generated by a detector with the observable  $\hat{i}(t)$  given by

$$\hat{i}(t) = \hat{E}^{(-)}(\mathbf{r}, t)\hat{E}^{(+)}(\mathbf{r}, t), \quad (2.7.1)$$

considering unit conversion efficiency. The average current measured during an interval  $\tau$  for a given quantum state  $|\psi(t)\rangle$  will be

$$\langle \hat{i}(t) \rangle = N_d \int_t^{t+\tau} \langle \psi(t) | \hat{E}^{(-)}(\mathbf{r}, t)\hat{E}^{(+)}(\mathbf{r}, t) | \psi(t) \rangle dt, \quad (2.7.2)$$

the constant  $N_d$  is a constant depending on the detector and its electronics. We can write the photocurrent operator as a well-defined mean value added to the fluctuations  $\delta\hat{i}(t)$  around the average value as

$$\hat{i}(t) = \langle \hat{i} \rangle + \delta\hat{i}(t). \quad (2.7.3)$$

In the same way, we can rewrite the creation and annihilation operators by separating the average value from the fluctuations

$$\hat{a}(t) = \alpha + \delta\hat{a}(t), \quad \hat{a}^\dagger(t) = \alpha^* + [\delta\hat{a}(t)]^\dagger \quad (2.7.4)$$

<sup>5</sup>With an oscillation frequency of the order of  $10^{14}$  Hz.

where  $\alpha = |\alpha|e^{i\bar{\theta}} = \langle \hat{a}(t) \rangle$ . For a single-mode we can write the direct relation between the photocurrent and the number operator as  $\hat{i}(t) = \hat{a}^\dagger(t)\hat{a}(t)$  which leads to equation

$$\delta \hat{i}(t) = \alpha^* \delta \hat{a}(t) + \alpha \delta \hat{a}^\dagger(t) + \delta \hat{a}^\dagger(t) \delta \hat{a}(t). \quad (2.7.5)$$

Disregarding the second-order terms in the fluctuations, valid when  $\langle \delta \hat{a}^\dagger \delta \hat{a} \rangle \ll |\alpha|^2$ , we have

$$\delta \hat{i}(t) = \alpha^* \delta \hat{a}(t) + \alpha \delta \hat{a}^\dagger(t). \quad (2.7.6)$$

The above equation in function of the generalized quadrature

$$\begin{aligned} \delta \hat{i}(t) &= |\alpha| [e^{-i\bar{\theta}} \delta \hat{a}(t) + e^{i\bar{\theta}} \delta \hat{a}^\dagger(t)] \\ &= |\alpha| \delta \hat{x}(\bar{\theta}). \end{aligned} \quad (2.7.7)$$

We see that the fluctuations in the photocurrent give us a direct measure of the quadrature fluctuations projected along with the mean field  $\alpha$  in the phase space (or the Fresnel representation). For this reason we call this quadrature as *amplitude quadrature* and we will represent it as  $\hat{p}$ . It can be experimentally evaluated from the beam intensity fluctuations as

$$\delta \hat{p} \equiv \delta \hat{x}(\bar{\theta}) = \delta \hat{i}(t) / \sqrt{\langle \hat{i} \rangle}. \quad (2.7.8)$$

The conjugate quadrature will be related to phase fluctuations and we will call it *phase quadrature*, denoted by  $\hat{q}$ , the geometric interpretation can be seen in the Fig. 2.4. The formal expressions for the amplitude and phase quadratures are given in terms of the creation and annihilation operators:

$$\delta \hat{p}(t) = e^{-i\bar{\theta}} \delta \hat{a}(t) + e^{i\bar{\theta}} \delta \hat{a}^\dagger(t), \quad (2.7.9)$$

$$\delta \hat{q}(t) = -i[e^{-i\bar{\theta}} \delta \hat{a}(t) - e^{i\bar{\theta}} \delta \hat{a}^\dagger(t)]. \quad (2.7.10)$$

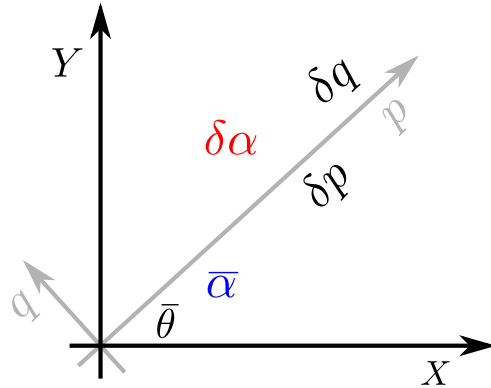


Figure 2.4: Representation of how the field fluctuation  $\delta\alpha$  can be decomposed in terms corresponding to fluctuations  $\delta p$  and  $\delta q$ . The mean field  $\bar{\alpha}$  defines a orientation  $\bar{\theta}$  defining amplitude and phase quadratures.

The analysis of fluctuations becomes simpler when we move from the time space to the frequency space. Using the definitions discussed in section 2.4, the noise spectrum  $\mathcal{S}[\hat{x}_\theta, \Omega]$  of a generalized quadrature is obtained by the Wiener-Khinchin theorem [64]

$$\langle \delta x_\theta(\Omega) \delta x_\theta(-\Omega') \rangle = 2\pi \delta(\Omega - \Omega') \mathcal{S}[\hat{x}_\theta, \Omega], \quad (2.7.11)$$

and is related to the spectral energy distribution of the field. The noise power  $\mathcal{S}[\hat{x}_\theta, \Omega]$  is proportional to the generalized quadrature variance. In practice, the noise spectrum is measured within a certain

frequency bandwidth, implying that  $\mathcal{S}[\hat{x}_\theta, \Omega]$  will not be the exact variance of frequency  $\Omega$ , but after the approximations, we obtain something proportional to the desired variance [65]. We need a reference calibrated under the same conditions to serve as a noise comparison unit. This reference is the *shot noise*, which corresponds to the noise of the vacuum state.

## 2.8 Homodyne detection

The photodetectors give us directly the fluctuations of the amplitude quadrature. However, to make measurements sensitive to the phase, it is necessary to use interferometric techniques. The homodyne detection makes use of an intense coherent beam, called the local oscillator (LO), as a phase reference. Using a beamsplitter (BS), the local oscillator is mixed with the field to be measured, as shown in Fig. 2.5. The input fields in the BS will be described by the annihilation operators  $\hat{a}_k$  and  $\hat{b}_k$  (LO), while the output fields by  $\hat{a}_o$  and  $\hat{b}_o$ . For a symmetric BS, where 50% of the light is transmitted, and 50% is reflected, the unitary transformation between input and output ports gives [66]

$$\hat{a}_o = (\hat{a}_k + i\hat{b}_k)/\sqrt{2}, \quad \hat{b}_o = (i\hat{a}_k + \hat{b}_k)/\sqrt{2}. \quad (2.8.1)$$

The difference between the photocurrents is

$$\hat{i}_- = \hat{a}_o^\dagger \hat{a}_o - \hat{b}_o^\dagger \hat{b}_o = i(\hat{a}_k^\dagger \hat{b}_k - \hat{a}_k \hat{b}_k^\dagger), \quad (2.8.2)$$

making the substitution  $\hat{b}_k = |\alpha_{\text{LO}}|e^{i\phi_{\text{LO}}} + \delta\alpha_{\text{LO}}$  we have

$$\hat{i}_- \approx |\alpha_{\text{LO}}|\hat{x}(\phi_{\text{LO}}), \quad (2.8.3)$$

neglecting the contributions of  $\delta\alpha_{\text{LO}}$ . The photocurrent  $\hat{i}_-$  measures a signal proportional to the input field quadrature projected on the local oscillator phase angle. The photocurrent variance is given by

$$\text{Var}[\hat{i}_-^2] \approx |\alpha_{\text{LO}}|^2 \text{Var}[\hat{x}(\phi_{\text{LO}})]. \quad (2.8.4)$$

The noise reference is the vacuum as the input signal in the homodyne detection scheme, see Fig.

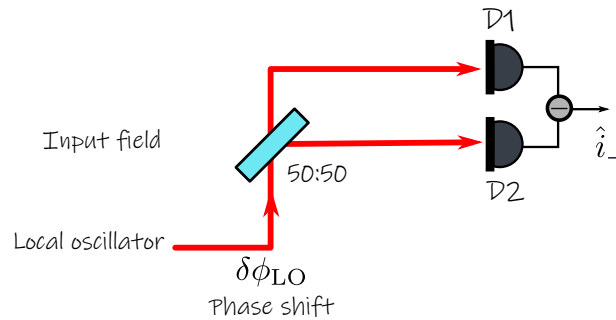


Figure 2.5: Balanced homodyne detection scheme. A 50:50 BS mixes a local oscillator to the field we want to study. The two outputs are detected and the photocurrents subtracted. By varying the local oscillator phase, we can measure the input field quadratures in any angle.

2.5. In this case, the fluctuation of the two detectors' photocurrent subtraction will be proportional to the vacuum noise. The fluctuation of the sum of the photocurrent will correspond to a measure of amplitude noise of the local oscillator. Once the value of shot noise is calibrated for several input powers, at a given analysis frequency  $\Omega$ , this value becomes the unit of noise for the respective LO



power. This value normalizes all variances. Thus, we will have the correspondence

$$\mathcal{S}[\hat{x}_\theta, \Omega] \begin{cases} > 1 & \Rightarrow \text{excess of noise;} \\ = 1 & \Rightarrow \text{shot noise;} \\ < 1 & \Rightarrow \text{squeezing.} \end{cases} \quad (2.8.5)$$

## 2.9 Quantum teleportation

Quantum teleportation is the process of transference of an unknown quantum state  $\hat{\rho}_{\text{in}}$  from one location to another, Fig. 2.6. This task can be performed using two channels: a classical channel and a quantum channel. A classical channel is a way to send information using physical resources that obey classical physics. A quantum channel, in this case, is an entangled bipartite state shared by the sender (Alice) and the receiver (Bob). Alice measures her sub-system and sends information to Bob that acts on his available system preparing a copy of the initial unknown state. As a consequence of Alice measurement and the sending-receiving time, the original state is destroyed in the process, and no cloning of a quantum state neither superluminal communication happens [30]. Teleportation plays an important role in quantum information; it is the fundamental ingredient in many quantum technology implementations such as quantum repeaters and quantum computing [13].

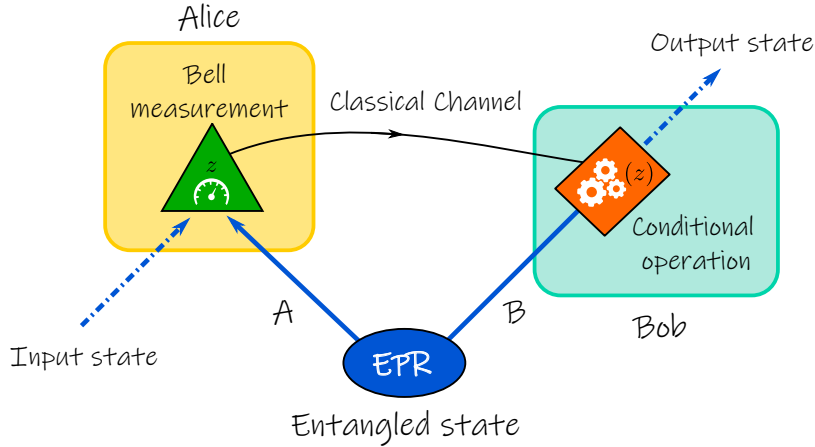


Figure 2.6: Basic quantum teleportation scheme. An EPR quantum state is shared between Alice and Bob. This forms the quantum channel in the teleportation protocol. Alice has an input state she wants to send to Bob. She performs a Bell measurement and sends the result to Bob through a classical channel. Bob operates in his part of the EPR state conditioned by the message he receives from Alice. In the end, the output state is a copy of Alice's input state with a given fidelity.

To understand the quantum teleportation protocol, we describe the ideal discrete variable case, first presented by Bennet *et al.* in 1993 [67]. We follow the description presented in [68]. Consider a pair of qubits  $A$  and  $B$  as our quantum channel, prepared in an entangled state

$$|\psi\rangle_{AB} = \frac{|0\rangle_A |1\rangle_B - |1\rangle_A |0\rangle_B}{\sqrt{2}}, \quad (2.9.1)$$

and a unknown general pure state  $|\psi\rangle_{\text{in}} = a|0\rangle_{\text{in}} + b|1\rangle_{\text{out}}$  to be teleported. It is necessary to couple the initial state with the EPR pair in order to transmit information through the quantum channel. This is achieved by Alice when she performs a Bell measurement, which is a joint measurement over

$|\psi\rangle_{\text{in}}$  and the  $A$ -qubit given by the projection on the Bell basis

$$|\psi^\pm\rangle = \frac{|0\rangle_{\text{in}}|1\rangle_A \pm |1\rangle_{\text{in}}|0\rangle_A}{\sqrt{2}}, \quad (2.9.2)$$

$$|\phi^\pm\rangle = \frac{|0\rangle_{\text{in}}|0\rangle_A \pm |1\rangle_{\text{in}}|1\rangle_A}{\sqrt{2}}, \quad (2.9.3)$$

The total state  $|\psi_T\rangle$  before the measurement can be written in terms of the Bell basis as

$$|\psi_T\rangle = \frac{1}{2} [|\phi^-\rangle (\hat{\sigma}_x |\phi\rangle_B) + |\phi^+\rangle (\hat{\sigma}_x \hat{\sigma}_z |\phi\rangle_B) - |\psi^-\rangle |\psi\rangle_B - |\psi^+\rangle (\hat{\sigma}_z |\psi\rangle_B)], \quad (2.9.4)$$

where

$$\hat{\sigma}_x \equiv \begin{pmatrix} 0 & 1 \\ 1 & 0 \end{pmatrix}, \quad \text{and} \quad \hat{\sigma}_z \equiv \begin{pmatrix} 1 & 0 \\ 0 & -1 \end{pmatrix}, \quad (2.9.5)$$

are the usual Pauli operators. The outcomes of the Bell measurement have equal probabilities and after the measurement the state projected in Bob station is going to be one of the states  $\hat{\sigma}_x |\psi\rangle_B$ ,  $\hat{\sigma}_x \hat{\sigma}_z |\psi\rangle_B$ ,  $-\hat{\sigma}_z |\psi\rangle_B$ ,  $-\hat{\sigma}_z |\psi\rangle_B$ , with a unique correspondence between each measurement and projection. Alice can communicate to Bob the outcome of her measurements in time to Bob apply a specific transformation on his state and recover the original  $|\psi\rangle_{\text{in}}$  state. However, there are always imperfections affecting the teleportation protocol's quality in real life, implying a mismatch between Bob's state in the output and the initial state. A measure of the protocol quality is called fidelity, which is defined as

$$F \equiv \text{Tr} \left\{ \sqrt{\hat{\rho}_{\text{in}} \hat{\rho}_{\text{out}}} \sqrt{\hat{\rho}_{\text{in}}} \right\}, \quad (2.9.6)$$

and for a pure state it becomes  $F = \langle \psi | \hat{\rho}_{\text{out}} | \psi \rangle$ . A minimum fidelity for assure that quantum resources was used has been given by [69]. For qubits, the use of pure classical channels can give at most  $F = 2/3$ , therefore the region  $2/3 < F \leq 1$  correspond to pure quantum channel.

### 2.9.1 Quantum teleportation in CV

We will explain the ideal quantum teleportation with continuous variables, following [68]. It uses a perfect EPR state, which can not be created in a laboratory because it requires infinite resources. However, the ideal case illustrates the protocol's most critical aspects. It follows in the steps:

Initial conditions: Alice and Bob share an ideal EPR state. The perfect correlations can be expressed as

$$\hat{x}_a - \hat{x}_b = \hat{y}_a + \hat{y}_b = 0. \quad (2.9.7)$$

The unknown state that Alice wants to teleport is described with the quadratures  $\hat{x}_{\text{in}}$  and  $\hat{y}_{\text{in}}$ .

Bell measurement and classical communication: Alice realizes the CV Bell measurement. To do so, Alice needs to perform two steps: mix with a BS operation the a-mode and in-mode and perform a homodyne detection. The BS output is going to be

$$\hat{x}_\pm = (\hat{x}_a \pm \hat{x}_{\text{in}})\sqrt{2}, \quad \hat{y}_\pm = (\hat{y}_a \pm \hat{y}_{\text{in}})\sqrt{2}, \quad (2.9.8)$$

where “+” and “-” label the two ports of the BS. Subsequently, Alice measures the  $\hat{x}_-$  and  $\hat{y}_+$  causing the projection for Alice

$$\hat{x}_a = \hat{x}_{\text{in}} + \sqrt{2}x_-, \quad \hat{y}_a = -\hat{y}_{\text{in}} + \sqrt{2}y_-, \quad (2.9.9)$$

and revealing that for Bob, the relations

$$\hat{x}_b = \hat{x}_{\text{in}} + \sqrt{2}x_-, \quad \hat{y}_b = \hat{y}_{\text{in}} - \sqrt{2}y_-, \quad (2.9.10)$$

should be valid. Alice sends Bob the information of her measurements  $(x_-, y_+)$  using the classical channel.

Conditional operation: using the information provided by Alice, Bob performs a conditional displacement operation on his b-mode

$$\hat{x}_b \longrightarrow \hat{x}'_b \equiv \hat{x}_{\text{in}} - \sqrt{2}x_- = \hat{x}_{\text{in}}, \quad (2.9.11)$$

$$\hat{y}_b \longrightarrow \hat{y}'_b \equiv \hat{y}_{\text{in}} + \sqrt{2}y_- = \hat{y}_{\text{in}}, \quad (2.9.12)$$

thus completing the protocol once the new displaced quadratures  $(\hat{x}'_b, \hat{y}'_b)$  are equal to the initial operators  $(\hat{x}_{\text{in}}, \hat{y}_{\text{in}})$ , therefore the ideal case teleports an unknown state with fidelity  $F = 1$ . In a real situation there are always defects that decrease the fidelity. For a pure initial state, the fidelity takes the form

$$F = \pi \int d^2\alpha \mathcal{W}^{\text{in}}(\alpha) \mathcal{W}^{\text{out}}(\alpha), \quad (2.9.13)$$

one can show that using a two-mode quantum channel the fidelity of a teleportation of coherent states has the optimal fidelity

$$F^{\text{coh}} = \frac{1}{\sqrt{(1 + \text{Var}[\hat{x}_{\text{EPR}}])(1 + \text{Var}[\hat{y}_{\text{EPR}}])}}. \quad (2.9.14)$$

Where  $\hat{x}_{\text{EPR}} = \hat{x}_a - \hat{x}_b$  and  $\hat{y}_{\text{EPR}} = \hat{y}_a + \hat{y}_b$ . In the particular case of coherent state teleportation, the maximum fidelity using only classical resources is  $F = 1/2$ . Where to have  $F^{\text{coh}} > 1/2$  the quantum channel has to present entanglement. A violation of Duan criterion would automatically give  $F^{\text{coh}} > 1/2$ . Today the fidelity record in CV is  $F = 0.83$  [70].

## Chapter 3

# Optical Parametric Oscillator

Nonclassical states of light in the CV domain play an essential role in the field of quantum information and quantum optics [71, 72]. The squeezed state is the best-known nonclassical state in CV. In the same class, the two-mode squeezed state has EPR correlations between two different optical modes. The entanglement is an essential feature in the fundamentals of quantum information and future applications in communication technology. Much of the research efforts in quantum optics and quantum information focus on finding sources of such states to manipulate them to serve future quantum technology applications. The optical parametric oscillator can efficiently generate squeezing or entanglement among the three fields involved in the parametric conversion process. That is why OPO is such an interesting device from the application point of view. This chapter will present the quantum theory of the OPO, calculate the noise spectra, and verify the expected violation of some entanglement criteria.

The first formal quantum treatment of parametric oscillators is given in [73, 74], just after the invention of the laser. Soon, an optical parametric process was suggested as quantum amplifier [75]. A more standard treatment of parametric oscillator was presented later by Glauber [76, 77], as well as a prediction of squeezed states of light by a degenerated OPO (DOPO) [78, 79]. Kimble *et al.* was the first to use an OPO below the oscillation threshold to generate squeezed light [80]. Quantum correlations above the oscillation threshold were demonstrated in the following year [81]. Reid *et al.* explored the use of Nondegenerated OPO (NOPO) as a source of EPR states of light [82–85]. This was first demonstrated in [86, 87], where the signal and idler fields were distinguished by polarization, adding entanglement in continuous variables of light to the quantum information toolbox. The mentioned experiments were done using tabletop systems. The necessity of scalable systems drives the miniaturization of such systems. Example of this effort are squeezing in waveguides [88–91], microring resonators [92–94] and whispering gallery mode resonators [95–98].

It took more than 20 years since the first generation of EPR states from an OPO [86, 87] to achieve two-color entanglement in continuous variables [99]. Three-color entanglement was also achieved between pump, signal, and idler by [100]. Recently, entanglement among six modes was also demonstrated [101, 102]. Moreover, using cluster states [103] multipartite entanglement among millions of optical modes can be generated [104, 105]. The OPO, despite being one of the most studied quantum optics tools, still produce novelties in quantum state generation.

### 3.1 Quantum description of OPOs

The presence of the nonlinear medium couples the modes of the pump, signal, and idler fields in the OPO cavity. We describe the triply resonant optical parametric oscillator (TROPO), where all fields are resonant inside the optical cavity. More fundamentally, we can say that a pump photon is annihilated, and simultaneously, two photons (signal and idler) are created; the reverse also occurs.

The description of this process is made by the interaction Hamiltonian [23]

$$\hat{V} = 2i\hbar\frac{\chi}{\tau}(\hat{a}_0^\dagger\hat{a}_1\hat{a}_2 - \hat{a}_0\hat{a}_1^\dagger\hat{a}_2^\dagger), \quad (3.1.1)$$

where  $\hat{a}_j$ ,  $j \in \{0, 1, 2\}$ , represents the annihilation operators of the pump, signal, and idler fields respectively. The proportionality constant  $\chi$  describes second-order nonlinear susceptibility and phase matching, whereas  $\tau$  is the time at which a photon performs a complete round trip in the cavity. In addition to the interaction, we need to include the Hamiltonian for each quantized field independently. In the interaction representation of the field, this is done by operators

$$\hat{H}_j = \hbar\frac{2\gamma'_j}{\tau}\Delta_j\hat{a}_j^\dagger\hat{a}_j, \quad (3.1.2)$$

where  $\Delta_j = (\omega_j - \omega_{cj})/\delta\omega_{cj}$  represents the detuning between the nearest frequency of the cavity and the frequency of the mode  $j$ , normalized by the bandwidth  $\delta\omega_{cj} = 2\gamma'_j/\tau$ , and  $\gamma'_j = \gamma_j + \mu_j$ . The intracavity pumping field is related to the classical driving field of the input  $\alpha_0^{\text{in}}$ , entering the cavity through the coupling port of the pump mode

$$\hat{H}_{\text{in}} = i\hbar\frac{\sqrt{2\gamma_0}}{\tau}\alpha_0^{\text{in}}(\hat{a}_0 - \hat{a}_0^\dagger). \quad (3.1.3)$$

We consider an input field described by a coherent state. The total Hamiltonian governs the OPO's dynamics

$$\hat{H} = \sum_j \hat{H}_j + \hat{H}_{\text{in}} + \hat{V}. \quad (3.1.4)$$

The OPO is an open quantum system. Consequently, it interacts with a reservoir of harmonic oscillators in thermal equilibrium that introduces losses and adds noise to the system. In this way, the temporal evolution can be described by the master equation [23, 106]

$$i\hbar\frac{d\hat{\rho}}{dt} = [\hat{H}, \hat{\rho}] + \sum_j \hat{\Lambda}_j\hat{\rho}, \quad (3.1.5)$$

where  $\hat{\Lambda}_j$  are the Lindblad operators that describe the coupling with the environment and are given by

$$\hat{\Lambda}_j\hat{\rho} = \frac{\gamma'_j}{\tau}(2\hat{a}_j\hat{\rho}\hat{a}_j^\dagger - \hat{a}_j^\dagger\hat{a}_j\hat{\rho} - \hat{\rho}\hat{a}_j^\dagger\hat{a}_j). \quad (3.1.6)$$

The standard procedure for solving (3.1.6) involves replacing the field operators with complex variables. Rewriting it in terms of a quasiprobability function to obtain a result that can be recognized as a Fokker-Planck equation. Then, associate the Fokker-Planck equation with a stochastic Langevin's equation [106]. Different representations of the density operator can be used, such as Glauber-Sudarshan's  $P$  representation, Wigner's representation, and Husimi's  $Q$ . They differ by interpretation and existence of singularities for different operating regimes of the OPO [107]. We use the Wigner representation, described in section 2.5.5. By doing the substitution of  $(\hat{a}_j, \hat{a}_j^\dagger)$  by complex variables

$(\alpha_j, \alpha_j^*)$  with the rules presented in [106], the Wigner function  $\mathcal{W}(\boldsymbol{\alpha})$  obeys the equation

$$\begin{aligned} \frac{d}{dt}\mathcal{W}(\boldsymbol{\alpha}) = & \left[ \sum_j \gamma_j (1 + i\Delta_j) \left( \frac{\partial}{\partial \alpha_j^*} \alpha_j^* - \frac{\partial}{\partial \alpha_j} \alpha_j \right) - \sqrt{2\gamma_0} \alpha_e \left( \frac{\partial}{\partial \alpha_0^*} + \frac{\partial}{\partial \alpha_0} \right) \right. \\ & + 2\chi \left( \alpha_1 \alpha_2 \frac{\partial}{\partial \alpha_0^*} + \alpha_1^* \alpha_2^* \frac{\partial}{\partial \alpha_0} - \alpha_0 \alpha_1 \frac{\partial}{\partial \alpha_2} - \alpha_0^* \alpha_1^* \frac{\partial}{\partial \alpha_2^*} - \alpha_0 \alpha_2^* \frac{\partial}{\partial \alpha_1} \right. \\ & \left. \left. - \alpha_0^* \alpha_2 \frac{\partial}{\partial \alpha_1^*} \right) + \sum_j \gamma_j' \frac{\partial^2}{\partial \alpha_j \alpha_j^*} - \frac{\chi}{2} \left( \frac{\partial^3}{\partial \alpha_0^* \alpha_1^* \alpha_2^*} + \frac{\partial^3}{\partial \alpha_0 \alpha_1 \alpha_2} \right) \right] \mathcal{W}(\boldsymbol{\alpha}), \end{aligned} \quad (3.1.7)$$

where  $\boldsymbol{\alpha} = (\alpha_0, \alpha_0^*, \alpha_1, \alpha_1^*, \alpha_2, \alpha_2^*)$ . This equation can be recognized as a Fokker-Planck equation if we disregard the terms involving third-order derivatives, which can be assumed to be very small [108]. In the case of large  $\chi$ , this approximation can not be assumed. We arrive at

$$\frac{d}{dt}\mathcal{W}(\boldsymbol{\alpha}) = \left[ - \sum_j \frac{\partial}{\partial \alpha_j} A_j + \frac{1}{2} \sum_{j,k} \frac{\partial}{\partial \alpha_j} \frac{\partial}{\partial \alpha_k} D_{jk} \right] \mathcal{W}(\boldsymbol{\alpha}), \quad (3.1.8)$$

where  $A_j$  is a component of the drag vector  $\mathbf{A}$ , carrying information on the mean values. The coefficients  $D_{jk}$  are elements of diffusion matrix  $\mathbb{D} = \mathbb{B}\mathbb{B}^T$ , responsible for the diffusion of the average values, therefore, to their fluctuations. Once obtained the Fokker-Planck equation, the equivalent Langevin's equation takes the form

$$\frac{d\boldsymbol{\alpha}}{dt} = \mathbf{A} + \mathbb{B}\mathbf{s}(t), \quad (3.1.9)$$

where  $\mathbf{s}(t)$  is a stochastic fluctuation vector with null mean value and correlation  $\langle s_i(t) s_j(t') \rangle = \delta_{ij} \delta(t - t')$ . A more detailed treatment is described in several references [109–113]. We then obtain the set of equations for intracavity complex amplitudes

$$\tau \frac{d}{dt} \alpha_0 = -\gamma_0' (1 - i\Delta_0) \alpha_0 - 2\chi \alpha_1 \alpha_2 + \sqrt{2\gamma_0} \alpha_0^e + \sqrt{2\mu_0} \delta v_0, \quad (3.1.10)$$

$$\tau \frac{d}{dt} \alpha_1 = -\gamma_1' (1 - i\Delta_1) \alpha_1 + 2\chi \alpha_0 \alpha_2^* + \sqrt{2\gamma_1} \delta u_1 + \sqrt{2\mu_1} \delta v_1, \quad (3.1.11)$$

$$\tau \frac{d}{dt} \alpha_2 = -\gamma_2' (1 - i\Delta_2) \alpha_2 + 2\chi \alpha_0 \alpha_1^* + \sqrt{2\gamma_2} \delta u_2 + \sqrt{2\mu_2} \delta v_2, \quad (3.1.12)$$

the terms  $\delta v_j$  and  $\delta u_j$  correspond to vacuum fluctuations that are coupled to the system by spurious losses and the transmissions of the output mirror, respectively. We rewrite the amplitudes in terms of an average value and a fluctuation

$$\alpha_j(t) = \alpha_j + \delta \alpha_j(t), \quad \alpha_j = \langle \alpha_j(t) \rangle = p_j e^{i\varphi_j}. \quad (3.1.13)$$

Our goal is to study the fluctuations  $\delta \alpha_j$  where it is assumed that  $|\alpha_j| \ll |\delta \alpha_j|$ . In terms of quadratures the fields are given by

$$\alpha_j(t) = \frac{e^{i\phi_j}}{2} [p_j(t) + iq_j(t)], \quad (3.1.14)$$

which defines the fluctuations in  $\delta p_j(t)$  and  $\delta q_j(t)$

$$\delta \alpha_j(t) = \frac{e^{i\phi_j}}{2} [\delta p_j(t) + i\delta q_j(t)], \quad (3.1.15)$$

remembering that these fluctuations are in the rotating reference for each mode.

### 3.1.1 Mean values

The stationary solution is found by taking the temporal mean of (3.1.10) – (3.1.12). We thus obtain the same equations for the field amplitudes in the classically treated steady state. Following the treatment presented in [114], we have

$$\alpha_0 \gamma'_0 (1 - i\Delta_0) = -2\chi^* \alpha_2 \alpha_1 + \sqrt{2\gamma_0} \alpha_0^e, \quad (3.1.16)$$

$$\alpha_1 \gamma'_1 (1 - i\Delta_1) = 2\chi \alpha_0 \alpha_2^*, \quad (3.1.17)$$

$$\alpha_2 \gamma'_2 (1 - i\Delta_2) = 2\chi \alpha_0 \alpha_1^*, \quad (3.1.18)$$

describing classical properties of OPOs. For sufficiently high amplitudes, it is expected that the results obtained for the mean value of the fields in the quantum treatment will agree with all the results obtained in the classical treatment. It is easy to see that the phases are related by

$$p_0 = \frac{1}{|\chi|} \sqrt{\gamma'_1 \gamma'_2 [1 + \Delta_1 \Delta_2 + i(\Delta_1 - \Delta_2)]} e^{-i(\phi_0 - \phi_+)} \quad (3.1.19)$$

where  $\phi_+ \equiv \phi_1 + \phi_2$ . We will then analyze the oscillation conditions of the triple resonant OPO. Multiplying the (3.1.17) by the conjugate of the equation (3.1.18) we have

$$\gamma'_1 \gamma'_2 (1 - i\Delta_1)(1 - i\Delta_2) = 4|\chi|^2 |\alpha_0|^2, \quad (3.1.20)$$

taking only the imaginary part of the equation above we arrive at the condition

$$\Delta_1 = \Delta_2 = \Delta, \quad (3.1.21)$$

thus the ratio between the normalized detunings for the total losses must be the same for the two fields generated. This is a nontrivial characteristic of the doubly resonant and triply resonant optical parametric oscillators. We can show that

$$2\gamma'_1 |\alpha_1|^2 (1 - \Delta_1) = 2\gamma'_2 |\alpha_2|^2 (1 - \Delta_2), \quad (3.1.22)$$

knowing that the number of photons coming out of the cavity in the modes  $j = 1, 2$  per unit of time is proportional to

$$|\alpha_j^s|^2 = 2\gamma'_j |\alpha_j|^2. \quad (3.1.23)$$

The condition imposed by (3.1.22) can be translated as follows: in the steady-state, the total number of photons coming out of the cavity, including spurious losses, must be equal for the two fields. Calculating the ratio between photon flux in each output mode, we have

$$\frac{\gamma'_1 |\alpha_1|}{\gamma'_2 |\alpha_2|} = \frac{\gamma_1 \gamma'_1}{\gamma_2 \gamma'_2}. \quad (3.1.24)$$

Spurious losses introduce an imbalance between the field outputs in the frequencies  $\omega_1$  and  $\omega_2$ . The real part of the equation (3.1.20), taking into account the condition (3.1.21), leads to

$$p_0^2 = \frac{\gamma'_1 \gamma'_2 (1 + \Delta^2)}{4|\chi|^2}, \quad (3.1.25)$$

showing that the intracavity pump field is independent of the pump power above the threshold. Substituting the equation above into the equation (3.1.16), we find for the oscillation threshold the

expression

$$p_{\text{th}}^{\text{in}} = \sqrt{\frac{\gamma_0'^2 \gamma_1' \gamma_2'}{8|\chi|^2 \gamma_0} (1 + \Delta^2)(1 + \Delta_0^2)}. \quad (3.1.26)$$

The detuning plays the role of increasing the oscillation threshold.

### 3.1.2 Signal and idler output power

To find the expressions of the fields  $\alpha_1$  and  $\alpha_2$  above the threshold, we will define a new variable  $\sigma$ , which is the ratio between the pumping and threshold power in the condition where  $\Delta = \Delta_0 = 0$  as

$$\sigma = \frac{|\alpha_0^{\text{in}}|^2}{|\alpha_0^{\text{in}}|_{\text{th}}^2}. \quad (3.1.27)$$

The expression for the threshold with this normalization is

$$\sigma_{\text{th}} = (1 + \Delta^2)(1 + \Delta_0^2) = (\Delta + \Delta_0)^2 + (1 - \Delta\Delta_0)^2. \quad (3.1.28)$$

Substituting  $\alpha_2$  for (3.1.18) into (3.1.16) we obtain

$$\left[ (1 - i\Delta_0)(1 - i\Delta_1) + \frac{4|\chi|^2 |\alpha_1|^2}{\gamma_2' \gamma_0'} \right] \alpha_0 = (1 - i\Delta) \frac{\sqrt{2\gamma_0}}{\gamma_0'} \alpha_0^{\text{in}}, \quad (3.1.29)$$

taking the square of the above equation and replacing  $|\alpha_0|^2$  with (3.1.25) we find

$$\left( 1 - \Delta\Delta_0 + \frac{4|\chi|^2 |\alpha_1|^2}{\gamma_2' \gamma_0'} \right) + (\Delta + \Delta_0)^2 = \sigma. \quad (3.1.30)$$

The output power of the signal and idler beams can be calculated as

$$I_1 = \frac{\gamma_0' \gamma_1' \gamma_2'}{4|\chi|^2} \left[ \sqrt{\sigma - (\Delta_0 + \Delta)^2} + \Delta\Delta_0 - 1 \right], \quad (3.1.31)$$

$$I_2 = \frac{\gamma_0' \gamma_1' \gamma_2'}{4|\chi|^2} \left[ \sqrt{\sigma - (\Delta_0 + \Delta)^2} + \Delta\Delta_0 - 1 \right], \quad (3.1.32)$$

and the total power is given by  $P_{\text{out}} = I_1 + I_2$ . Considering the degenerate case, where  $\gamma_1 = \gamma_2 = \gamma$ , and  $\gamma_1' \gamma_2' = \gamma'$ , (3.1.26) for the threshold power becomes

$$P_{\text{th}} = \hbar\omega_0 \frac{\gamma_0'^2 \gamma'^2}{8|\chi|^2 \gamma_0}. \quad (3.1.33)$$

In this case, the output power at resonance is given by

$$P_{\text{out}} = \hbar\omega_0 \left[ \frac{\gamma\gamma'\gamma_0}{2|\chi|^2} (\sqrt{\sigma} - 1) \right] = 4\eta_{\text{max}} P_{\text{th}} \left( \sqrt{\frac{P_{\text{in}}}{P_{\text{th}}}} - 1 \right). \quad (3.1.34)$$

The maximum efficiency is defined as  $\eta_{\text{max}} = \eta_s \eta_0$ , where  $\eta_0 = \gamma_0/\gamma_0'$ ,  $\eta_s = \gamma/\gamma'$  is the ratio between losses by coupling mirrors and total losses. The efficiency depends on the ratio of the pump power to the threshold power. It is maximal at  $\sigma = 4$ , and if we have a lossless system,  $\eta_s = \eta_0 = 1$ , and all pumping light is downconverted. Interesting quantum properties are observed in this condition [115], as a maximal value of the squeezing for the pump field. The challenge in achieving this condition lies



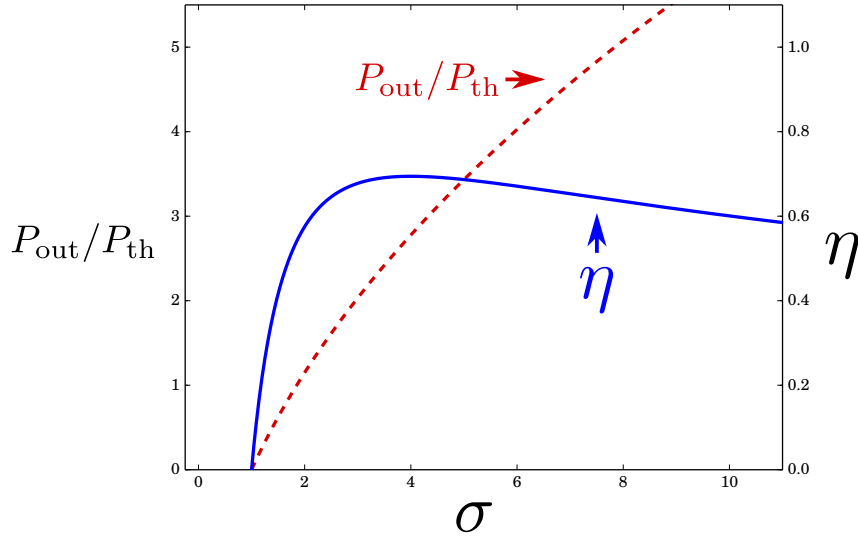


Figure 3.1: Output power and efficiency in function of  $\sigma$ . The threshold power normalizes the output power, and it was considered  $\eta_s = \eta_0 = 0.83$ .

primarily in the technicalities of reducing spurious losses and in the mode coupling of the pump laser with the resonant mode of the cavity. In Fig. 3.1 we can observe the efficiency dependence with  $\sigma$ , reaching its maximum value for  $\sigma = 4$  and presenting a slight decrease to larger values, however remaining close to the maximum for values of up to  $\sigma = 10$ .

### 3.1.3 Linearization

The dynamics of the fluctuations are obtained by replacing the fields by their mean values and their fluctuations, as shown in (3.1.13) in (3.1.10) - (3.1.12). Neglecting the second-order terms in the fluctuations [110, 111] we get

$$\tau \frac{d}{dt} \delta \alpha_0 = -\gamma'_0 (1 - i\Delta_0) \delta \alpha_0 - 2\chi p (e^{i\phi_2} \delta \alpha_1 + e^{i\phi_1} \delta \alpha_2) + \sqrt{2\gamma_0} \delta \alpha_0^{\text{in}} + \sqrt{2\mu_0} \delta v_0, \quad (3.1.35)$$

$$\tau \frac{d}{dt} \delta \alpha_1 = -\gamma' (1 - i\Delta) \delta \alpha_1 + 2\chi (p e^{-i\phi_2} \delta \alpha_0 + p_0 e^{i\phi_0} \delta \alpha_2^*) + \sqrt{2\gamma} \delta u_1 + \sqrt{2\mu} \delta v_1, \quad (3.1.36)$$

$$\tau \frac{d}{dt} \delta \alpha_2 = -\gamma' (1 - i\Delta) \delta \alpha_2 + 2\chi (p e^{-i\phi_1} \delta \alpha_0 + p_0 e^{i\phi_0} \delta \alpha_1^*) + \sqrt{2\gamma} \delta u_2 + \sqrt{2\mu} \delta v_2. \quad (3.1.37)$$

If we make the substitution of the parameter  $\chi$  and use the quadrature definitions  $p$  and  $q$ , we arrive at a set of equations that can be directly translated to the frequency space by using the correspondence  $d/dt \rightarrow i\Omega$ . Defining the vectors

$$\delta \mathbf{r}(\Omega) = [\delta p_0(\Omega), \delta q_0(\Omega), \delta p_1(\Omega), \delta q_1(\Omega), \delta p_2(\Omega), \delta q_2(\Omega)]^T, \quad (3.1.38)$$

$$\delta \mathbf{r}_{\text{in}}(\Omega) = [\delta p_0^{\text{in}}(\Omega), \delta q_0^{\text{in}}(\Omega), \delta u_{p_1}(\Omega), \delta u_{q_1}(\Omega), \delta u_{p_2}(\Omega), \delta u_{q_2}(\Omega)]^T, \quad (3.1.39)$$

$$\delta \mathbf{v}(\Omega) = [\delta v_{p_0}(\Omega), \delta v_{q_0}(\Omega), \delta v_{p_1}(\Omega), \delta v_{q_1}(\Omega), \delta v_{p_2}(\Omega), \delta v_{q_2}(\Omega)]^T, \quad (3.1.40)$$

we arrive at the following matrix equation

$$(\mathbb{A} + 2i\Omega' \gamma' \mathbb{I}) \delta \mathbf{r}(\Omega) = \mathbb{T}_{\text{in}} \delta \mathbf{r}_{\text{in}}(\Omega) + \mathbb{T}_v \delta \mathbf{v}(\Omega), \quad (3.1.41)$$

with  $\Omega' = \tau\Omega/2\gamma'$  is the analysis frequency normalized by the cavity bandwidth, and we define the

matrices

$$\mathbb{A} = \begin{pmatrix} \gamma'_0 & \gamma'_0\Delta_0 & \gamma'\beta & -\gamma'\beta\Delta & \gamma'\beta & -\gamma'\beta\Delta \\ -\gamma'_0\Delta_0 & \gamma'_0 & \gamma'\beta\Delta & \gamma'\beta & \gamma'\beta\Delta & \gamma'\beta \\ -\gamma'\beta & -\gamma'\beta\Delta & \gamma' & \gamma'\Delta & \gamma' & \gamma'\Delta \\ \gamma'\beta\Delta & -\gamma'\beta & -\gamma'\Delta & \gamma' & \gamma'\Delta & \gamma' \\ -\gamma\beta & -\gamma'\beta\Delta & -\gamma' & \gamma'\Delta & \gamma' & \gamma\Delta \\ \gamma\beta\Delta & -\gamma'\beta & \gamma'\Delta & \gamma' & -\gamma'\Delta & \gamma' \end{pmatrix}. \quad (3.1.42)$$

with  $\beta \equiv p/p_0$ ,

$$\mathbb{T}_{\text{in}} = \text{diag}[\sqrt{2\gamma_0}, \sqrt{2\gamma_0}, \sqrt{2\gamma}, \sqrt{2\gamma}, \sqrt{2\gamma}, \sqrt{2\gamma}], \quad (3.1.43)$$

and

$$\mathbb{T}_v = \text{diag}[\sqrt{2\mu_0}, \sqrt{2\mu_0}, \sqrt{2\mu}, \sqrt{2\mu}, \sqrt{2\mu}, \sqrt{2\mu}], \quad (3.1.44)$$

defining the matrix the  $\mathbb{M}(\Omega') \equiv \mathbb{A} + 2i\Omega'\gamma'\mathbb{I}$  we can easily find the vector  $\delta\mathbf{r}(\Omega)$  by

$$\delta\mathbf{r}(\Omega) = \mathbb{M}^{-1}(\Omega') [\mathbb{T}_{\text{in}}\delta\mathbf{r}_{\text{in}}(\Omega) + \mathbb{T}_v\delta\mathbf{v}(\Omega)]^T, \quad (3.1.45)$$

and the fluctuations of the output fields are related to the intracavity fluctuations by the input-output theory [23] giving

$$\delta\mathbf{r}_{\text{out}}(\Omega) = -\delta\mathbf{r}_{\text{in}}(\Omega) + \mathbb{T}_{\text{in}}\delta\mathbf{r}(\Omega), \quad (3.1.46)$$

so that the output fluctuations vector becomes

$$\delta\mathbf{r}_{\text{out}}(\Omega) = [\mathbb{T}_{\text{in}}\mathbb{M}^{-1}(\Omega')\mathbb{T}_{\text{in}} - \mathbb{I}] \delta\mathbf{r}_{\text{in}}(\Omega) + \mathbb{T}_{\text{in}}\mathbb{M}^{-1}(\Omega')\mathbb{T}_v\delta\mathbf{v}(\Omega), \quad (3.1.47)$$

the spectral noise matrix of the fluctuations for the three fields in the output of the OPO will be

$$\mathbb{S}_{\text{OPO}} = \langle \delta\mathbf{r}_{\text{out}}(\Omega)\delta\mathbf{r}_{\text{out}}(-\Omega) \rangle. \quad (3.1.48)$$

## 3.2 Twin beams bipartite entanglement

To investigate the occurrence of entanglement between the signal and idler beams, we use the Duan inequality presented in section 2.3. In this case, the EPR pair will be  $\hat{p}_- = (\hat{p}_1 - \hat{p}_2)/\sqrt{2}$  and  $\hat{q}_+ = (\hat{q}_1 + \hat{q}_2)/\sqrt{2}$  and can be expressed by the sum of the variances

$$V_D/2 = \text{Var}[\hat{p}_-] + \text{Var}[\hat{q}_+] \geq 2. \quad (3.2.1)$$

Using the previously calculated values, we can study the behavior of noise spectra and find the regions of inequality violation (3.2.1), Fig. 3.3. The entanglement is expressed in squeezing in  $\hat{p}_-$  and  $\hat{q}_+$ . We see that the criterion shows entanglement in the entire region of parameters presented in 3.3, the maximum violation happens with  $\sigma = 1$  and  $\Omega' = 0$ . This is the quantum correlation that we want to explore for use in a light-matter quantum network.

## 3.3 Tripartite entanglement

The three-color correlations involving pumping, signal, and idler beams can be checked by applying the van Loock and Furusawa criterion as presented in section 2.3. In this case, the most

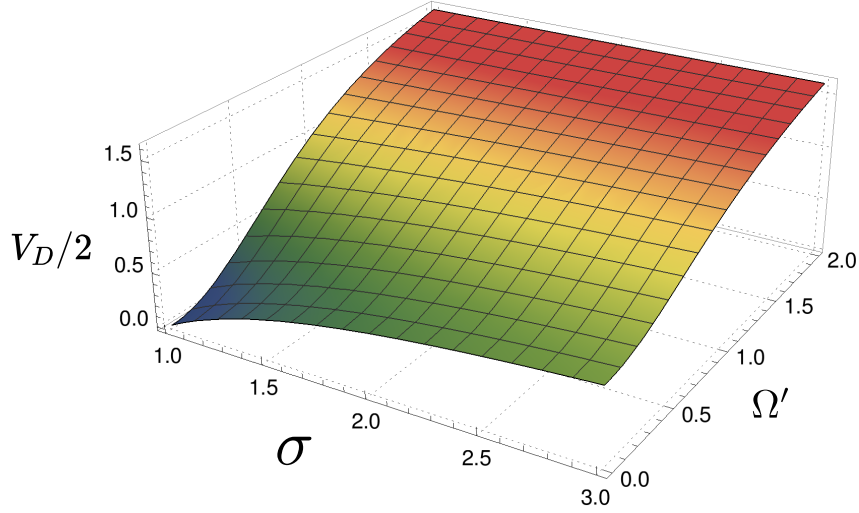


Figure 3.2: Violation of the Duan criteria for signal and idler EPR variables  $\hat{p}_-$  and  $\hat{q}_+$ . The variables  $\sigma$  and  $\Omega'$  are the pumping power normalized by the oscillation threshold and the analysis frequency normalized by the bandwidth of the cavity of the OPO, respectively.

appropriate set of inequalities are [116]

$$V_0 = \text{Var} \left[ \frac{\hat{p}_1 - \hat{p}_2}{\sqrt{2}} \right] + \text{Var} \left[ \frac{\hat{q}_1 + \hat{q}_2}{\sqrt{2}} - c_0 \hat{q}_0 \right] \geq 2, \quad (3.3.1)$$

$$V_1 = \text{Var} \left[ \frac{\hat{p}_0 + \hat{p}_1}{\sqrt{2}} \right] + \text{Var} \left[ \frac{\hat{q}_0 - \hat{q}_1}{\sqrt{2}} - c_2 \hat{q}_2 \right] \geq 2, \quad (3.3.2)$$

$$V_2 = \text{Var} \left[ \frac{\hat{p}_0 + \hat{p}_2}{\sqrt{2}} \right] + \text{Var} \left[ \frac{\hat{q}_0 - \hat{q}_2}{\sqrt{2}} - c_1 \hat{q}_1 \right] \geq 2. \quad (3.3.3)$$

Where the coefficients  $c_j$  we choose in order to minimize the sum of variances. The violation of the above inequalities eliminates the possibility of writing the density operator of the total system as the product of the operator density of each subsystem with the other parts. The violation of two such inequalities is a sufficient condition to demonstrate tripartite entanglement. In fact, in the case of symmetrical losses we have  $V_1 = V_2$ .

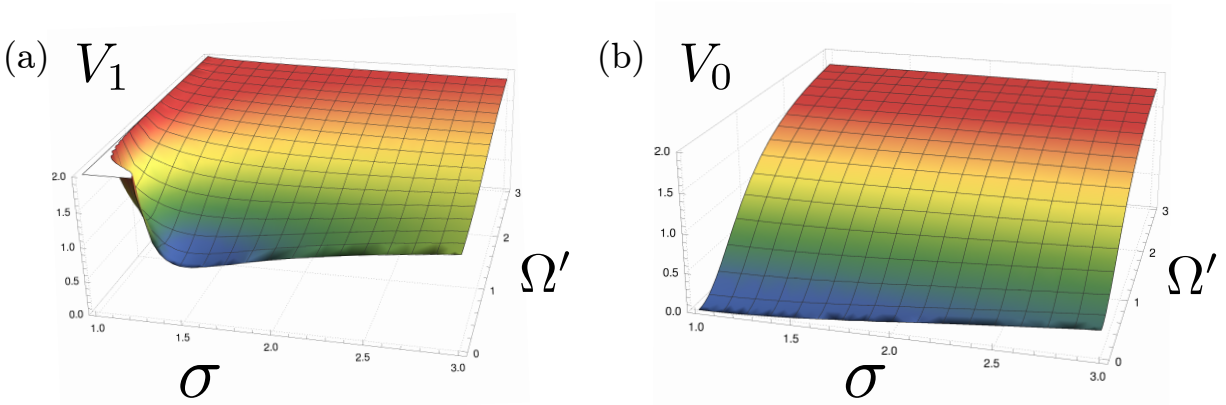


Figure 3.3:  $V_1$  and  $V_0$  in function of  $\sigma$  and  $\Omega'$ . The variables  $\sigma$  and  $\Omega'$  are the pumping power normalized by the oscillation threshold and the analysis frequency normalized by the bandwidth of the cavity of the OPO, respectively.

In 1989 M. Reid proposed an entanglement criterion for continuous variables in bipartite states [83] inspired by the EPR [4] paradox; we know now that this is a quantum steering [117]. Van Loock and Furusawa [45] being generally applied in quantum optics but do not attest to the presence of genuine multipartite entanglement [118]. Just recently a new criterion proposed by [119] using bounds of violations of [45] multipartite entanglement criteria as criteria for genuine multipartite entanglement and genuine steering. The sum

$$V_0 + V_1 + V_2 = \mathcal{I}, \quad (3.3.4)$$

can give us information if the entanglement is genuine. If  $\mathcal{I} < 4$  the system presents genuine tripartite

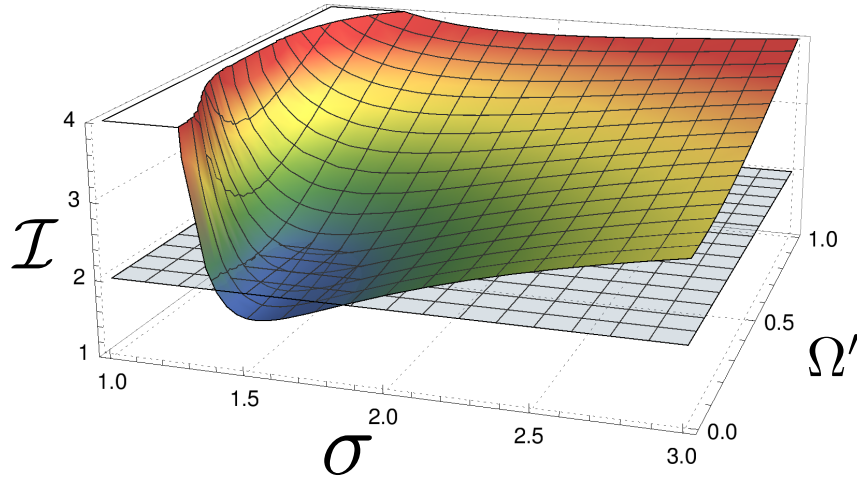


Figure 3.4: Sum of variances  $\mathcal{I}$  for a region of parameters  $\sigma$  and  $\Omega'$ . The variables  $\sigma$  and  $\Omega'$  are the pumping power normalized by the oscillation threshold and the analysis frequency normalized by the bandwidth of the cavity of the OPO, respectively.

entanglement and if  $\mathcal{I} < 2$  the system has genuine tripartite steering. Plotting  $\mathcal{I}$  as a function of  $\sigma$  and  $\Omega'$  makes it clear that OPO is a genuine tripartite source of entanglement for a large region of parameters, and for small frequencies of analysis around  $\sigma = 1.5$  features genuine tripartite steering. This is a new result that has not been published.

### 3.4 Quantum fluctuations in polarization

In this section, we explore the possibility of using the OPO to generate polarization entanglement. Quantum correlations in the polarization degrees of freedom are important in the interface of light and matter in the CV domain [33, 120, 121]. The usual definition of the Stokes operators in quantum optics [122] is

$$\hat{S}_0 = \hat{a}_H^\dagger \hat{a}_H + \hat{a}_V^\dagger \hat{a}_V, \quad (3.4.1)$$

$$\hat{S}_1 = \hat{a}_H^\dagger \hat{a}_H - \hat{a}_V^\dagger \hat{a}_V, \quad (3.4.2)$$

$$\hat{S}_2 = \hat{a}_H^\dagger \hat{a}_V e^{-i\phi} + \hat{a}_V^\dagger \hat{a}_H e^{i\phi}, \quad (3.4.3)$$

$$\hat{S}_3 = i(\hat{a}_H^\dagger \hat{a}_V e^{-i\phi} - \hat{a}_V^\dagger \hat{a}_H e^{i\phi}), \quad (3.4.4)$$

with  $\hat{a}_H$  and  $\hat{a}_V$  the annihilation operators in the polarization  $H$  and  $V$ , respectively. The Stokes

operators obey the angular momentum commutation relations

$$[\hat{S}_1, \hat{S}_2] = 2i\hat{S}_3, \quad [\hat{S}_2, \hat{S}_3] = 2i\hat{S}_1, \quad [\hat{S}_3, \hat{S}_1] = 2i\hat{S}_2, \quad (3.4.5)$$

and

$$[\hat{S}_0, \hat{S}_j] = 0, \quad (j = 1, 2, 3). \quad (3.4.6)$$

Therefore, the simultaneous exact measurement of these Stokes operators is thus impossible. To convert quantum fluctuations from quadratures to Stokes operators, we study the coherent combination of two beams in different polarizations. Consider two fields of the same frequency and transverse mode, combined in a polarizing beamsplitter (PBS), as described in Fig. 3.5. Decomposing the mean field from the fluctuations we will have

$$\hat{a}_H = p_H e^{i\phi_H} + \delta\hat{a}_H, \quad (3.4.7)$$

$$\hat{a}_V = p_V e^{i\phi_V} + \delta\hat{a}_V, \quad (3.4.8)$$

where  $p_H$  and  $p_V$  are the average amplitudes,  $\phi_H$  and  $\phi_V$  the phases of the mean field in polarizations  $H$  and  $V$ , respectively. The Stokes operators expected values for the combined field at the output of

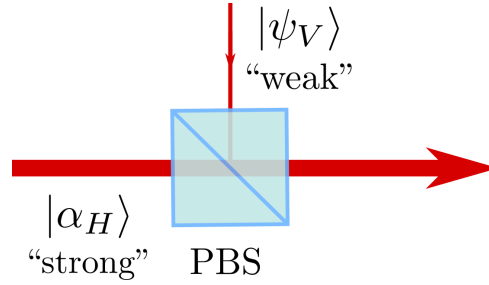


Figure 3.5: Mixing two fields of the same frequency and spatial mode in different polarizations using a polarizing beam splitter (PBS) can convert quadrature noise into polarization noise.

the PBS are given by

$$\langle \hat{S}_0 \rangle = |p_H|^2 + |p_V|^2, \quad (3.4.9)$$

$$\langle \hat{S}_1 \rangle = |p_H|^2 - |p_V|^2, \quad (3.4.10)$$

$$\langle \hat{S}_2 \rangle = 2|p_H||p_V| \cos \phi, \quad (3.4.11)$$

$$\langle \hat{S}_3 \rangle = 2|p_H||p_V| \sin \phi, \quad (3.4.12)$$

where we defined  $\phi \equiv \phi_V - \phi_H$ . In our case  $p_H \gg p_V$ , we can make the substitution  $\hat{S}_1 \rightarrow \langle \hat{S}_1 \rangle$  and write the commutator as

$$\frac{[\hat{S}_2, \hat{S}_3]}{|p_H|^2 - |p_V|^2} = [\hat{s}_2, \hat{s}_3] = 2i, \quad (3.4.13)$$

where we define normalized Stokes operators

$$\hat{s}_2 \equiv \frac{\hat{S}_2}{\sqrt{|p_H|^2 - |p_V|^2}}, \quad (3.4.14)$$

$$\hat{s}_3 \equiv \frac{\hat{S}_3}{\sqrt{|p_H|^2 - |p_V|^2}}, \quad (3.4.15)$$

which obey the same commutation relations. The variances of the Stokes operators neglecting

second-order terms are simply

$$\text{Var}[\hat{S}_0] = p_H^2 \text{Var}[\hat{p}_H(0)] + p_V^2 \text{Var}[\hat{p}_V(0)], \quad (3.4.16)$$

$$\text{Var}[\hat{S}_1] = p_H^2 \text{Var}[\hat{p}_H(0)] - p_V^2 \text{Var}[\hat{p}_V(0)], \quad (3.4.17)$$

$$\text{Var}[\hat{S}_2] = p_H^2 \text{Var}[\hat{p}_V(-\phi)] + p_V^2 \text{Var}[\hat{p}_H(\phi)], \quad (3.4.18)$$

$$\text{Var}[\hat{S}_3] = p_H^2 \text{Var}[\hat{p}_V(-\phi)] + p_V^2 \text{Var}[\hat{p}_H(\phi)]. \quad (3.4.19)$$

This shows that the fluctuations in the amplitude and phase quadratures of the two combined fields contribute to the fluctuations of the Stokes operators. They depend exclusively on the phase difference between the two polarizations and the amplitudes of the fields.

Taking the entangled beams from the OPO, we can study their Stokes operators. Mixing a coherent state in a polarization orthogonal to each OPO output, if the coherent field amplitude is sufficiently large, we can convert the correlations to Stokes operators. Defining the parameter

$$K \equiv \frac{\alpha_{\text{coh}}}{\alpha_{\text{twins}}}, \quad (3.4.20)$$

where  $\alpha_{\text{twins}}$  is the amplitude of the output fields of the OPO and  $\alpha_{\text{coh}}$  is the amplitude of the coherent field being mixed. Using the Duan criterion, we study the criteria violation dependence with the parameter  $K$ . When the value of Duan  $< 2$  we can state that the state is entangled, see Figure 3.6. The

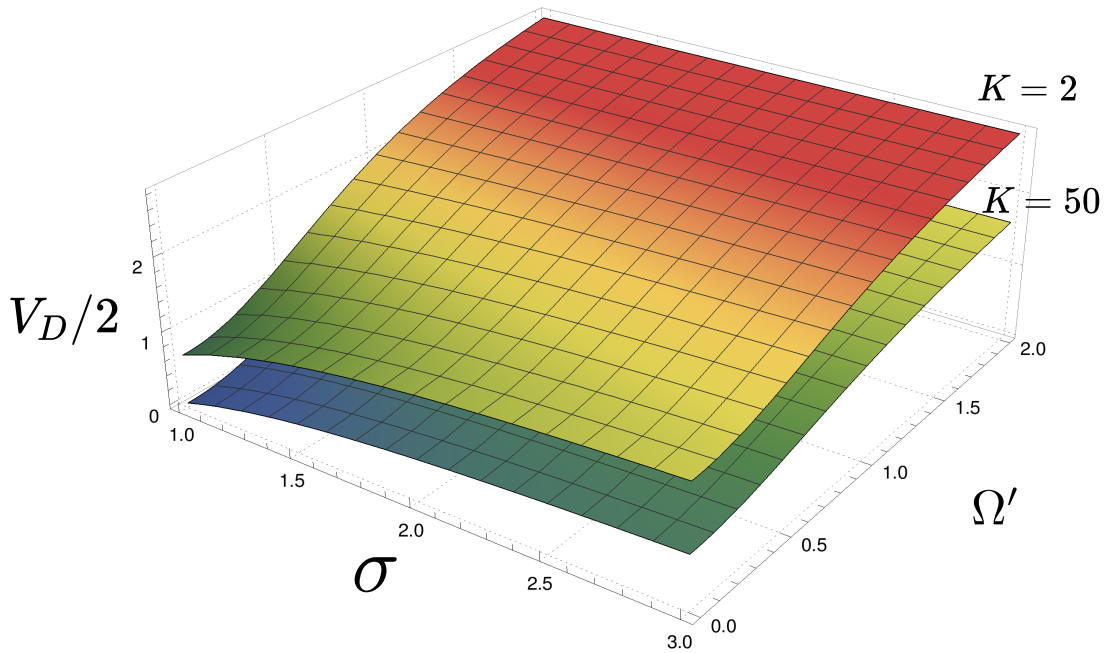


Figure 3.6: Duan criterion for the Stokes operators for different values of the parameter  $K$ , increasing  $K$  we have a better conversion of the violation. The variables  $\sigma$  and  $\Omega'$  are the pumping power normalized by the oscillation threshold and the analysis frequency normalized by the bandwidth of the OPO's cavity, respectively.

prediction shows that we can achieve entanglement between Stokes operators using experimentally reasonable  $K$  values.

### 3.5 Phonon noise

César et al. [123] showed that phonon-light scattering is a source of noise that can frustrate entanglement observation [124]. Thermal fluctuations excite crystal vibrational modes that generate standing or propagating sound waves [125]. Fluctuations of the refractive index lead to phase modulation. Consequently, photons are excited in sidebands adding uncorrelated noise to the dynamics of the parametric process. This is known as spontaneous Brillouin scattering [126]. In this section we follow the description given in [123] to understand the origin of such spurious noise and how to mitigate it.

### 3.5.1 Phonon noise model

A full description of how the perturbations in microscopic degrees of freedom of a solid medium can change the light properties propagating through it is challenging. The effect depends on the solid orientation, geometry, molecular composition, and nature of perturbations. Spontaneous light-scattering is the case where the light itself does not modify the optical properties of the material [126]. The spontaneous process is driven by the material thermal or quantum fluctuations only.

Our interest is to consider the spontaneous Brillouin scattering dependence in our quantum model for the OPO entanglement. We disregard the tensor nature of the dielectric medium and describe the medium perturbation by a modulation in the permittivity as  $\varepsilon = \bar{\varepsilon} + \delta\varepsilon$ . The displacement field is given in terms of the electric field as

$$\mathbf{D} = \bar{\varepsilon}\mathbf{E} + \delta\varepsilon(z, t)\mathbf{E}. \quad (3.5.1)$$

Using Maxwell's equations, we can write the wave equation

$$\nabla^2\mathbf{E} = \mu_0\bar{\varepsilon}\frac{\partial^2}{\partial t^2}\mathbf{E} + \mu_0\frac{\partial^2}{\partial t^2}(\delta\varepsilon\mathbf{E}), \quad (3.5.2)$$

where it is clear that the perturbation in  $\varepsilon$  acts like a source of light waves, generating different sidebands depending on its spectral composition. Describing the single-mode input light as a fast oscillating and slow varying envelope complex field  $\mathcal{E}_j(\mathbf{r}, t)$  part, and considering

$$\mathcal{E}_j(\mathbf{r}, t) = \bar{\mathcal{E}}_j(\mathbf{r}) + \delta\mathcal{E}_j(\mathbf{r}, t), \quad (3.5.3)$$

in the paraxial approximation [123] the local fluctuations of the complex envelope in the frequency domain are given by

$$\delta\mathcal{E}(\mathbf{r}, \Omega) = i\frac{n_j k_j}{2\bar{\varepsilon}_j}\alpha_j u_j^{(g)}(\mathbf{r})\delta\varepsilon_j(\Omega)\delta z, \quad (3.5.4)$$

where  $k_j = \omega_j/c$ ,  $n_j = \sqrt{\varepsilon_j/\varepsilon_0}$  is the medium refractive index,  $\alpha_j$  is the mode amplitude, and  $\alpha_j u_j^{(g)}(\mathbf{r})$  describes the spatial mode of the light beam. We are interested in describing an optical mode inside a resonator so that  $u_j^{(g)}(\mathbf{r})$  is described as one Hermite-Gauss or Laguerre-Gauss mode [127]. The total fluctuation amplitude can be calculated by the integral

$$\delta\alpha_j(z, \Omega) = \int u_j^{(g)*}(\mathbf{r})\delta\mathcal{E}_j(\mathbf{r}, \Omega)d\mathbf{r}. \quad (3.5.5)$$

The above equation now relates the total contribution in a given plane to the fluctuation of the complex number describing the mode. If we now integrate over the total crystal length, we obtain the contribution of phonon noise scattering  $\delta Q_j^{\text{B}}(\Omega)$ . This contribution is in quadrature with  $\alpha_j$ , meaning that no amplitude modulation occurs. Therefore, the effect is only observed in the phase of

the field, and its contribution is given by

$$\begin{aligned}\delta Q_j^B(\Omega) &= i \int \delta \alpha_j(z, \Omega) dz \\ &= \frac{n_j k_j}{2\varepsilon_j} \alpha_j \int |u_j^{(g)}(\mathbf{r})|^2 \delta \varepsilon_j(\mathbf{r}, \Omega) d^3 \mathbf{r}.\end{aligned}\quad (3.5.6a)$$

with noise spectrum given by

$$\langle \delta Q_i^B(\Omega) \delta Q_j^B(-\Omega) \rangle = \frac{n_j k_j n_i k_i}{4\varepsilon_j \varepsilon_i} \sigma_{ji} \alpha_i \alpha_j = \zeta_{ji} \sqrt{P_j P_i}.\quad (3.5.7)$$

We see that the fluctuation in the refractive index originated by pressure waves inside the nonlinear crystal is a source phase noise. The spectral composition of  $\delta \varepsilon_j(\mathbf{r}, \Omega)$  involves two contributions: a broadband noise floor and a succession of narrow peaks. The broadband noise is flat and comes from thermorefractive noise. The narrow peaks are due to scattering by standing pressure waves. The last is a well-known optical fibers effect called guided acoustic wave Brillouin scattering (GAWBS), [128, 129]. A study of Brillouin scattering in a similar PPKTP crystal is done in [130], the theory follows the same treatment of [129, 131] giving good agreement with the experiment.

If the contribution is significant compared with the vacuum noise, this can be the limiting factor for entanglement in OPOs operating above the threshold. As the phonons obey the Bose-Einstein energy distribution, the noise coupling depends linearly over the temperature  $\zeta_{ji} \propto T$ . Considering the measurements of  $\zeta_{ji}$  made by [123, 132]. It is essential to design an OPO to operate with lower optical powers and lower temperatures than the previous designs in our lab [123, 132].

### 3.6 Two-color entanglement source

We extend our work to the specific case of a driven OPO working below the oscillation threshold to produce two-color entangled states. Here the pump beam interacts in a single-pass through the nonlinear crystal. Only the signal and idler wavelengths are resonant in the optical cavity. The description follows the works [133, 134]. We calculate EPR correlations from signal and idler spectrum, including detuning and unbalanced losses. To describe a double resonance OPO below the threshold, we can take (3.1.10) – (3.1.12) and apply adiabatic elimination. This can be effectively done by starting with the interaction Hamiltonian

$$\hat{H}_I = i\hbar \frac{\chi_0}{\tau} \left( e^{i\theta_0} \hat{a}_1^\dagger \hat{a}_2^\dagger - e^{-i\theta_0} \hat{a}_1 \hat{a}_2 \right),\quad (3.6.1)$$

where now the coupling is given by  $\chi_0 = \chi \alpha_0$ , with  $\alpha_0$  the classical pump field obtained by  $\hat{a}_0 \rightarrow \alpha_0$  and  $\theta_0$  is the pump phase. For this model we obtain the Langevin equations:

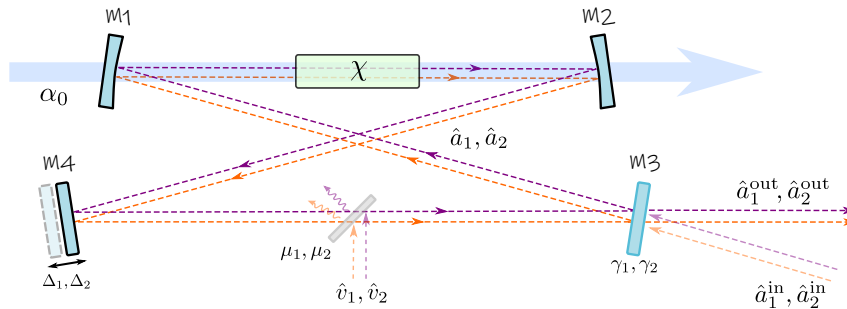


Figure 3.7: NOPO cavity model.



$$\tau \dot{\hat{a}}_j = -\gamma'_j(1 - i\Delta'_j)\hat{a}_j + \chi_0 e^{i\theta_0} \hat{a}_j^\dagger + \sqrt{2\gamma_j} \hat{a}_j^{\text{in}} + \sqrt{2\mu_j} \hat{v}_j, \quad (3.6.2)$$

where  $\gamma'_j = \gamma_j + \mu_j$ , as described in Section 3.1. In the rotating frame of each beam we define the quadratures  $\hat{x}_j(\theta) = \hat{a}_j e^{-i\theta_j} + \hat{a}_j^\dagger e^{i\theta_j}$ , and  $\hat{y}_j(\theta_j) \equiv \hat{x}_j(\theta_j + \pi/2) = i(\hat{a}_j e^{-i\theta_j} - \hat{a}_j^\dagger e^{i\theta_j})$ . We now parametrize the pump field  $\alpha_0 = g\alpha_{\text{th}}$ , where  $\alpha_{\text{th}} = \sqrt{\gamma_1\gamma_2}/|\chi|$  is the oscillation threshold. In a similar fashion as (3.1.35) – (3.1.37), the dynamics in terms of quadrature operators can be written as

$$\tau \dot{\hat{x}}_1(\theta_1) = -\gamma'_1 \hat{x}_1(\theta_1) - \gamma_1 \Delta'_1 \hat{y}_1(\theta_1) + g\sqrt{\gamma'_1\gamma'_2} \hat{x}_2(\theta_0 - \theta_1) + \sqrt{2\gamma_1} \hat{x}_1^{\text{in}}(\theta_1) + \sqrt{2\mu_1} \hat{x}_1^v, \quad (3.6.3)$$

$$\tau \dot{\hat{x}}_2(\theta_2) = -\gamma'_2 \hat{x}_2(\theta_2) - \gamma_2 \Delta'_2 \hat{y}_2(\theta_2) + g\sqrt{\gamma'_1\gamma'_2} \hat{x}_1(\theta_0 - \theta_2) + \sqrt{2\gamma_2} \hat{x}_2^{\text{in}}(\theta_2) + \sqrt{2\mu_2} \hat{x}_2^v. \quad (3.6.4)$$

Here slowly varying vacuum quadrature fields  $\hat{x}_j^{\text{in}}$  and  $\hat{x}_j^v$  were defined, the phase dependence is neglected because the vacuum noise is phase independent. To make the symmetry in the interaction clear, we analyze the  $\phi_\pm = \theta_0/2 \pm \theta$  angles. We rewrite (3.6.3) and (3.6.4) as

$$\tau \dot{\hat{x}}_1(\phi_+) = -\gamma'_1 \hat{x}_1(\phi_+) - \gamma_1 \Delta'_1 \hat{y}_1(\phi_+) + g\sqrt{\gamma'_1\gamma'_2} \hat{x}_2(\phi_-) + \sqrt{2\gamma_1} \hat{x}_1^{\text{in}} + \sqrt{2\mu_1} \hat{x}_1^v, \quad (3.6.5)$$

$$\tau \dot{\hat{x}}_2(\phi_-) = -\gamma'_2 \hat{x}_2(\phi_-) - \gamma_2 \Delta'_2 \hat{y}_2(\phi_-) + g\sqrt{\gamma'_1\gamma'_2} \hat{x}_1(\phi_+) + \sqrt{2\gamma_2} \hat{x}_2^{\text{in}} + \sqrt{2\mu_2} \hat{x}_2^v, \quad (3.6.6)$$

showing that the coupling between the two modes happens only for the phases  $\phi_\pm$ . This effect originates from the parametric process where the relation  $\theta_1 + \theta_2 = \theta_0$  must be satisfied.

We can write the commutator

$$[\hat{x}_m(\phi), \hat{x}_n(\phi')] = -2i \sin(\phi - \phi') \delta_{mn} \quad (3.6.7)$$

where  $\{m.n\} = \{1, 2\}$ . Then we can write a commutator for OPO output quadrature operators:

$$C_+ = [\hat{x}_1(\phi_+) + \hat{x}_2(\phi_-), \hat{x}_1(\phi_+ + \psi) + \hat{x}_2(\phi_- + \psi)] \quad (3.6.8)$$

$$= C_- \quad (3.6.9)$$

$$= [\hat{x}_1(\phi_+) - \hat{x}_2(\phi_-), \hat{x}_1(\phi_+ + \psi) - \hat{x}_2(\phi_- + \psi)] \quad (3.6.10)$$

$$= 4i \sin(\psi), \quad (3.6.11)$$

and the combinations  $\{\hat{x}_1(\phi_+) + \hat{x}_2(\phi_-), \hat{y}_1(\phi_+) + \hat{y}_2(\phi_-)\}$  and  $\{\hat{x}_1(\phi_+) - \hat{x}_2(\phi_-), \hat{y}_1(\phi_+) - \hat{y}_2(\phi_-)\}$  form conjugate observables. A illustration helpful to understand the way that the quadratures are coupled can be seen in Fig. 3.8, where we can see that the difference of projections onto pump phase axis  $\hat{x}_1(\phi_+) - \hat{x}_2(\phi_-)$  as well as sum of projections onto the perpendicular axis  $\hat{y}_1(\phi_+) + \hat{y}_2(\phi_-)$  cancels out. This correlation between the phasor projections taking the pump as a phase reference leads to squeezing.

Taking the Fourier transform of (3.6.5) and (3.6.6), for  $\Delta_1 = \Delta_2 = 0$ , we obtain

$$\mathbb{A} \mathbf{X} = \mathbb{T} \mathbf{X}^{\text{in}} + \mathbb{L} \mathbf{X}^v, \quad (3.6.12)$$

where  $\mathbb{T} = \text{diag}[\sqrt{2\gamma_1}, \sqrt{2\gamma_2}]$ ,  $\mathbb{L} = \text{diag}[\sqrt{2\mu_1}, \sqrt{2\mu_2}]$ , and

$$\mathbb{A} = \begin{bmatrix} \gamma_1 - i\Omega & -g\sqrt{\gamma_1\gamma_2} \\ -g\sqrt{\gamma_1\gamma_2} & \gamma_2 - i\Omega \end{bmatrix}. \quad (3.6.13)$$

We define the vectors for the intracavity quadratures  $\mathbf{X} = [\hat{X}_1(\phi_+), \hat{X}_2(\phi_-)]^T$ , the input fields  $\mathbf{X}_{\text{in}} = [\hat{X}_1^{\text{in}}, \hat{X}_2^{\text{in}}]^T$  and for the spurious vacuum coupled modes  $\mathbf{X}_v = [\hat{X}_1^v, \hat{X}_2^v]^T$ . We are interested

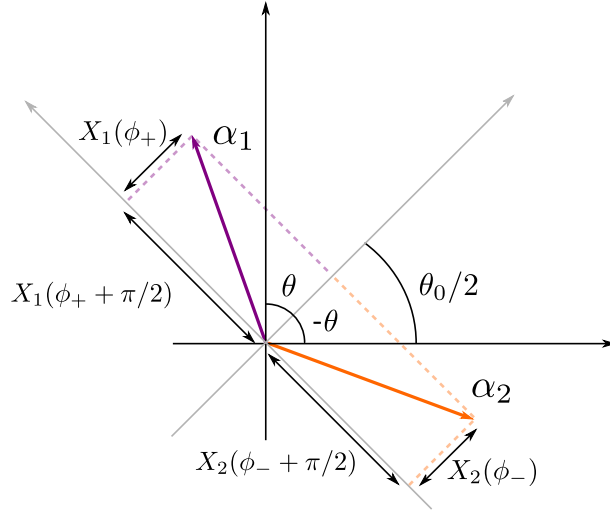


Figure 3.8: Phasor diagram of parametric down-conversion.

in the output quadratures modes, given by the input-output relations [23]

$$\mathbf{X}^{\text{out}} = \mathbb{A}\mathbf{X} - \mathbf{X}_{\text{in}}, \quad (3.6.14)$$

the final output can be written as

$$\mathbf{X}^{\text{out}} = [\mathbb{T}\mathbb{A}^{-1}\mathbb{T} - \mathbb{I}] \mathbf{X}_{\text{in}} + \mathbb{M}^{-1}\mathbb{L}\mathbf{X}_v. \quad (3.6.15)$$

As a illustration, in the case of symmetric losses ( $\gamma_1 = \gamma_2$ ,  $\gamma'_1 = \gamma'_2$ ) we get

$$V_X^\pm = \text{Var} \left[ \frac{\hat{X}_1^{\text{out}} \pm \hat{X}_2^{\text{out}}}{\sqrt{2}} \right] = 1 \pm \eta \frac{4\sqrt{\sigma}}{\tilde{\Omega}^2 + (1 \pm \sqrt{\sigma})^2}, \quad (3.6.16)$$

$$V_Y^\mp = \text{Var} \left[ \frac{\hat{Y}_1^{\text{out}} \mp \hat{Y}_2^{\text{out}}}{\sqrt{2}} \right] = 1 \mp \eta \frac{4\sqrt{\sigma}}{\tilde{\Omega}^2 + (1 \pm \sqrt{\sigma})^2}, \quad (3.6.17)$$

where  $\eta = \gamma/\gamma'$  and  $\tilde{\Omega} = \Omega/\gamma$ , and  $g^2 = \sigma$  (normalized pump power). The modes defined by the subtraction or subtraction of output fields will present noise characteristics following the well-known expression for single-mode squeezing and antisqueezing [23]. Also, it is necessary to take into account the presence of phase noise, that reduces the measured squeezing by projecting antisqueezing into the measured quadrature [135]. This can be described by the rotations

$$V_{\text{pn}}^- = \cos^2(\theta_{\text{RMS}})V_X^- + \sin^2(\theta_{\text{RMS}})V_Y^-, \quad (3.6.18)$$

$$V_{\text{pn}}^+ = \sin^2(\theta_{\text{RMS}})V_X^+ + \cos^2(\theta_{\text{RMS}})V_Y^+, \quad (3.6.19)$$

where  $\theta_{\text{RMS}}$  is the value in RMS of phase noise.

Defining the EPR variables as  $\hat{X}_{\text{EPR}} \equiv (\hat{X}_1^{\text{out}} - \hat{X}_2^{\text{out}})/\sqrt{2}$  and  $\hat{Y}_{\text{EPR}} \equiv (\hat{X}_1^{\text{out}} + \hat{X}_2^{\text{out}})/\sqrt{2}$  we have a separable state between the two outputs of the OPO if the Duan sum of variances

$$V_D/2 = \text{Var}[\hat{X}_{\text{EPR}}] + \text{Var}[\hat{Y}_{\text{EPR}}] \geq 2. \quad (3.6.20)$$

From (3.6.16) and (3.6.17) we see that  $V_D \rightarrow 0$  for  $\{\eta, \sigma, \tilde{\Omega}\} \rightarrow \{1, 1, 0\}$ . Meaning that, assuming a fixed input/output coupler, to obtain a high-quality EPR-state out of the OPO we need a high optical efficiency  $\eta$  — which can be accomplished by reducing the intracavity losses such as imperfect

mirrors, crystal light absorption, and the crystal antireflective (AR) coating. Moreover, the sideband of measurement should be well inside the cavity bandwidth and the pump power as close as possible from the oscillation threshold.

### 3.6.1 Nondegenerated parametric gain

To characterize the parametric interaction strength when operating the system below the oscillation threshold it is necessary to inject a beam in one of the down-converted modes. This beam probes the parametric interaction and is amplified, this is called seeding. In this regime, the OPO is operating as an optical parametric amplifier (OPA). This amplification will depend on the nonlinear interaction strength, the optical cavity parameters, and the pump power. So that a measurement of parametric amplification can tell us the expected degree of quantum correlations.

To obtain a expression for the parametric gain we can change one of the input vacuum fields in (3.6.1) to a classical field. Lets consider the injection of a coherent beam  $\alpha_1^{\text{in}}$ , in the optical cavity from the input/output coupling mirror as in Fig. 3.7,  $\hat{a}_1^{\text{in}} \rightarrow \alpha_1^{\text{in}}$ . Taking the mean values in (3.6.1) and assuming that the pump field is not depleted, we have only a two equation system:

$$\gamma'_1 \alpha_1 = \chi_0 \alpha_2^* + \sqrt{2\gamma_1} \alpha_1^{\text{in}}, \quad (3.6.21)$$

$$\gamma'_2 \alpha_2 = \chi_0 \alpha_1^*. \quad (3.6.22)$$

Solving for  $\alpha_1$  and using the input-output relations the the output field  $\alpha_1^{\text{out}}$  is given by

$$\alpha_1^{\text{out}} = \frac{2\gamma_1/\gamma'_1 - 1}{1 - \sigma} \alpha_1^{\text{in}}, \quad (3.6.23)$$

where  $\sqrt{\sigma} = g$ . We define the parametric gain as the power ration  $\mathcal{G} = |\alpha_1^{\text{out}}|^2 / |\alpha_1^{\text{out}}|_{g=0}^2$  so that the relation of gain and pump power becomes

$$\mathcal{G} = (1 - \sigma)^{-2}. \quad (3.6.24)$$

We see that by (3.6.24), the OPA parametric gain approaches infinity when close the oscillation threshold, so does  $d\mathcal{G}/d\sigma$ . This implies an unstable operation when approaching the threshold. This limits the pump power where the system can operate. As a consequence, limiting the degree of entanglement achievable.

## Part II

# Two-color entanglement



## Chapter 4

# Two-color entanglement experiment

The degenerate OPO (DOPO) is the most efficient source of squeezed states of light [136]. During the last 25 years, it has been the workhorse for quantum information in continuous variables. The degree of control of the parametric process achieved today made it possible to generate high levels of squeezing down to a few Hz [137–139]. Such stable squeezed light sources are used nowadays to enhance the sensibility of interferometric gravitational wave detectors (GWD) [140–144]. However, few works focus on bringing the same technical level to the nondegenerate OPO (NOPO) due to the degree of complexity added to produce and detect CV entanglement in different colors.

We developed a NOPO focusing on two-color entanglement in the audio frequency range. Our goal is to provide the quantum channel necessary to connect Cs atoms and GWD as part of the back action cancellation scheme proposed in [1,28]. This chapter describes this part of the project, as it was developed in the Niels Bohr Institute. It presents the building blocks of our two-color entanglement source and the experimental results showing the generation of an EPR state between 1064 nm and 852 nm light beams.

The project will begin with two lasers, operating at the Cs and the GWD wavelengths. They will be combined by sum-frequency generation (SFG) to produce the pump for the OPO. In the NOPO cavity, this pump will be converted back to the desired frequencies. The OPO will act as a two-mode squeezed state source, generating a pair of thermal states sharing EPR entanglement, which can be observed by violating a Duan inequality on the verification stage.

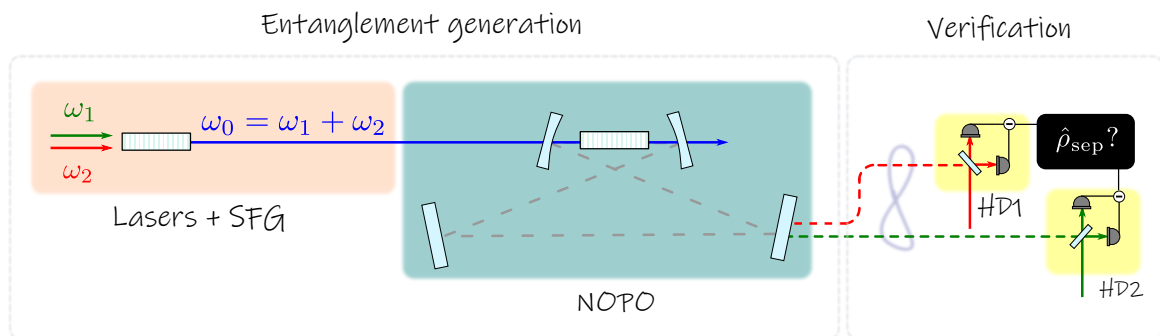


Figure 4.1: Illustration showing the building blocks of the two-color entanglement source.

### 4.1 Laser sources

The proposal [1,28] needs at least two lasers as initial sources: the 1064 nm laser that operates at the GWD interferometer light and the 852 nm laser that allows the light to interact with Cs atoms. Careful characterization of the noise in each laser is fundamental to determine the frequency

limit where entanglement can be measured. In this section, we describe the lasers and analyze their amplitude noise.

### 4.1.1 1064 nm light

The 1064 nm light source is a composition of an Innolight Mephisto Nd:YAG laser (500 NE) with a Nufern fiber amplifier (PSFA-1064-50-10W-2-1) providing up to 10 W of amplified output with narrow linewidth, see Table 4.1 and Fig. 4.2. The Mephisto laser is a narrow linewidth and stable light source [145]. Despite its good stability, the 500 mW of power provided by the Mephisto laser is not enough for our single-pass sum-frequency generation module. The Nufern amplifier can increase the light power without significantly increasing the laser linewidth, and noise [146].

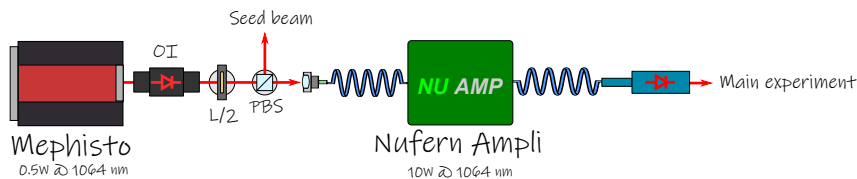


Figure 4.2: The 1064 light setup. Mephisto laser as the master for the fiber amplifier. Part of the Mephisto laser is will also be used for seed and generate the coherent lock field. The output of the Nufern amplifier is primarily used for the SFG stage, OPO lock, and as the local oscillator.

To determine how the amplification changes the noise proprieties of light, we compare the input light with the output light.

Table 4.1: Comparing the Mephisto laser to Mephisto + Nufern amplifier.

	Mephisto	Mephisto + Nufern amplifier
Max. output power	500 mW	10 W
Spatial mode	TEM <sub>00</sub> ( $M^2 < 1.1$ )	same
Linewidth (over 100 ms)	< 1 kHz	< 100 kHz
Intensity noise	< 0.03 % (10 Hz to 2 MHz)	3 % (peak to peak, over 2 h)
Coherence length	> 1 km	same
Frequency stability	< 1 MHz/min	same

To measure the laser amplitude noise, we send light to a balanced detector for shot noise calibration. After having it as a reference, we adjust the input power and block one of the photodiodes to measure the amplitude noise. The results are divided into low-frequency and high-frequency because different spectrum analyzers were used. For the Mephisto laser, results shown in Fig. 4.3, we can identify three regions: the first, a roll of from 0 Hz to 250 Hz; the second a broadband noise  $\approx 10$  dB above the shot noise from 250 Hz to 500 kHz and the third a  $\approx 5$  dB noise above the shot noise from 500 kHz to 2 MHz. In all measurements above, we let the built-in Mephisto amplitude noise eater on.

After comparing the input and output light noise in the amplification stage, we decided that the laser's low-frequency noise characteristics are enough for our project — once the lab environment is kept stable — and if necessary active intensity stabilization schemes can be implemented.

### 4.1.2 852 nm light

Light at 852 nm is provided by a M-Squared Ti:Sapphire laser — SolsTiS PSX-R — pumped by a Lighthouse Photonics Sprout-G10. We investigate the pump effect into the Ti:Sapphire noise

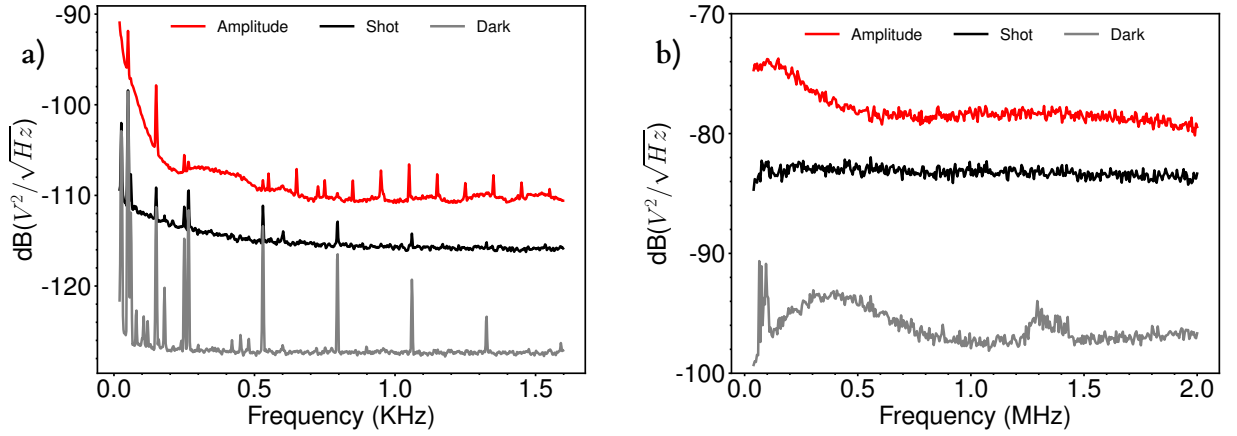


Figure 4.3: Measurements of amplitude noise of the Mephisto laser. a) From 0 Hz to 1.5 kHz, using the Stanford Research Systems SR780 FFT analyser. b) From 50 kHz to 2 MHz, using the Agilent E4405B spectrum analyser. The measured input power is  $\approx 0.2$  mW.

characteristics for low and high frequencies. We found the laser threshold and calibrate the linear dependence of output power with pump power, Fig. 4.4. We have  $\approx 2.3$  W of light at 852 nm at maximum pump power, which is more than enough for our SFG module and the rest of the experiment. The choice of the Ti:Sapphire pump power should consider the laser relaxation oscillation (RO) [127]. The relaxation oscillation frequency  $f_{\text{RO}}$  can be approximated by

$$f_{\text{RO}} \approx \frac{1}{2\pi} \sqrt{\frac{\rho P_{ic}}{\tau_R E_{\text{sat}}}}, \quad (4.1.1)$$

where  $\rho$  is the total intracavity losses in the laser's resonator,  $P_{ic}$  the intracavity power,  $\tau_R$  the resonator round-trip time, and  $E_{\text{sat}}$  the saturation energy of the gain medium. We measured the relaxation oscillation dependence of the Ti:Sapphire laser for different pump powers. Fig. 4.5, shows a broad noise peak shifting to higher frequencies and decreasing in value for growing values of pump power. The plot shows that high-frequency noise ( $> 1$  MHz) can be avoided by running the laser at low pump powers, but for low-frequency noise ( $< 1$  MHz) performance is advantageous to run the laser at its maximum power.

Table 4.2: Sprout and Solstis main parameters.

	Pump (Sprout G-10)	Solstis
Wavelength (nm)	532	775 - 860
Max. output power (W)	10 W	2.3 W
Spatial mode	TEM <sub>00</sub> ( $M^2 < 1.1$ )	TEM <sub>00</sub> ( $M^2 < 1.1$ )
Linewidth (over 100 $\mu\text{s}$ )	-	$< 100$ kHz
Intensity noise (RMS, 10 Hz to 10 MHz)	$< 0.1\%$	$< 0.075\%$

We found that the low-frequency noise of the Sostis laser is determined by a transfer of the pump noise, Fig. 4.5. Over this low-frequency noise, we can observe the broad peak of the relaxation noise and the narrow peaks of diverse origins. If we look at the low-frequency range Fig. 4.6 and 4.6, the amplitude noise spectrum is mainly flat from 200 Hz to 12 kHz except for a peak at 2.6 kHz. For frequencies below 200 Hz, we see several peaks over the noise floor.



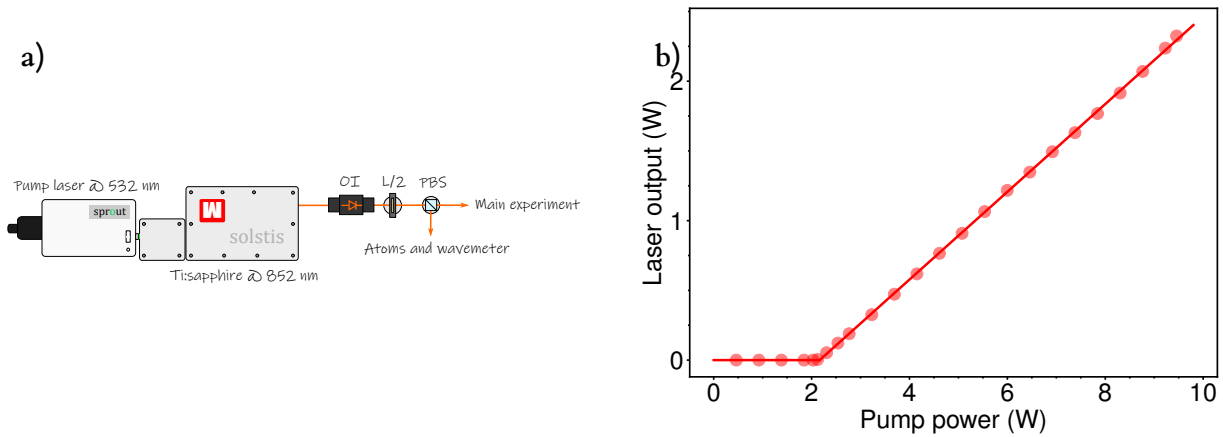


Figure 4.4: a) The 852 light setup. Scheme of the laser arrangement used in our experiment with the Sprout laser and the Solstis laser. The output beam goes into an optical isolator power and is split for the two main parts of the experiment: (i) the SFG process and OPO lock. (ii) Atoms probe and wavemeter to measure the laser wavelength that is used as feedback to tune it. b) Solstis output power as a function of pump power. The fit indicates that the threshold for lasing is 2.18 W and the output power increases at a rate of 0.31 Watts of output per Watt of the pump.

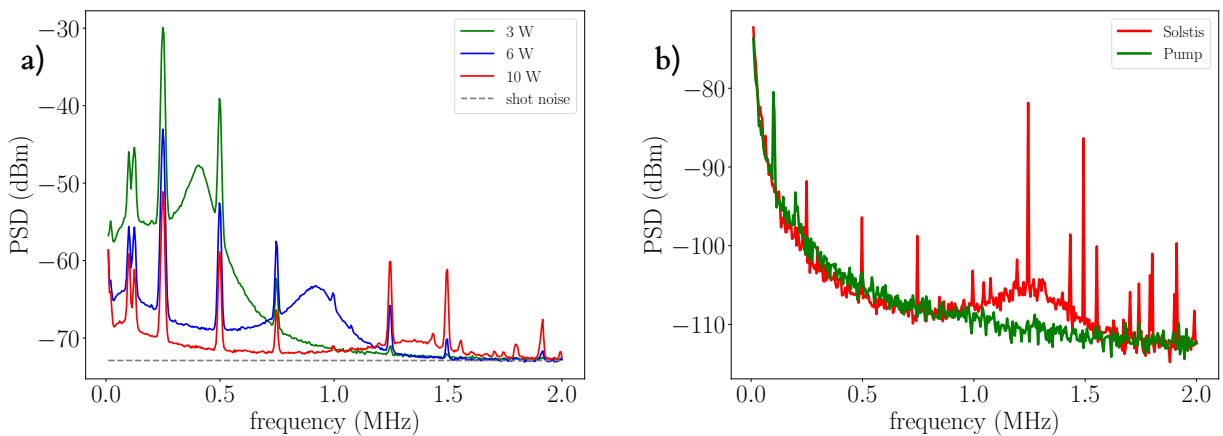


Figure 4.5: a) The typical relaxation oscillation behavior measured by amplitude noise from the laser output power. We can see that the peak frequency increase by increasing the pump power, and the noise is reduced. b) Comparing the amplitude noise of pump and output light from the Sostis laser. This can infer that the low-frequency laser noise is mainly from the pump beam with the relaxation oscillation peak on top.

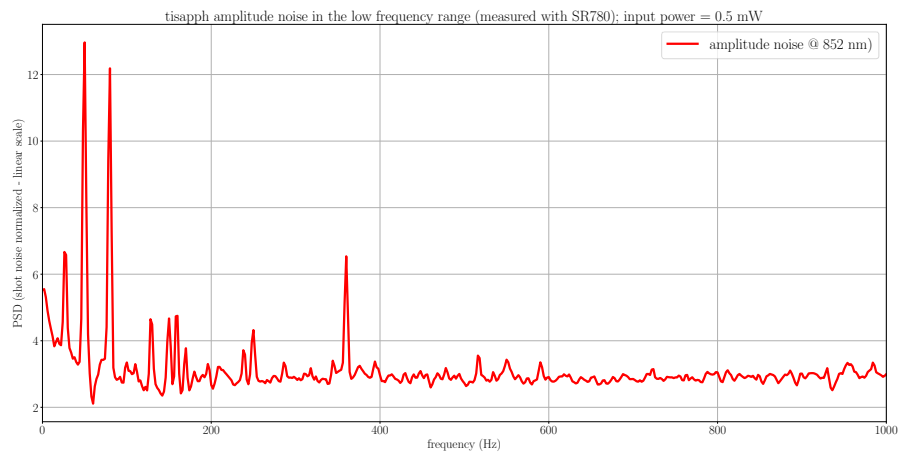


Figure 4.6: Sostis laser amplitude noise normalized to shot noise for frequencies from 0 Hz to 1 kHz (pump power = 10 W).

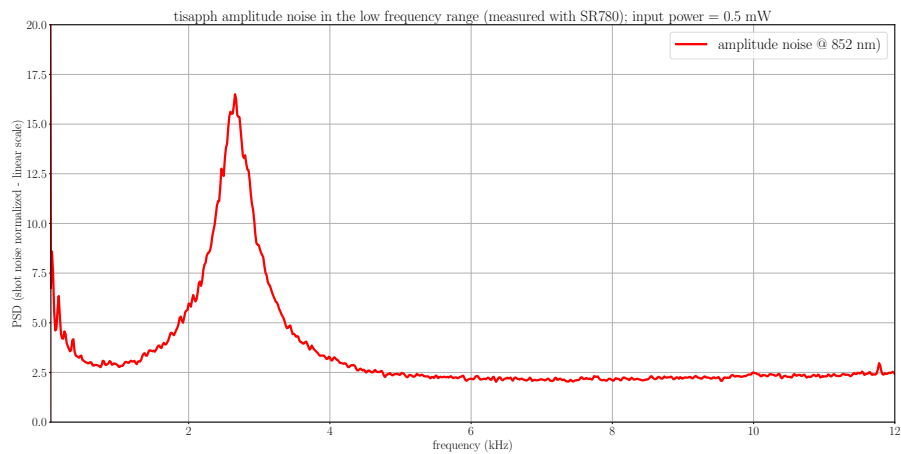


Figure 4.7: Sostis laser amplitude noise normalized to shot noise for frequencies from 0 Hz to 12 kHz (pump power = 10 W).

## 4.2 The nonlinear crystal

The nonlinear crystal we use for the SFG and OPO is a periodically polled potassium-titanyl-phosphate (PPKTP), Fig. 4.8. Optimization of the antireflective (AR) coating for low losses in 1064 nm and 852 nm was only possible with the compromise for the pump wavelength losses at 473 nm. To an overview of the PPKTP main parameters, see Table 4.3. Raicol Crystal Ltd manufactured the crystals for this project. The initial order specified that the phase-matching temperature for the wavelengths of interest should be few degrees above room temperature. Unfortunately, after the crystals arrived, it was found that the phase-matching temperature was much higher, close to 68 °C. While not a problem for this project, a lower phase-matching temperature would help in the SFG and OPO stability. The temperature feedback control works better when the system is closer to the room temperature.

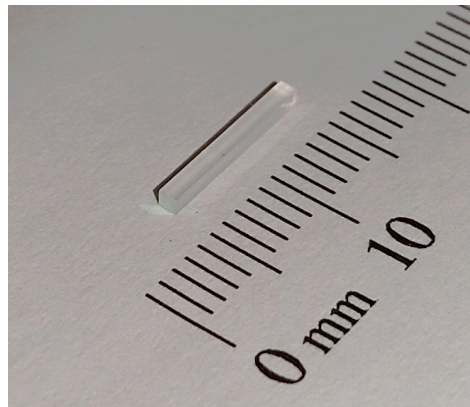


Figure 4.8: Picture of our PPKTP crystal.

Table 4.3: PPKTP main parameters.

PPKTP characteristics	
Dimensions	1 mm X 1 mm X 10 mm
Reflection per face at 1064 nm/852 nm/473 nm	< 0.1 % / < 0.1 % / < 0.5 %
Polarization phase-matching	Type-0
Phase-matching temperature (1064 nm and 852 nm → 473 nm)	68 ° C
Poling period	6.1 μm

To understand the phase-matching tunability ( $\lambda_{\text{signal}}$  and  $\lambda_{\text{idler}} \rightarrow 473$  nm) in function of crystal's temperature we simulate the phase-matching conditions for the polling period of our crystal (6.12 μm), see Fig. 4.9. The matching wavelengths have almost linear dependence with the crystal temperature.

## 4.3 Sum-frequency generation

To pump the OPO, we need light in the frequency given by the sum of twins frequencies, Fig. 4.10. If substantial light power in the same frequency of the twin beam is available, the nonlinear process of sum-frequency generation is the obvious choice to produce such a source. The three-wave mixing guarantees the frequency matching and produces a phase relation between the input beams necessary to measure the entanglement between the twin fields. The SFG process is essentially more

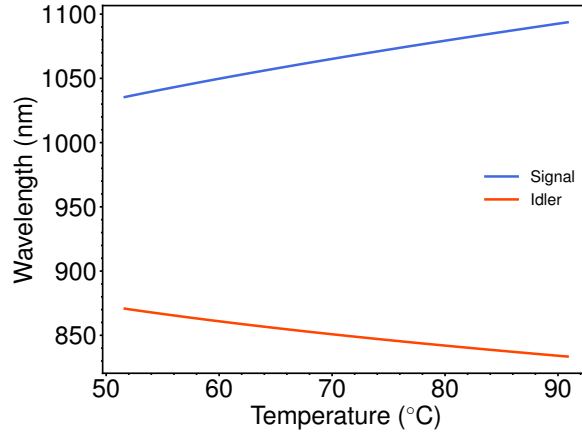


Figure 4.9: Wavelength and temperature to obtain the phase-matching condition for a PPKTP crystal with a polling period of  $6.12 \mu\text{m}$ . The graph shows that the expected phase-matching temperature is around  $68^\circ\text{C}$ . This simulation is done using the SNLO software [147].

complicated than the second-harmonic generation (SHG). Since we rely on two input beams, we must care for different focus and distinct propagation in the nonlinear crystal. The goal is to maximize the generated power while maintaining stability. The straightforward answer is to maximize the overlap with beams propagating in the same direction, but optimally focusing the inputs is a complicated matter. In Appendix C, we describe how to choose the focusing parameters and achieve maximum conversion efficiency properly. We start by introducing the basic theory of single-pass sum-frequency mixing

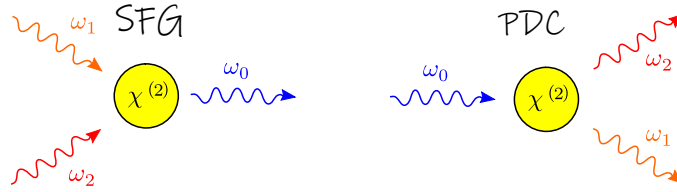


Figure 4.10: (a) Pictorial scheme of the SFG process. Two photons of frequency  $\omega_1$  and  $\omega_2$  can be combined in the nonlinear crystal  $\chi^{(2)}$  medium to generate a photon with frequency  $\omega_0 = \omega_1 + \omega_2$ . (b) The process of parametric down-conversion (PDC) is the core of the entanglement generation.

Consider pump fields with wavelengths  $\lambda_1$  and  $\lambda_2$  and input pump powers  $P_1$  and  $P_2$  assumed, without loss of generality, to obey  $P_1 > P_2$ . By defining  $m = P_2/P_1 < 1$ , the SFG output power at the wavelength  $\lambda_0 = (\lambda_1^{-1} + \lambda_2^{-1})^{-1}$  is given by [148]

$$P_0 = (\lambda_2/\lambda_0)P_2\text{sn}^2 \left\{ \sqrt{(\lambda_0/\lambda_2)\alpha P_1} |m \right\}. \quad (4.3.1)$$

The solution is given in terms of the Jacobian elliptic sine (sn). It highlights the periodic nature of the SFG process with a maximum SFG power given by  $(\lambda_2/\lambda_3)P_2$ . The parameter  $\alpha$  is the nonlinear conversion coefficient often quoted in literature and given in units of  $\text{W}^{-1}$ . Its value depends on the nonlinear crystal specifications and the overlap and focusing of the pumping modes. Expansion of (4.3.1) to first order in  $\alpha$ , leads to the common approximate expression with the SF power being linear with respect to the pump powers

$$P_0 = \alpha P_1 P_2. \quad (4.3.2)$$

This constitutes the undepleted-pump approximation where it is assumed that the pump fields remain undepleted throughout the nonlinear interaction in the crystal. The approximation is often valid due to the low values of nonlinear conversion coefficients. As the SF power increases, energy conservation dictates that the pump powers decrease. The relations give the output pump powers [148]

$$P_{1,\text{out}} \equiv (1 - \Gamma_1)P_1, \quad (4.3.3a)$$

$$P_{2,\text{out}} \equiv (1 - \Gamma_2)P_2, \quad (4.3.3b)$$

where the defined conversion parameters  $\Gamma_1$  and  $\Gamma_2$  are functions of both of the input pump powers. As for the SF power, expansion of the Jacobian elliptic functions to first order in the nonlinear conversion coefficient gives the approximate expressions

$$P_{1,\text{out}} = [1 - (\lambda_0/\lambda_1)\alpha P_2] P_1 \equiv (1 - \Gamma_1)P_1, \quad (4.3.4a)$$

$$P_{2,\text{out}} = [1 - (\lambda_0/\lambda_2)\alpha P_1] P_2 \equiv (1 - \Gamma_2)P_2, \quad (4.3.4b)$$

all the expressions conserve the total initial power  $P_1 + P_2$ . The approximated expression for  $\alpha$  is given by [149]

$$\alpha = \frac{32\pi^2 d_{eff}^2}{\epsilon_0 c n_3^2 \lambda_0 \lambda_1 \lambda_2} P_1 P_2 e^{-\rho l} h. \quad (4.3.5)$$

We turn now to describe the experimental implementation of our SFG module. A simplified illustration of the system is described in Figure 4.11. The crystal is inside a sealed box to avoid airflow and temperature changes. First, we calculate the required waist sizes using the Kleinman-Boyd treatment [150], described in Appendix C. We mix the 1064 nm and 852 nm beams using a dichroic mirror after matching the input beam profiles and polarizations. Then, focus the pumping lasers inside the crystals to a waist size of  $w_{852} \approx 17.5 \mu\text{m}$  and  $w_{1064} \approx 19.7 \mu\text{m}$ .

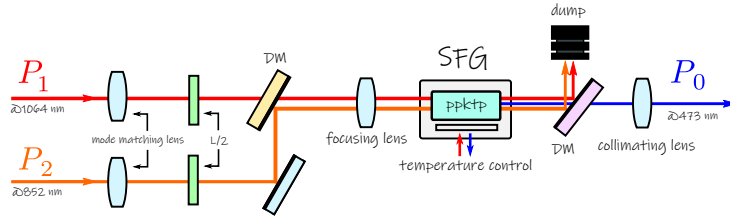


Figure 4.11: Illustration of the SFG setup. L/2 : half-wave plate. DM: dichroic mirror.

The crystal temperature is adjusted, around  $68^\circ\text{C}$ , to increase the SF process. To check the process efficiency as function of crystal temperature, see 4.12. The generated light at 473 nm is separated from the pump beams by a dichroic mirror and collimated. Once the phase-matching temperature is adjusted to maximize we measured the process efficiency in terms of the input powers, Fig. 4.13. The measured conversion efficiency is  $\alpha \approx 5.5\%/W$ .

We have reached stable operation of our SFG module up to 900 mW of light at 473 nm, sending almost all power available in the pump lasers. In everyday operation, we run the SFG at the lowest powers possible to avoid damaging the nonlinear crystal.

## 4.4 OPO cavity design

Many optical parametric oscillator designs are suitable for quantum optics experiments. In respect to mirror cavity geometry, we have the choice of linear cavities, ring cavities, or also part of the whole crystal that can be coated and polished in such a way to form monolithic or semi-monolithic cavities. For resonance conditions, single, double, and triple resonant cavities are also an option. All styles

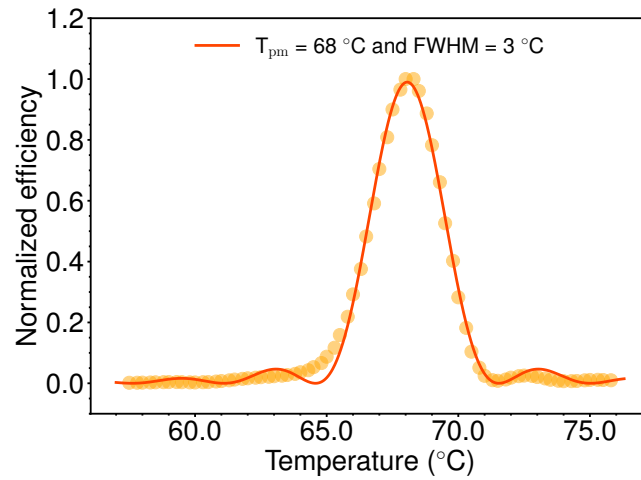


Figure 4.12: SFG phase matching vs temperature and efficiency measurements. (a) normalized conversion efficiency in function of the crystal oven temperature. The input wavelengths are 852.1 nm and 1064 nm. The phase-matching temperature  $T_{\text{pm}}$  is 68 °C, and the temperature bandwidth is approximately 3 °C.

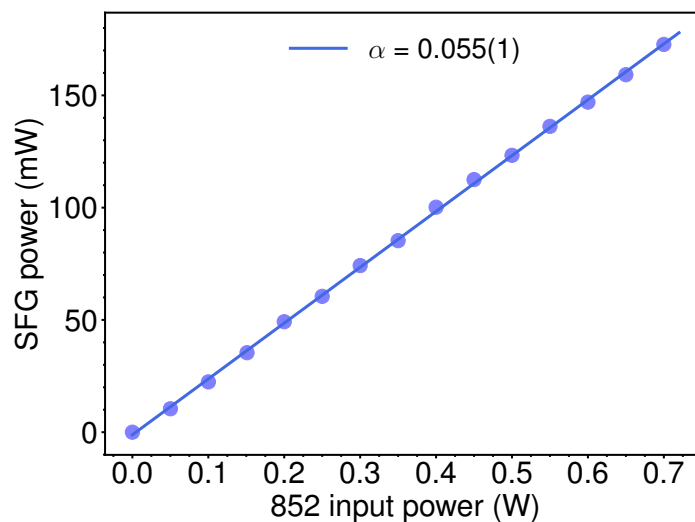


Figure 4.13: The conversion efficiency is 5.5%/W. The 1064 nm powers were fixed at 4.5 W while the 852 power is changed.

have advantages and drawbacks in their designs, and choosing the right one for your application can be tricky. Because we do not have a demand for large bandwidth and need to operate simultaneously with three wavelengths. We choose a configuration with a ring bow-tie cavity with double resonance for 852 nm and 1064 nm.

To calculate the spatial eigenmodes of this cavity, some considerations about the crystal optical properties have to be taken into account. The refractive index depends on the light polarization and wavelength, so that the optical path and Gaussian beam propagation will depend on the input light. The simple bow-tie cavity with a nonlinear crystal can be described in the Fig. 4.14, composed of two plane mirrors ( $M_3, M_4$ ) and two curved mirrors ( $M_1, M_2$ ) with a radius of curvature  $ROC = R$ . In our case  $ROC = 38$  mm. Light impinges on the curved mirrors with an angle  $\theta$ . It is characteristic from curved surface reflection that horizontal and vertical focus will be different. This astigmatism is taken into account by splitting the propagation for tangential and sagittal planes, with  $R_h = R \cos \theta$ ,  $R_v = R / \cos \theta$ . We note that the cavity has one waist located between the plane mirror and another

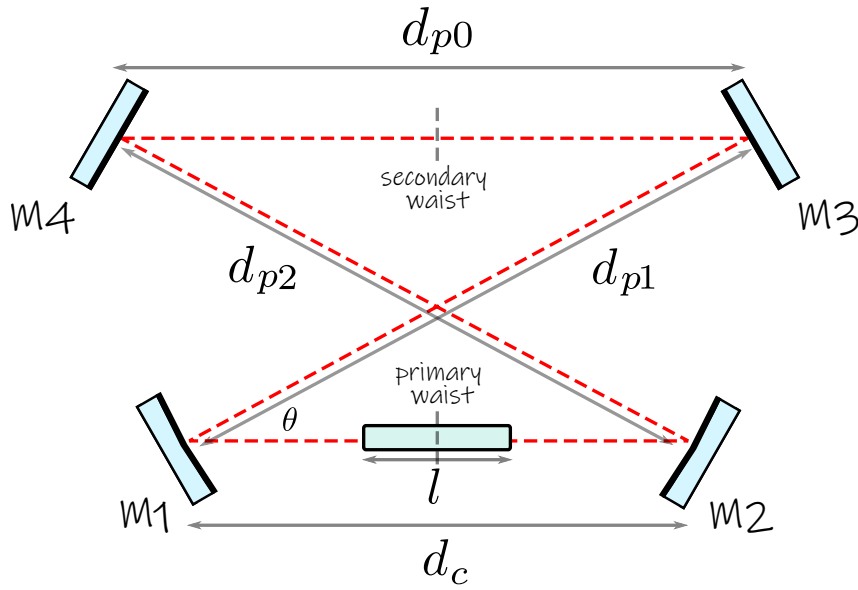


Figure 4.14: Bow-tie cavity scheme. The nonlinear crystal is located between the two curved mirrors for tight focus. The relevant distances between mirrors are labeled.

between the curved mirrors from pure geometrical arguments. The theory of ABCD matrices [127] is useful to calculate all eigenmodes parameters. We can calculate them by choosing a reference plane. The horizontal and vertical propagation ABCD matrices for the primary waist reference plane and  $\lambda_j$  are written as

$$ABCD_{h,j}^{(pri)} = M_f[dp_0/2 + dp_2]M_c[R_h]M_f[(d_c - l)/2]M_n[l, n_j]M_f[(d_c - l)/2]M_c[R_h]M_f[dp_0/2 + dp_1], \quad (4.4.1a)$$

$$ABCD_{v,j}^{(pri)} = M_f[dp_0/2 + dp_2]M_c[R_v]M_f[(d_c - l)/2]M_n[l, n_j]M_f[(d_c - l)/2]M_c[R_v]M_f[dp_0/2 + dp_1]. \quad (4.4.1b)$$

and for the secondary waist reference plane

$$ABCD_{h,j}^{(sec)} = M_n[l/2, n_j]M_f[(d_c - l)/2]M_c[R_h]M_f[dp_0 + dp_1 + dp_2]M_c[R_h]M_f[(d_c - l)/2]M_n[l/2, n_j], \quad (4.4.2a)$$

$$ABCD_{v,j}^{(sec)} = M_n[l/2, n_j]M_f[(d_c - l)/2]M_c[R_v]M_f[dp_0 + dp_1 + dp_2]M_c[R_v]M_f[(d_c - l)/2]M_n[l/2, n_j]. \quad (4.4.2b)$$

The beam size in a given reference plane can be calculated by

$$w_{\text{ref},j}^2 = |B| \frac{\lambda_j}{\pi} \sqrt{\frac{1}{1 - \mathfrak{M}^2}}, \quad (4.4.3)$$

where  $\mathfrak{M} = (A + B)/2$ . One relevant requirement for the waist size is the waist size inside the crystal should be compatible with the Kleinman-Boyd calculation [150], Appendix C. This optimizes the nonlinear interaction and reduces the necessary pump power to achieve a certain gain value. In 4.15 and 4.16 the cavity waist sizes are analyzed.

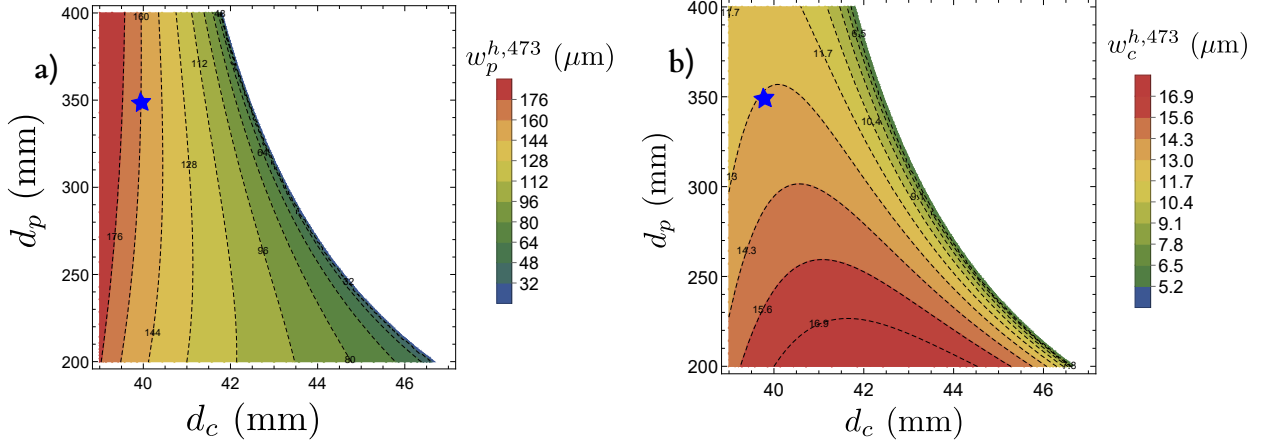


Figure 4.15: Plot of waist size between the curved mirror (a) and between the plane mirror (b) for different  $d_c$  and  $d_p$ . (a) The goal is to choose a length for  $d_p$  such that it is possible to achieve the optimum waist size inside the nonlinear crystal by varying  $d_c$ . (b) Shows the change in the waist size between the plane mirrors. ROC = 38mm.

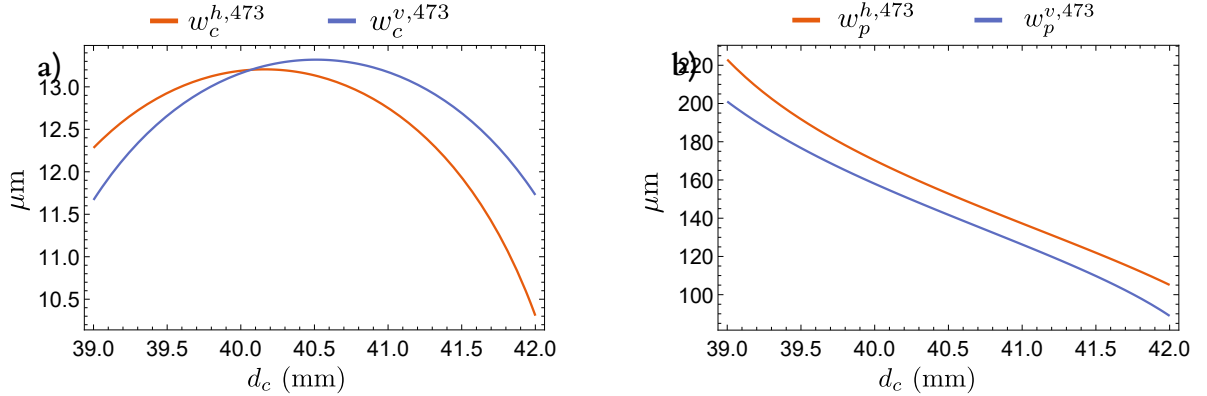


Figure 4.16: Plot of horizontal and vertical waist sizes for a fixed distance  $d_p = 347$  mm. (a) astigmatism can be canceled by choosing a convenient distance between the curved mirrors marked with. (b) For the secondary waist, astigmatism can not be canceled, and the output mode is always astigmatic. This reduces the overlap with local oscillators if no mode shaping is introduced after the OPO. The advantage of choosing this as the output mode is to easily get rid of the pump. Also, the divergence angle is small compared to the primary waist. ROC = 38 mm.

The angle  $\theta$  should be made as small as possible given the cavity geometry restriction. The limiting factor is the diameter of the curved mirrors. With a thin crystal and curved mirror with a small diameter, we can reduce astigmatism. Once all parameters are chosen, we proceed to analyze the high-order mode distribution. For a stable resonator, one spatial eigenmode  $\alpha_{mn}$  acquires a Gouy



phase after one cavity round trip given by

$$\exp[\mp i(n + m + 1)\varphi], \quad (4.4.4)$$

where  $\cos \varphi = \mathfrak{M}$ . This introduces an effective frequency shift in resonance of a mode  $(m,n)$  with respect to the fundamental mode  $(0,0)$ , given by

$$\Delta f_{mn} = \text{FSR} \frac{(m+n)}{2\pi} \text{sign}(B) \arccos \mathfrak{M}. \quad (4.4.5)$$

The exact high-order mode (HOM) distribution can be estimated once the cavity is built and the Gouy phase measured. If high-order modes lay near the FSR, they can leak together with the fundamental mode and degrade the mode's spatial quality, reducing the overlap with the local oscillator. In Fig. 4.17, we show an example of the cavity HOM distribution for the non astigmatic configuration between the curved mirrors. Unfortunately, this is a high contamination configuration. To avoid the HOM contamination, we reduce the distance  $d_c$  by 0.5 mm and obtain an almost free HOM contamination configuration. From our experience, this was the difference between 97% and 99.5% in homodyne visibility.

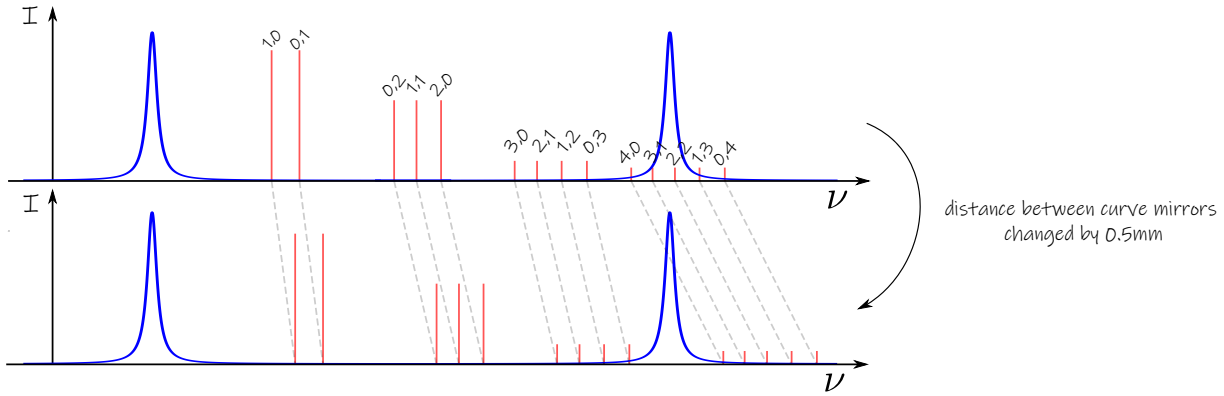


Figure 4.17: High order mode spacing for (a) initial configuration (b) adjusted cavity size. (a) The fourth-order modes are initially overlapping with the cavity resonance. (b) After a 0.5 mm cavity reduction.

## 4.5 OPO assembly

We decided to build the OPO in an aluminum block box to minimize mechanical and thermal perturbations, Fig. 4.18. The block was CNC-milled to accommodate the mirror mounts and crystal stage positioner. Optical access is possible via apertures in the block structure. To guarantee minimum angle of incidence and reduce the cavity astigmatism, the line joining the center of the curved mirrors M1–M2 should be parallel and as close as possible to the line joining the center of the plane mirrors M3–M4. To achieve optimum angle, we used a 7 mm diameter mirror for M1 and M1 attached to the adaptor and attached<sup>1</sup> to the mirror mounts. The M3 and M4 mirrors are 1/2" in diameter.

Feedthrough holes provide wires access for signals to control the crystal temperature and cavity size. The parts used to build the mechanical and electronic parts used to build the OPO are listed in Table 4.4. The crystal oven temperature is measured via a thermistor. A dual-stage thermoelectric cooler (TEC) is responsible to cool or heat the oven following a feedback loop given by a commercial temperature controller. The cavity size is controlled with a piezo transducer mounted in the brass

<sup>1</sup>UV glue was used to bind the mirrors to the adaptors.

holder (M4) that is used to scan and lock the cavity resonance. After assembly, the cavity finesse was measure to be  $\mathcal{F} \approx 52$  for both wavelengths, giving a cavity bandwidth of  $\approx 15$  MHz.

Table 4.4: Parts used in the OPO construction

Equipment	Manufacturer	Model
Mirror mounts	Thorlabs	POLARIS-K05C4
Alignment stage	Newport	9082-V-M
TEC	Thorlabs	TECD2
Temperature controller	Thorlabs	TED200C
NCT 100 k $\Omega$ thermistor	Murata	NXFT15WF104FA2B100
Piezo	Piezomechanik	HPSt 150/14-10/12

#### 4.5.1 Intracavity losses

As described in chapter 3, the intracavity spurious losses limit the amount of output entanglement. The losses can be estimated by complete optical characterization of each cavity component or by a finesse measurement. However, those methods are usually not practical or provide poor estimates for small spurious losses. To a better escape efficiency characterization, it is necessary to find a method that differentiates the total losses from the spurious ones and can be performed without disturbing the experimental setup. We know that escape efficiency  $\eta_j$ , for the wavelength  $\lambda_j$  is determined by

$$\eta_j = \frac{T_j}{T_j + \mathcal{L}_j}, \quad (4.5.1)$$

$T_j$  is the in/out coupler mirror transmission, and  $\mathcal{L}_j$  is the intracavity spurious loss for  $\lambda_j$ . In the situation where the cavity total loss is dominated by  $T_j$ , we can write the rate between the input power  $P_j^{\text{in}}$  and output power  $P_j^{\text{re}}$  reflected by the cavity when light is injected from the in/out mirror as

$$\frac{P_j^{\text{re}}}{P_j^{\text{in}}} = \left( \frac{T_j - \mathcal{L}_j}{T_j + \mathcal{L}_j} \right)^2, \quad (4.5.2)$$

for a probe that is perfectly matched with the cavity mode. By measuring the dip in reflection and knowing  $T_j$ , we can estimate  $\mathcal{L}_j$ . In Fig. 4.19, we can see the reflected dips for 1064 nm and 852 nm. In the experiment, sometimes, it is not easy to obtain cavity coupling close to 100%. As is the case in Fig. 4.19. To take the effect of mode matching, we need to compensate the contribution from high order modes. By subtracting the contribution of the HOM dips, HOM, can we correct the estimate. This is done by

$$\frac{P_j^{\text{re}} - \sum \text{HOM}}{P_j^{\text{in}} - \sum \text{HOM}} = \frac{(T_j - \mathcal{L}_j)^2 - \sum \text{HOM}}{(T_j + \mathcal{L}_j)^2 - \sum \text{HOM}}, \quad (4.5.3)$$

So that we write  $\eta_j$  as

$$\eta_j = \frac{1}{2} \left( 1 + \sqrt{\frac{P_j^{\text{re}} - \sum \text{HOM}}{P_j^{\text{in}} - \sum \text{HOM}}} \right). \quad (4.5.4)$$

and the total OPO escape efficiency is given by  $\eta_{\text{OPO}} = \sqrt{\eta_1 \eta_2}$  [133]. In our OPO cavity, the spurious losses are estimated to be  $\mathcal{L}_{1064} = 0.15(2)$  % and  $\mathcal{L}_{852} = 0.21(2)$  %. This is compatible with the crystal AR coating and absorption. The asymmetry is mainly due to the crystal AR coating. This leads to an overall OPO escape efficiency of  $\eta_{\text{OPO}} = 0.98(3)$  Without the crystal, we measured the loss to be  $\lesssim 0.03(1)$  % for the two wavelengths.

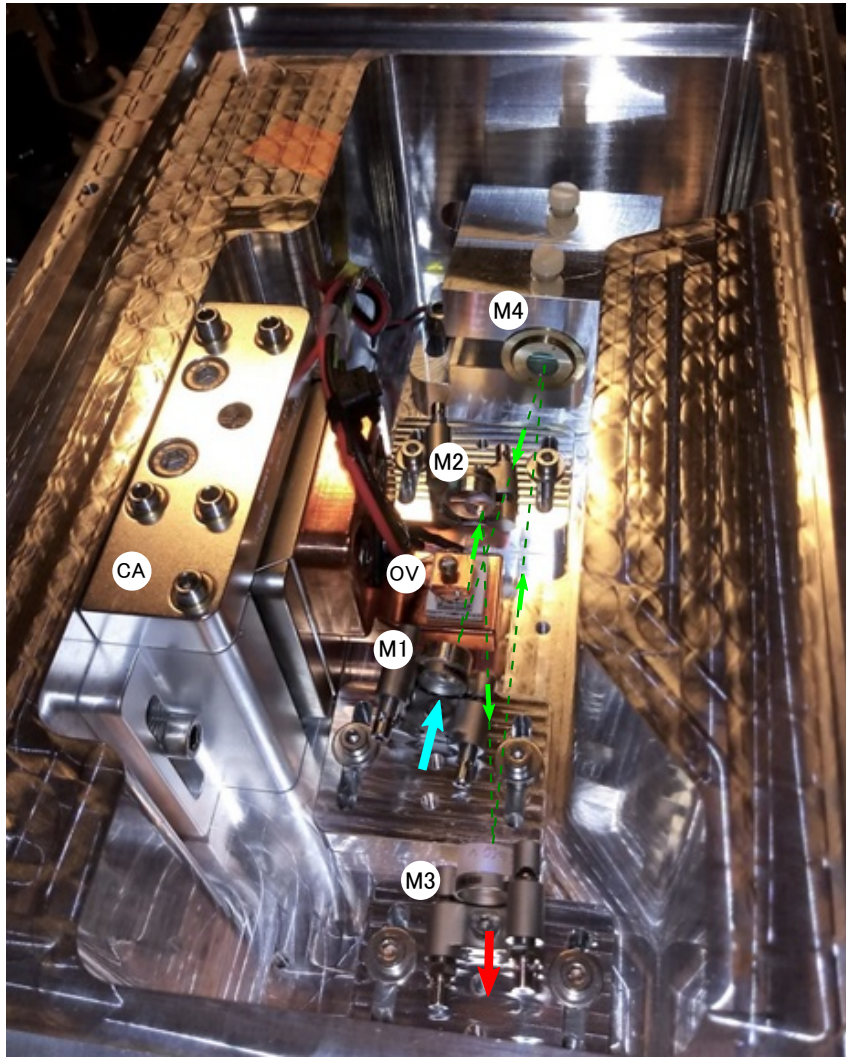


Figure 4.18: Picture of the assembled optical parametric oscillator. M1: curved mirror where the pump light is injected, HR for 1064/852 nm, AR for 473 nm. M2: curved mirror that transmits the pump light out of the cavity, HR for 1064/852 nm, AR for 473 nm. M3: plane output mirror,  $T \approx 12\%$  for 1064/852 nm. M4: plane mirror, HR for 1064/852 nm, attached to a PZT to control the cavity size. OV: crystal oven composed of a copper holder, TEC, and thermistor. CA: crystal alignment stage. Blue arrow: pump injection direction. Red arrow: OPO output. Dark-green dotted line: cavity propagation paths. Light-green arrows: the direction of signal and idler propagation.

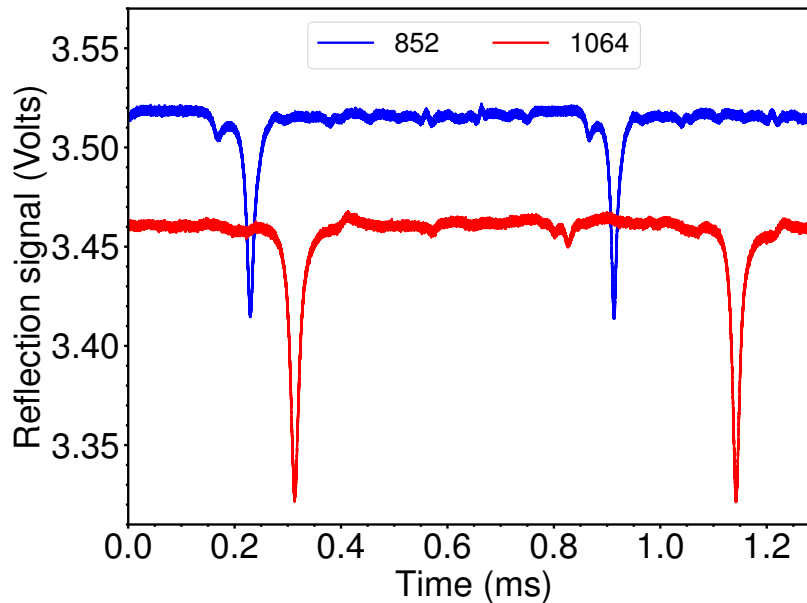


Figure 4.19: Measurement of reflection dip for spurious loss estimate. The cavity is scanned, and the main dip corresponds to the fundamental mode. The contribution of the HOM to the off-resonance value must be removed to improve the estimate.

## 4.6 Two-color setup

A picture of the built experimental setup is shown in 4.20, and a detailed scheme is presented in Fig. 4.21. Our 1064 nm and 852 nm lasers are split and sent to the SFG stage, to the local oscillator stage, and to lock the OPO cavity system. The 1064 light has an extra path used as seed for the OPO.

### 4.6.1 Cavity locks

To maintain the OPO at double resonance, phase-modulated counterpropagating beams are injected through the HR mirror (M4), Fig. 4.18. The lock beams are detected at the cavity transmission, Fig. 4.21, and the signal is demodulated to generate a Pound-Drever-Hall error signal [151, 152]. The lock has two steps; first, we lock the cavity length relative to the 1064 nm laser — for that, feedback is sent to a piezoelectric transducer (PZT) attached to one of the OPO mirrors (M4). Then we lock the 852 nm laser to the cavity by applying slow feedback to the PZT inside the Ti:Sapphire laser. In the end, the stability of the system is determined by the frequency/phase fluctuations of our 1064 nm laser and undesired mechanical and thermal fluctuations. All feedback loops are controlled using FPGA boards (Redpitaya STEMLAB, 125-14), and the PyRPL package [153].

To generate the LOs, a fraction of the lasers' output is transmitted through mode-cleaner cavities with the bandwidth  $\approx 1$  MHz, shown in Fig. 4.21. The cavities consist of two plane mirrors and one curved mirror in a triangular configuration built in a monolithic aluminum block. They are used to perform spatial mode filtering as well as to eliminate beam pointing jitter. An example of the lock performance can be seen in Fig. 4.23.

### 4.6.2 Parametric gain

We start by generating about 250 mW of SFG light. The pump beam is mode matched to the OPO cavity by calculating the beam's position and value inside the crystal. To check the parametric gain, we pump the OPO cavity and inject a 1064 nm seed, Fig. 4.21 (gain only beam). The cavity is



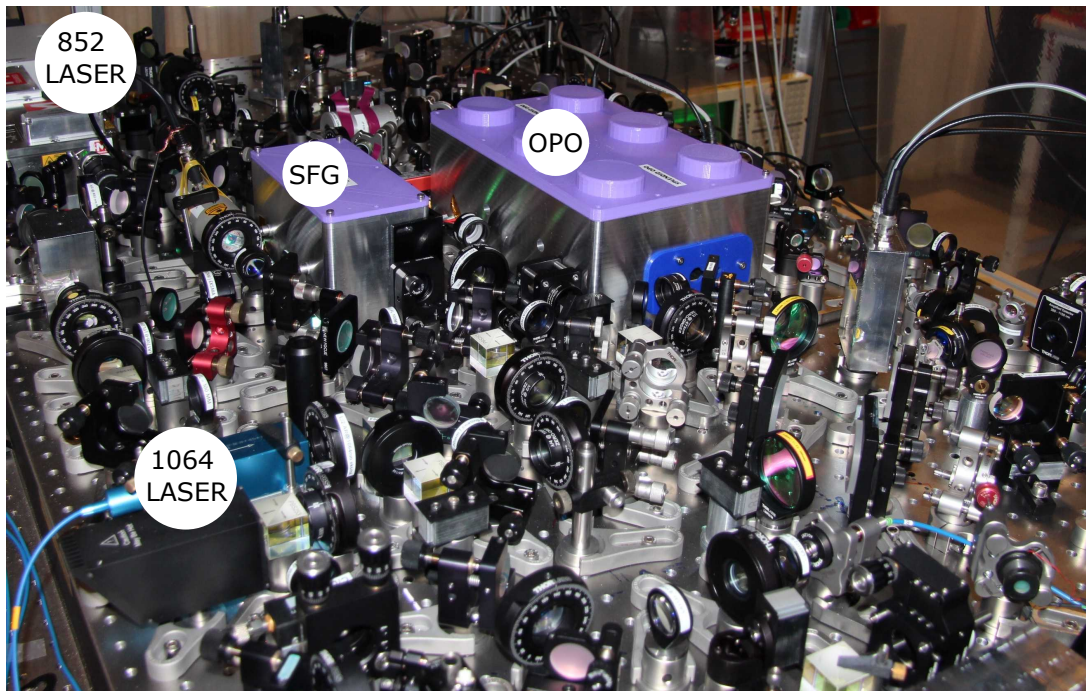


Figure 4.20: Picture of the experimental setup for two-color EPR-state.

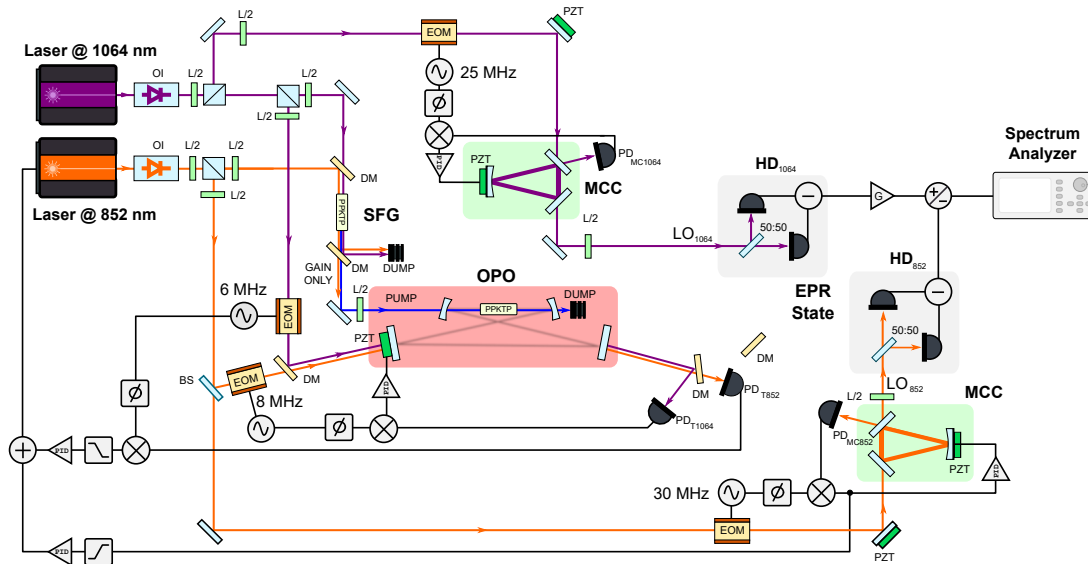


Figure 4.21: Scheme of the experimental setup. The 852 nm and 1064 nm (after amplification) lasers produce the blue light used to pump the OPO through the sum-frequency generation. The two colors of the OPO output are separated with a dichroic mirror and sent to the homodyne detectors. The local oscillators are produced by MMC and overlapped with the corresponding output beams in the HD scheme. The photocurrents are combined and sent to a Spectrum analyzer for noise analysis. L/2 : half-wave plate. DM: dichroic mirror. PID: Proportional-Integral-Differential loop. OI: optical isolator. PD: photodetector. EOM: Electro-optical Modulator.

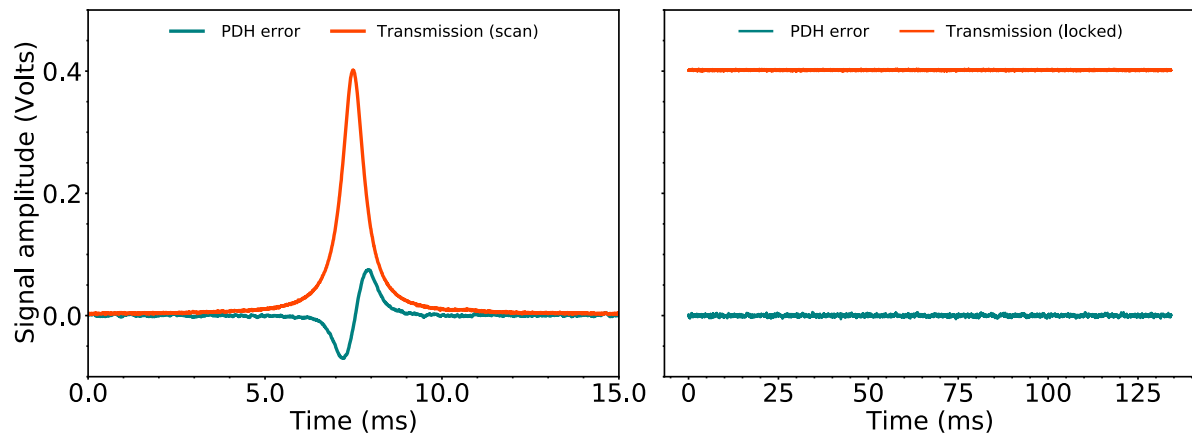


Figure 4.22: Example of cavity lock for one of the OPO wavelengths. This is the scan (left) and lock regime (right) for the 852 nm OPO lock beam, Fig 4.21.

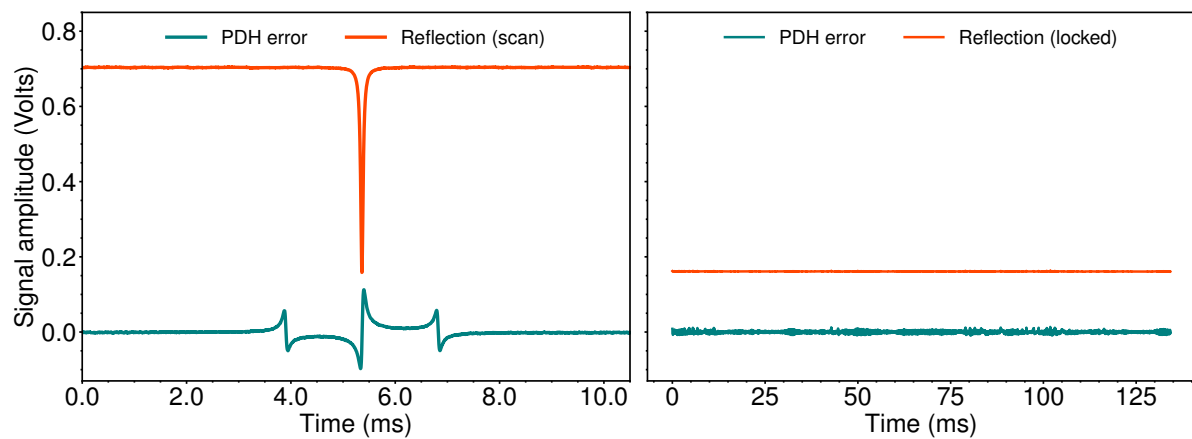


Figure 4.23: Example of cavity lock for one of the mode cleaner cavities (MCC). This is the scan (left) and lock regime (right) for the 1064 nm LO MCC, Fig 4.21.

locked to resonance with 1064 nm light, and the 852 nm laser is scanned. We tune the PPKTP crystal temperature for maximum gain. A measurement of OPO parametric gain is presented in 4.24. The fit of (3.6.24) gives an estimated oscillation threshold of  $\approx 320$  mW. The SFG power of blue light is more than necessary for the initial characterization of entanglement, giving a maximum pump parameter of  $\sigma_{\max} \approx 0.7$ . To achieve a stable parametric gain, the 852 nm laser frequency is locked to the OPO cavity. This guarantees that the laser is going to follow the slow 1064 nm frequency drifts. Only parking the laser on double resonance is not enough to guarantee long-term operation. The active laser frequency change can introduce phase drifts that can affect the measurement stage by changing the homodyne phase.

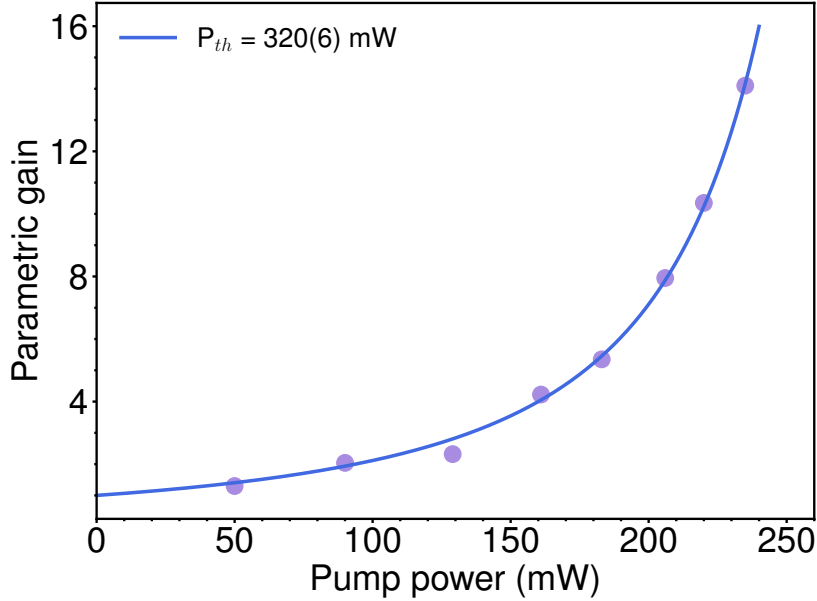


Figure 4.24: Measurement of the parametric gain for different pump powers. The fit of (3.6.24), gives and estimated oscillation threshold of  $\approx 320$  mW.

### 4.6.3 Homodyne detection and estimated losses

The entangled beams leak from the output coupler mirror M3 and are separated by a low-loss dichroic mirror, reflecting 852 nm and transmitting 1064 nm. Low-loss mirrors are used to steer the entangled beams to the homodyne stages, Fig. 4.21. No lenses or waveplates are used from the OPO's output to the homodyne to avoid optical losses. Each beam is overlapped with its corresponding local oscillator in a 50/50 beam splitter. The achieved fringe visibilities are  $\mathcal{V}_{1064} \gtrsim 98\%$  and  $\mathcal{V}_{852} \gtrsim 97\%$ . A visibility less than 100% is equivalent to optical losses, and the efficiency is given by  $\eta_{MM} = \mathcal{V}^2$ . An estimate of the overall losses in the experiment is presented in Table 4.5 (the values of  $\eta_{MM}$  correspond to the specific entanglement measurements in this chapter).

The photodiodes used for 1064 nm are Fermionics InGaAs PIN FND-500-1064 with estimated quantum efficiency of  $\eta_{det,1064} = 98\%$ . For 852 we use Hamamatsu Si PIN S5971 with estimated quantum efficiency  $\eta_{det,852} = 97\%$ . All diodes are operated without protection windows to avoid losses, and they both have  $500 \mu\text{m}$  diameter of area. We choose to match the shot level of each homodyne stage for the initial measurement by changing the local oscillator powers. This is a simple way to adjust the gains of the measured quadrature before their combination. Another important factor is the Common Mode Rejection Ratio (CMRR) of the balanced detection. We operate the homodyne detectors with  $\text{CMRR}_{1064} = \text{CMRR}_{852} \approx 40$  dB.

Table 4.5: Estimated efficiencies in the experimental setup.

Efficiency	1064 nm	852 nm
$\eta_\lambda$ (escape)	0.986	0.983
$\eta_{\text{prop}}$ (output to HD)	0.995	0.994
$\eta_{\text{MM}}$ (overlap with LO)	0.96	0.93
$\eta_{\text{det}}$ (photodiodes)	0.98	0.97

## 4.7 Entanglement measurements

The quantum correlations can be seen in a given set of quadrature combinations, as described in 3.6. The LO power is changed according to match the signal amplitude, but the phase combination is still not adjusted. In each LO path, a piezo actuator can use a mirror to variate the local oscillator phase, Fig. 4.21. As a preliminary measurement we let the 852 nm local oscillator phase free running and scanning the 1064 local oscillator phase. We obtain the sum and the subtraction of the homodyne photocurrents by mixing the signals with power splitters. The results for a detection frequency of 350 kHz are shown in Fig. 4.25 and 4.26. From the obtained data the sum of variances for the Duan inequality is estimated to be

$$\text{Var} \left[ \frac{\hat{X}_{1064} - \hat{X}_{852}}{\sqrt{2}} \right] + \text{Var} \left[ \frac{\hat{Y}_{1064} + \hat{Y}_{852}}{\sqrt{2}} \right] \approx 0.32(5) < 2. \quad (4.7.1)$$

To the best of our knowledge, the highest quantum correlation was ever measured for such long separated wavelengths. By the level of antiqeezing ( $\approx 15$  dB) and squeezing ( $\approx -8$ dB) the total quantum efficiency can be calculated giving a value of  $\eta_{\text{total}} \approx 85\%$ , which is close to the estimated total efficiency taking in account each source of loss in the system, we can calculate it by  $\eta_{\text{total}} = \eta_{\text{OPO}}\eta_{\text{optics}}\eta_\nu\eta_{\text{det}} \approx 86\%$ .

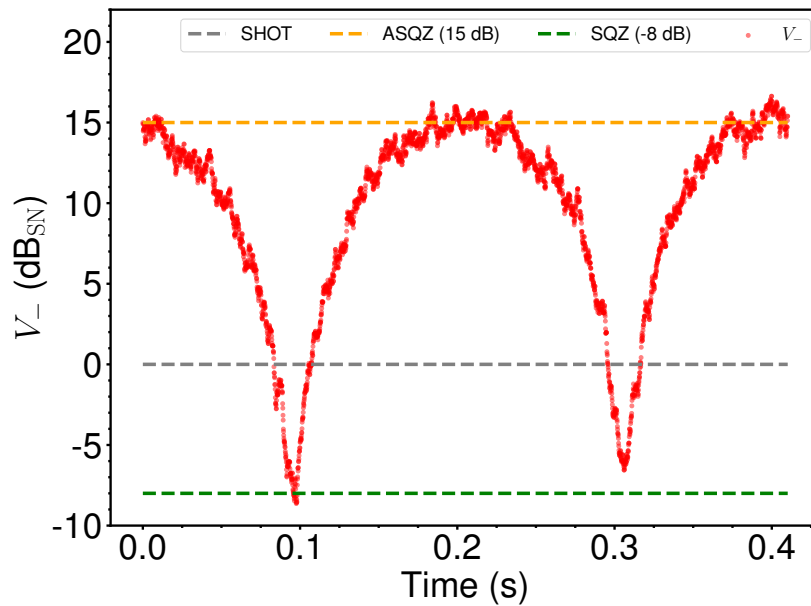


Figure 4.25: Noise measurement of the difference of homodyne photocurrents. During the measurement, one homodyne angle was free running, and the other was slowly scanned with a ramp. The numbers are normalized to shot noise unities and corrected by dark noise. The RBW 10 kHz is and VBW is 100 Hz.



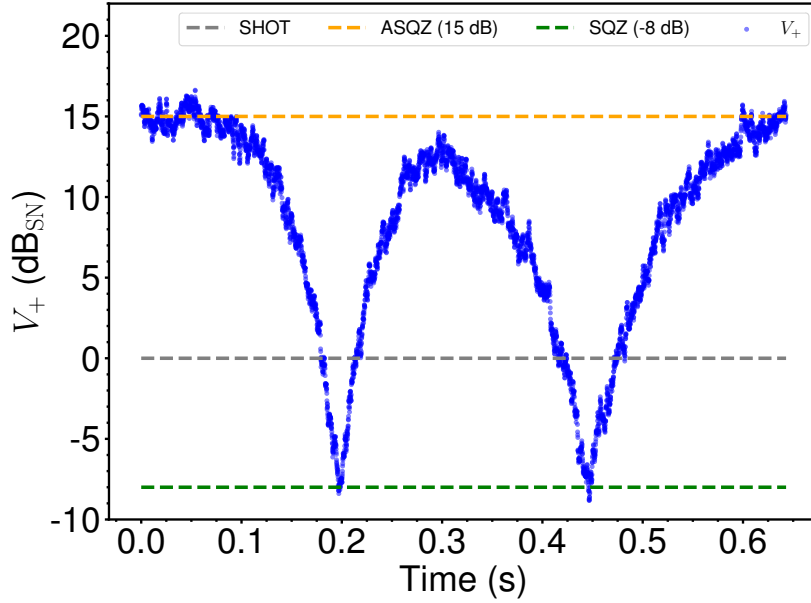


Figure 4.26: Noise measurement of the sum of homodyne photocurrents. During the measurement, one homodyne angle was free running, and the other was slowly scanned with a ramp. The numbers are normalized to shot noise unities and corrected by dark noise. The RBW 10 kHz is and VBW is 100 Hz.

After we optimize the quadrature measurement for the above set of parameters, we measure the correlations for different pump powers. The measurements for different pump powers are shown in 4.27. By fitting (3.6.18) to the data, we estimate  $P_{th} \approx 316$  mW,  $\eta_{total} \approx 0.86$ , and  $\delta\theta \approx 50$  mrad. In these particular measurements, the phase noise contribution is clear. We reach the point where the degree of entanglement is reduced by increasing the pump power. This happens due to antisqueezing being projected into squeezing [135]. We attribute the difference in phase noise to the lock stability and phase scan drifts due free run phase in one HDs. If noise present, we would be able to measure the maximum degree of entanglement generated and be limited only by losses. There are ways to mitigate the phase noise to a certain degree, but it will always be a limiting factor in measuring the high degree of quantum correlations.

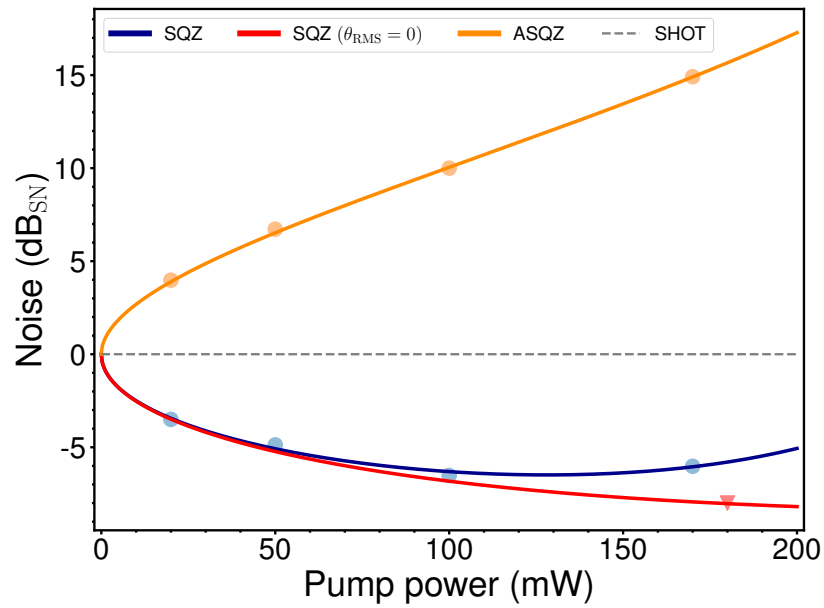


Figure 4.27: Noise in the subtraction of photocurrents normalized to the shot noise level for different pump powers. We fit the model (3.6.18) to the data (solid orange and blue trace). The points for SQZ and ASQZ correspond to a different experimental run from the data in Fig. 4.26 and 4.25. The red trace corresponds to the same parameters estimated from the model but with  $\theta_{\text{RMS}} = 0$ , the red triangle is the squeezing value obtained in the previous experimental run.  $\Omega = 350$  kHz, the RBW 10 kHz is and VBW is 100 Hz.



## Part III

# Three-color entanglement



## Chapter 5

# Towards three-color entanglement

Another relevant system for quantum communications, quantum information, and quantum measurements is the optical parametric oscillator in the above threshold operation. We will explore in this chapter the development of such a unit aiming at the quantum coupling of Rubidium atoms and systems operating at the C-band in telecommunications.

### 5.1 The pump laser

In the laboratory at the University of São Paulo, there were two commercial lasers at 532 nm: the LWE-142 fabricated by Lightwave electronics. The other is the Diablo laser fabricated by Innolight. Both lasers work by similar principles, a diode laser at 808 nm pumps an Nd:YAG crystal generating light at 1064 nm, and then the frequency is doubled using a nonlinear crystal through second harmonic generation<sup>1</sup> giving 532 nm light as output. They present similar spectral characteristics but differ by output power and control options.

Table 5.1: LWE-142 and Diablo main parameters.

	Lightwave	Diablo
Output power - (mW)	200	500
Linewidth (kHz/millisecond)	< 10	1
Amplitude noise (RMS, 10 Hz to 2 MHz)	< 0.2%	< 0.06
Coherence length (km):	> 1	> 1
Frequency stability, jitter (kHz/second):	< 300	30

We have used only the LWE-142 in this project so far. For an adequate stabilization of internal parameters, the LWE-142 requires a good system for temperature dissipation. All controls of parameters are made through a computer connection using an RS-232 serial port. When we first attempted to increase the laser output power, it demonstrated an unstable operation, shutting down after 2 minutes of stable output or simply not locking the stability of the LWE-142. We installed a cooling system to help the heat dissipation at the laser surface. A water block with circulating water at 20 °C provided by a chiller significantly improved the laser stability. After the dissipation problem was solved, another effect was limiting the maximum (nominal) output of 200 mW. A spurious higher-order spatial mode was affecting the stability. This problem involves internal optics, and we were unable to fix it. Given the limiting factors, the maximum output power of pure TEM<sub>00</sub> mode is 110 mW.

<sup>1</sup>LWE-142 and Diablo are examples of DPSS (Diode Pumped Solid State) lasers.

### 5.1.1 The ordered PPKTP

To obtain the desired wavelengths, we choose to buy a crystal with quasi-phase matching, a PPKTP (Periodically-Poled Potassium Titanyl Phosphate<sup>2</sup>) with type-I phase matching. It can be tailor-made for all nonlinear applications within the transparency range of KTP, without the phase-matching limitations of birefringent matching used in regular KTP interactions. Its effective nonlinear coefficient is about three times larger than that of bulk KTP. PPKTP crystals are widely used in high efficient nonlinear optical effects, and many groups have demonstrated high levels of squeezing using optical parametric oscillator based on PPKTP crystals.

We ordered a PPKTP crystal from Raicol Crystals Ltd. It has a length of 15 mm with an aperture size of 2x1 mm<sup>2</sup>. For low phonon noise contribution, we specified that the phase matching for 532 nm  $\rightarrow$  795 nm + 1608 nm happens at the temperature of  $-20^\circ\text{C}$ . The crystal with specific phase matching temperature, a high-quality surface antireflection coating for 532 nm, 795 nm, and 1608 nm was requested. The coating treatment quality is essential to the entanglement generation because it is the factor that determines the intracavity losses and, therefore, the maximum entanglement violation we can achieve.

Raicol Crystals specializes in the manufacture of nonlinear optical crystals and electro-optic devices and has more than 20 years of experience developing and manufacturing PPKTP for various applications. Nevertheless, we will see that this expertise was not enough to achieve our simple needs.

To compare the received crystals with our request, we ran simulations using SNLO<sup>3</sup> (Select Non-Linear Optics) software. It can calculate the periodic polling necessary to achieve a given phase matching in a specific temperature by choosing the nonlinear crystal. The data for generated wavelengths in function of the periodic polling  $\Lambda$  for the temperature of phase matching we wanted is shown in Fig. 5.1. We can see that variations of the order of  $0.1\ \mu\text{m}$  is sufficient to induce significant changes in the output wavelengths. For crystal temperature of  $-20^\circ\text{C}$ , the desired wavelengths (blue and red dots in Fig. 5.1) are achieved for  $\Lambda \approx 10.12\ \mu\text{m}$ .

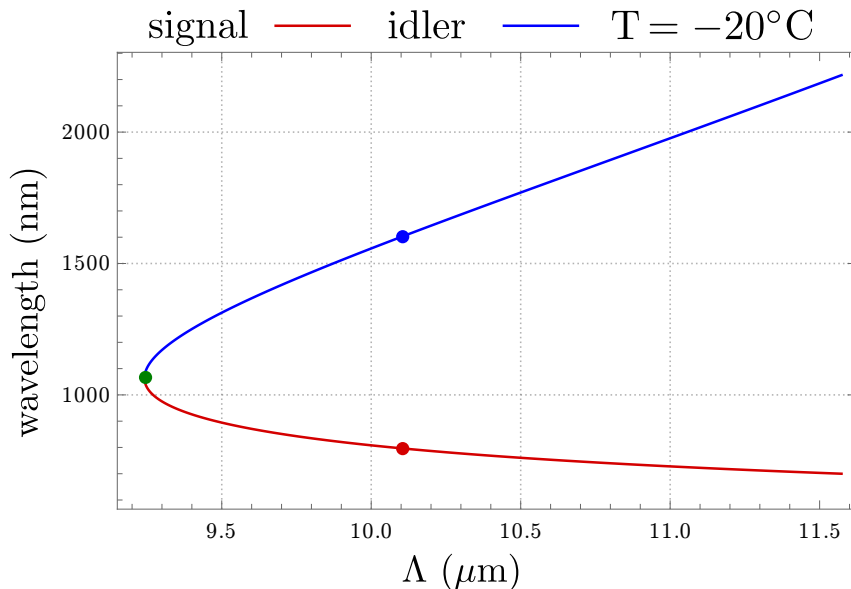


Figure 5.1: SNLO simulation of output wavelengths for a pump wavelength of 532 nm in function of the polling period. The temperature was fixed at  $-20^\circ\text{C}$ .

Once we defined the period, it is interesting to study the tunability of the phase matching with

<sup>2</sup>KTiOPO<sub>4</sub>

<sup>3</sup>SNLO is free software developed by Dr. Arlee Smith. It has several functions to assist in selecting a nonlinear crystal and modeling its performance.

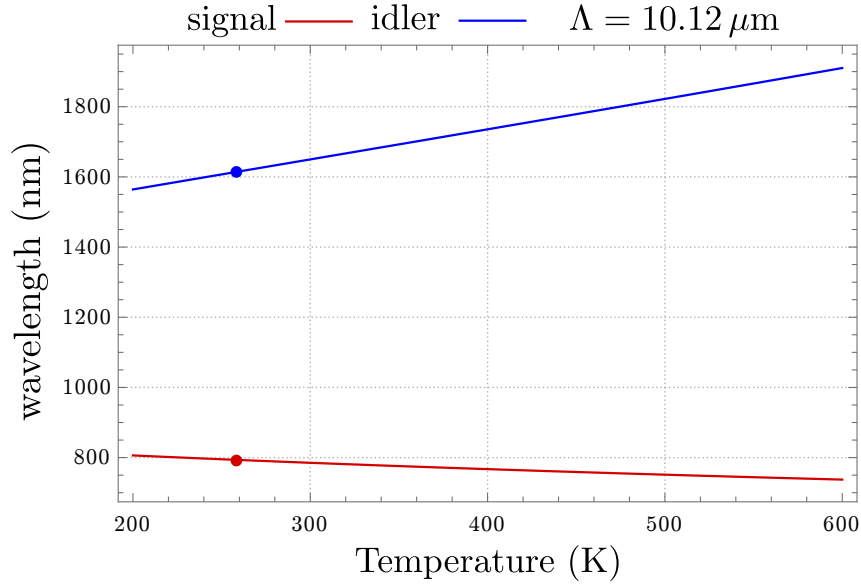


Figure 5.2: SNLO simulation of output wavelengths for a pump wavelength of 532 nm in function of the temperature. The polling period was fixed at  $\Lambda \approx 10.12 \mu\text{m}$ .

the temperature. This gives us the idea of how tunable our system is without leaving the ideal low-temperature range to correct eventual fabrication polling period inaccuracy. We set the ideal polling ( $\Lambda \approx 10.12 \mu\text{m}$ ) and simulate the output wavelengths in function of the temperature, Fig. 5.2. Analyzing the graph, we see that the temperature region  $-40^\circ$  to  $0^\circ \text{C}$  provides a reasonable tunable range for the ideal crystal, with  $\pm 5\text{K}$  around the desired wavelength at 795 nm. Inaccuracy in polling period fabrication should happen in a way to decrease the phase matching temperature.

## 5.2 OPO cavity design

For a triply resonant cavity, the beams' waist is different for each wavelength and is defined by cavity parameters. We have seen in the last section that maximum conversion happens when the pump beam matches the Kleinman-Boyd parameters. Thus, we would like to design our resonator so that the beam is optimally focused inside the nonlinear crystal. In the case of a Fabry-Perot cavity with two curved mirrors, the required waist is given by

$$w_j^2 = \frac{L_j \lambda_j}{\pi} \sqrt{\frac{g_{1,j} g_{2,j} (1 - g_{1,j} g_{2,j})}{g_{1,j} + g_{2,j} - 2g_{1,k} g_{2,j}}}, \quad (5.2.1)$$

where

$$g_{k,j} = 1 - \frac{L_j}{R_k}, \quad (5.2.2)$$

and  $R_k$  is radius of curvature of the mirror labeled by  $k \in \{\text{in}, \text{out}\}$ ,  $L_j$  is the cavity length and  $\lambda_j$ , with  $j \in \{0, 1, 2\}$  labeling pump, signal and idler, respectively (Fig. 5.3). The length of the cavity is different for different wavelengths and polarizations because the crystal introduces propagation shifts by the index of refraction dependence with these factors. The effective cavity length for the propagation and evolution of the transverse mode will be given by

$$L_j = L + l \left( \frac{1}{n_j} - 1 \right). \quad (5.2.3)$$

These waists will enter in the expressions for the calculation of the predicted oscillation threshold.



This length should not be confounded with the optical length of the cavity, which will be taken into account for calculations of cavity bandwidths:

$$\mathcal{L}_j = L + l(n_j - 1). \quad (5.2.4)$$

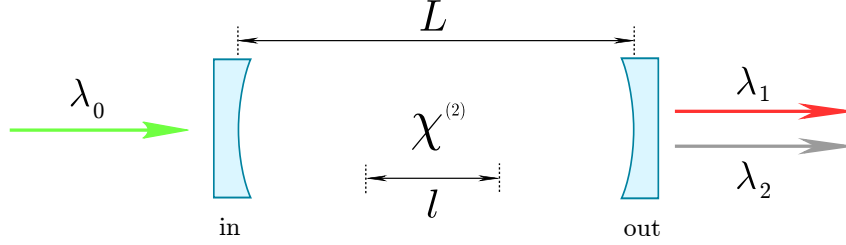


Figure 5.3: Basic diagram of a symmetrical linear optical cavity with a nonlinear crystal inside. The pump beam must have its spatial mode shaped to optimize the oscillation threshold.

The elements that compose the optical cavity must be chosen, considering the system's stabilization properties, oscillation threshold, and separation between oscillation peaks. They depend directly on the geometry and reflectivity of the cavity mirrors. We use two concave spherical mirrors of the same radius manufactured by Layertec, which form a symmetrical Fabry-Perot cavity. The radius of curvature is equal to  $R = 10$  mm, and the transverse diameter of the mirrors is  $\approx 7$  mm. In Fig. 5.4 we find the transmissions  $T$  (%) for the input and output mirrors.

The input mirror is partially reflector for 532 nm ( $T_{532}^{\text{in}} \approx 25\%$ ), and highly reflective to the wavelengths of the twin beams ( $T_{795,1068}^{\text{in}} \lesssim 0.1\%$ ). While the output mirror is highly reflective for 532 nm ( $T_{532}^{\text{out}} \lesssim 0.1\%$ ) and partially reflector for signal and idler ( $T_{795,1068}^{\text{out}} \lesssim 5\%$ ). The finesse of the OPO cavity measured at 532 nm is  $F_{532} = 20$  and we expect that for idler/signal  $F_{795,1068} \approx 120$ . For this configuration the ideal cavity length is about 26 mm and we will get a threshold of  $\approx 5$  mW with a bandwidth of  $\approx 33$  MHz.

We can plot optimized threshold graphs with these parameter values as a function of the geometric cavity length and mirror configurations to find a configuration with a low oscillation threshold and a geometry that leads to an experimentally feasible bandwidth to work with. In Fig. 5.5 we see tests of two mirror configurations where it is evident that mirrors with a smaller radius of curvature lead to smaller cavities. This leads to larger bandwidths, consequently, more interesting working conditions to measure entanglement.

### 5.3 Results for the received PPKTPs

Once we had the mirrors and the crystal, we built our OPO. On this first try, the # 1 batch of crystals showed manufacturing problems. After sending the crystals back to Israel and receive the same crystals with the reported problem corrected, we tried once more to build the desired OPO. This trial, we call Raicol #2.

We follow by describing the problems for the two tests and the current stage of our system.

#### 5.3.1 Raicol #1: coating

After a long wait for the new mirrors for constructing the optical parametric oscillator, we had the unfortunate surprise of discovering that the PPKTP crystals showed very high losses with a single passage of light, incompatible with those specified. We expected losses  $< 0.5\%$  for the desired

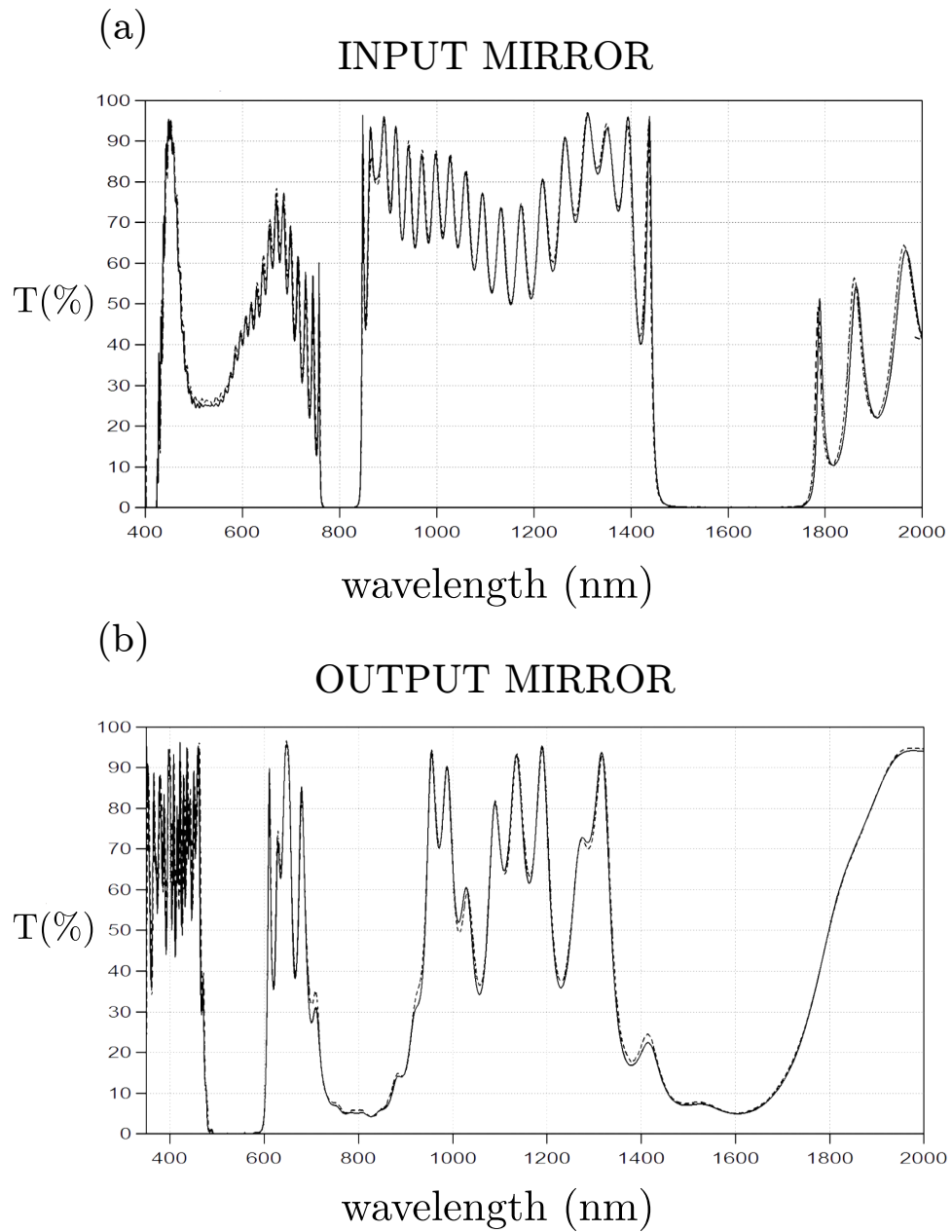


Figure 5.4: (a) Input mirror transmission. (b) Output mirror transmission. The measurements were performed by the mirror manufacturer (Layertec), and the error of  $\pm 0.1\%$ .

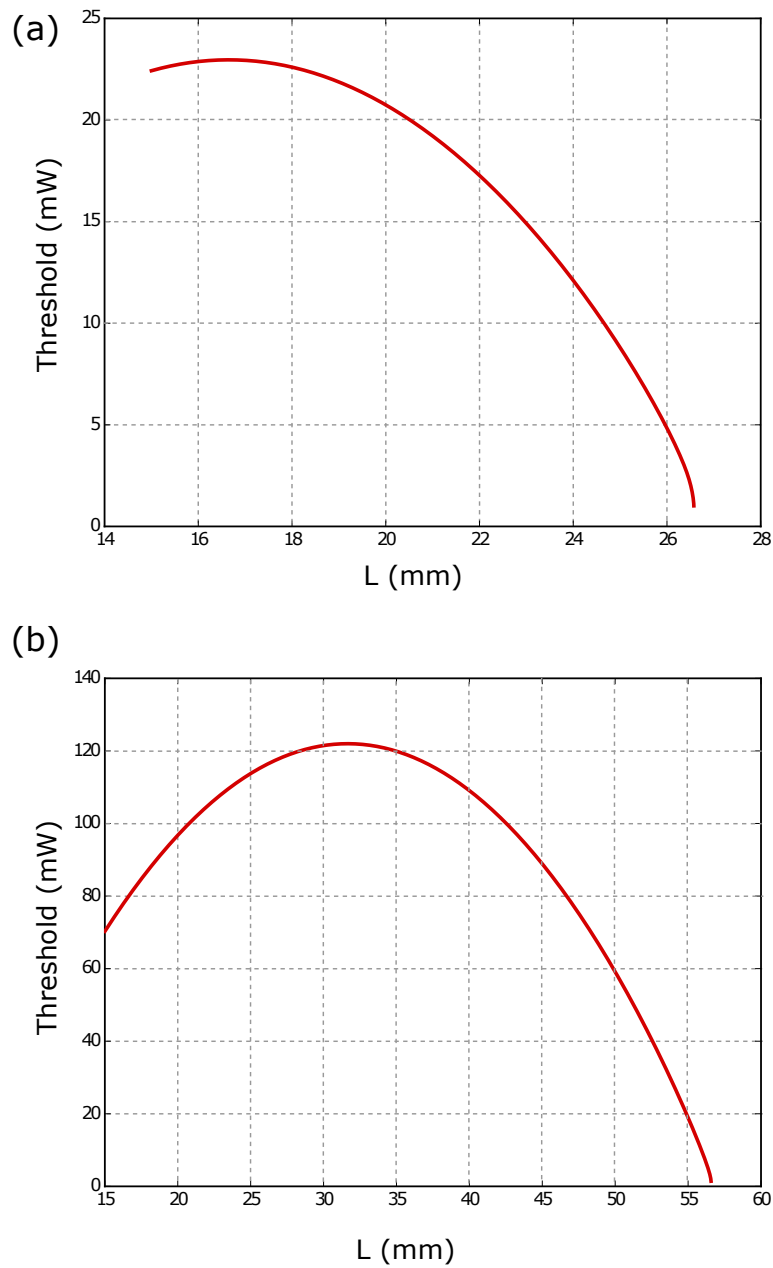


Figure 5.5: Oscillation threshold for a TROPO, the waist is optimized for the length of the cavity. Radius of curvature of the mirrors: (a)  $R = 10$  mm; (b)  $R = 25$  mm.

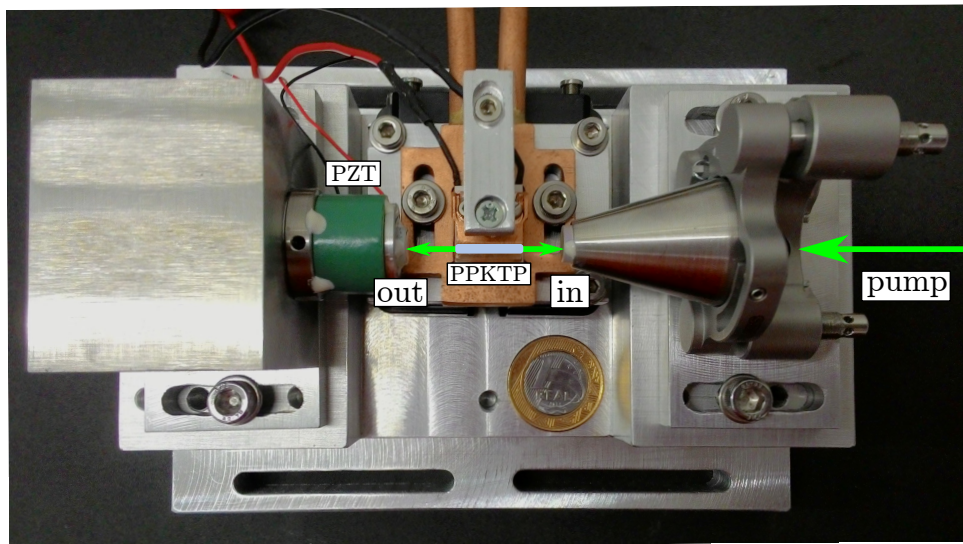


Figure 5.6: Photo of the experimental implementation of the OPO system. In the picture, we can see the optical cavity and the PPKTP crystal. The PZT is a ring-shaped piezoelectric ceramic material used to control the cavity size (glued to the output mirror). The structure is constructed on a heavy aluminum plate for mechanical stability.

wavelengths (532 nm, 795 nm, and 1608 nm), but the initial tests showed losses of 13 % to 532 nm and 8% to 795 nm. A simple test analyzing the transmission of a continuous spectrum light source shows the crystal's transmission at different wavelengths. The result shown 5.7 confirms that the crystal had a wrong anti-reflective treatment.

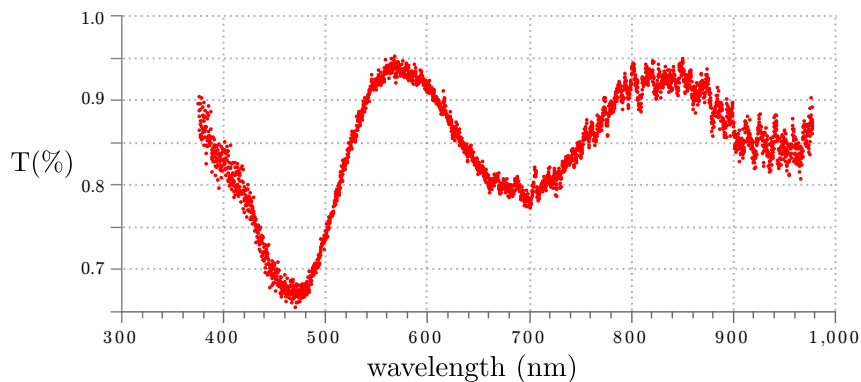


Figure 5.7: Transmission through the received PPKTP crystal (Raicol #1) as a function of wavelength.

We could not achieve parametric oscillation with the measured losses, and even if we could, this system would be useless for quantum information purposes.

### 5.3.2 Raicol # 2: coating, phase-matching, and threshold

We sent the crystals back to the manufacturer to be re-polished and re-coated. We measured the light transmission through the crystal once again and confirmed that the coating was satisfactory. Our measurements are compatible with a plot of reflection in function of wavelengths for the two crystal surfaces (S1 and S2) provided by Raicol (Fig. 5.8).

Once we had verified the coating's quality, we put the crystal inside the cavity and pumped the OPO in room temperature conditions. We would expect to see oscillation even though not in the desired wavelength from our simulations in the previous sections from our simulations in the previous section. However, no oscillation occurred, even if we cool the crystal down to 0 °C. After

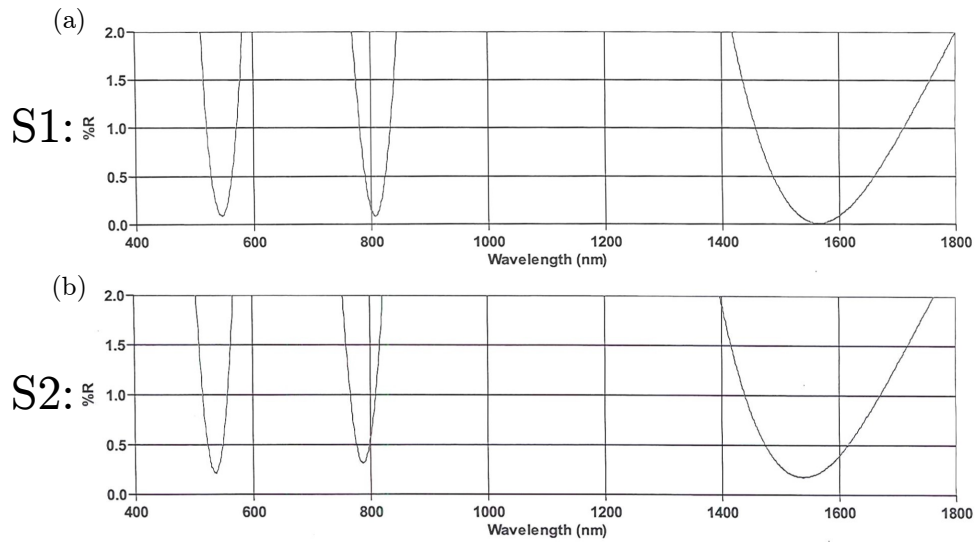


Figure 5.8: Reflection of the two surfaces of the crystal in function of the wavelength. (a) S1 surface 1. (b) S2 surface 2. The overall transmission is a combination of the two reflections. Raicol provided this plot, but our measurements confirm the data.

checking the alignment and polarization, we investigated the cavity losses, and we could not reach the oscillation threshold even going to 20 times the expected oscillation threshold of 5 mW. Eventually, we heated the crystal that reached the oscillation condition at 60 °C.

The measurements showed that we could achieve the desired wavelengths with acceptable losses but only with a crystal temperature close to 185 °C. This high temperature for phase-matching may lead to phonon noise contribution destroying the quantum correlation we want to measure. The reason for this unexpected behavior is that the polling period of the crystal is wrong. The internal process has a period from the expected 9.952  $\mu\text{m}$  to 9.525  $\mu\text{m}$ . With the available pump power, the OPO starts to oscillate only at temperatures > 40 °C. After optimizing the system to increase the temperature, we measured the output wavelengths and the oscillating threshold changing the temperature; the results are shown in Fig. 5.9 and 5.10.

In conclusion, we could achieve a functional operation of the OPO, although far from the desired temperature. Consequently, a new order was filled, replacing the batch we have received, at the polling period of 10  $\mu\text{m}$ . This latest batch provided the same oscillation threshold powers of (5.10), but much lower phase-matching temperatures, Fig. 5.11. The 795 nm wavelengths is reached at temperature  $\approx -43^\circ\text{C}$ .

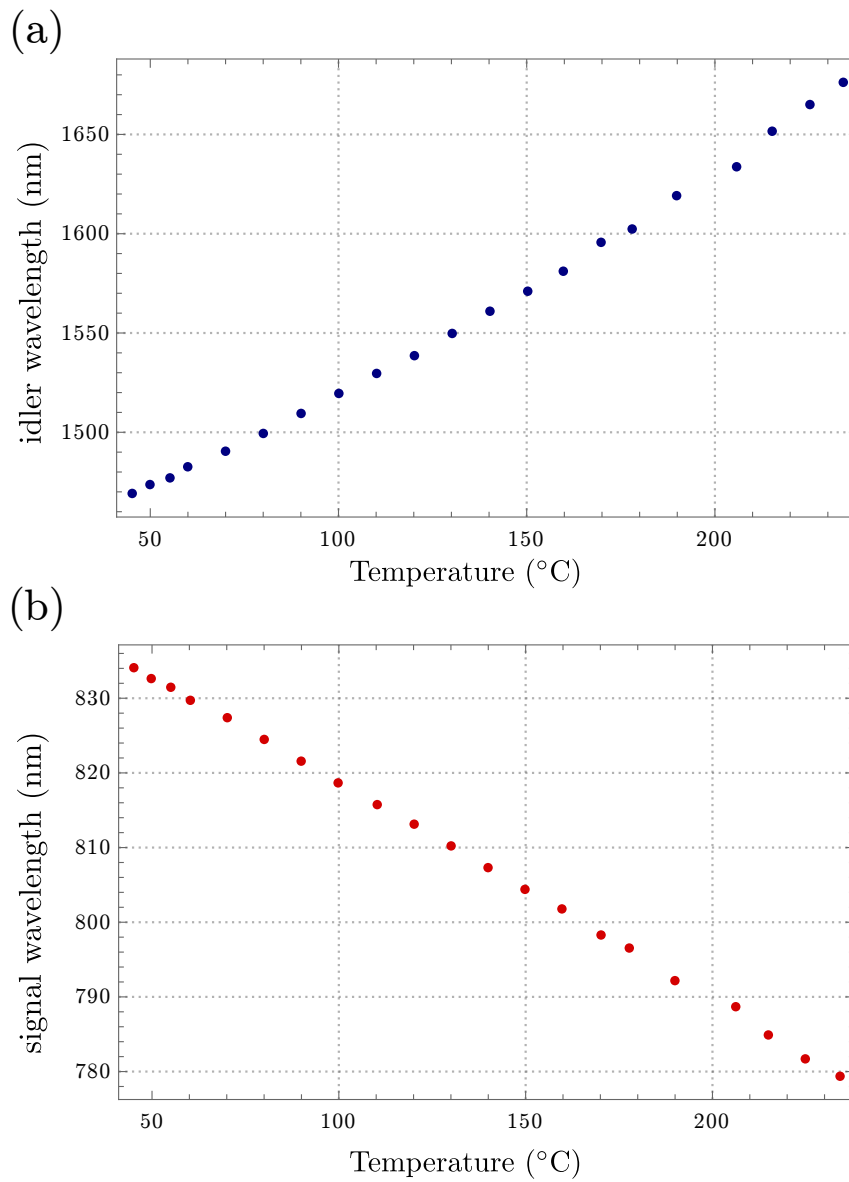


Figure 5.9: TROPO output in function of crystal temperature (a) idler wavelengths. (b) signal wavelengths. The Rubidium D1 line is achieved at temperature  $\approx 185^\circ\text{C}$ .

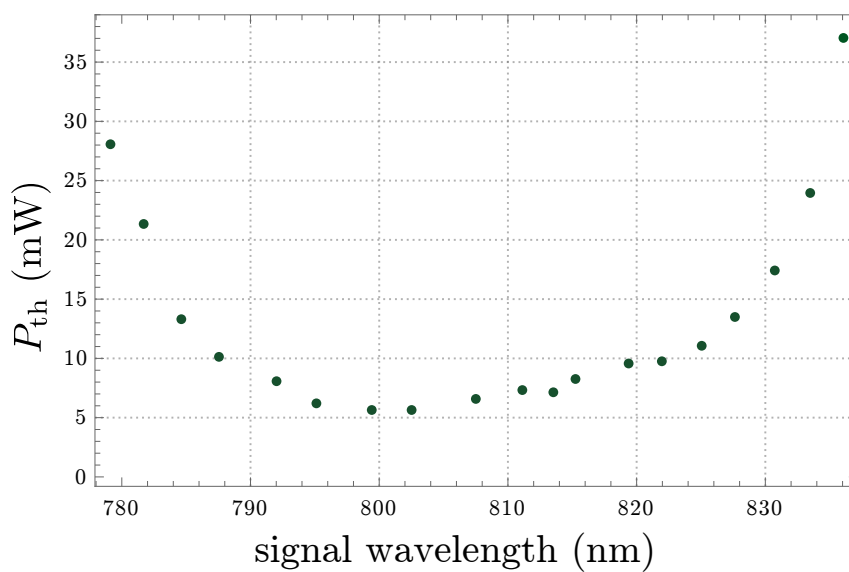


Figure 5.10: TROPO threshold power dependence on the signal wavelength.

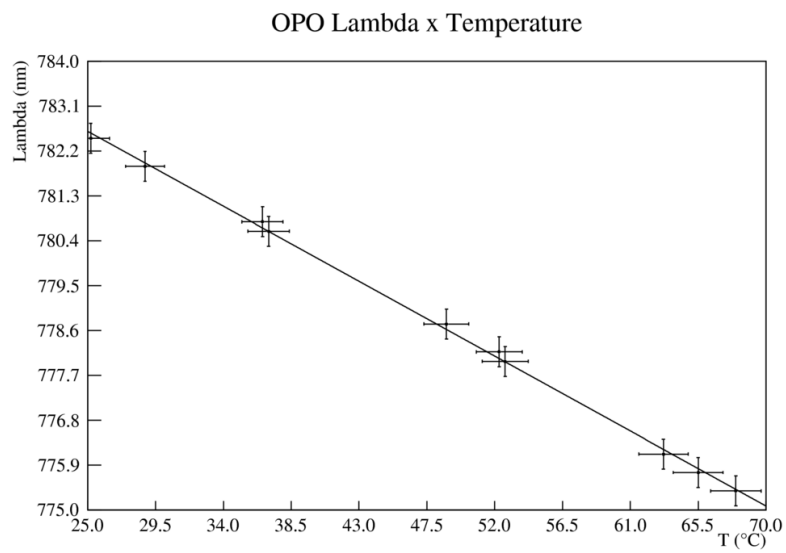


Figure 5.11: TROPO signal wavelengths output in function of crystal temperature. The Rubidium D1 line is estimated to be achieved achieved at temperature  $\approx -43$  °C.

## Chapter 6

# Conclusion and future work

From the basic tools of nonlinear and quantum optics, we designed and built two Optical Parametric Oscillators aiming at distinct purposes. The main common feature is the use of entanglement between different colors.

At the Niels Bohr Institute, we built and characterized a nondegenerate OPO that successfully produced entangled states below the oscillation threshold. We violate the separability criteria,  $\text{Var}[\hat{X}_-] + \text{Var}[\hat{Y}_+] \approx 0.32 < 2$  down to 350 kHz for a pair of fields at 852 nm and 1064 nm. To the best of our knowledge, it corresponds to the highest violation for two-color entanglement measured in continuous variables. This is the first step into implementing a link between a Gravitational Wave Detector (at 1064 nm) and an atomic ensemble (Cs atoms, at 852 nm). Calculations show that an increase of 6 dB in the sensitivity can be achieved by implementing the techniques for evading the quantum back action, which will rely on the generation of these entangled modes.

At the Physic Institute at the University of São Paulo, we looked for the generation of entanglement in the above threshold operation. Knowing that entanglement in intense fields is deteriorated by phase noise, depending on temperature and intracavity power, we aimed at building an OPO with phase matching for 795 nm and 1608 nm at temperature  $\approx -40^\circ$  and an oscillation threshold of 5 mW. Although severe problems with the manufacturing of the crystals, we could achieve a stable operation of the OPO, although far from the desired temperature. Nevertheless, these results certify our proposed design. With the new crystals, we can achieve a quantum interface for teleportation protocols involving rubidium atoms, coupling the D1 line at 795 nm to the telecom L-band at 1608 nm.





# Appendices



# Appendix A

## Light Modulation

### A.0.1 Oscillating functions and the simple harmonic oscillator

We begin by describing the nature of the oscillating function. This will define simple concepts that will become more complex and subtle in the quantum description of the systems we work in our lab. We can describe a time oscillating function in a given frequency  $\omega$  by two parameters

$$f(t) = A \cos(\omega t - \phi), \quad (\text{A.0.1})$$

We usually call  $A$  the amplitude and  $\phi$  the phase of the quantity that  $f(t)$  is describing. Another way to write the above function is

$$f(t) = a \cos \omega t + b \sin \omega t, \quad (\text{A.0.2})$$

with  $a = A \cos \phi$  and  $b = A \sin \phi$  called *quadratures*, which are  $\pi/2$  phase separated amplitudes;  $a$  is related to the cosine part and  $b$  is related to the sine part of  $f(t)$ . In the literature is common to call  $a$  the *cosine quadrature* and  $b$  the *sine quadrature*. In this case, it is more convenient to work with complex numbers than with trigonometric functions, for that reason we write the complex amplitude

$$\tilde{f}(t) = A e^{i(\phi - \omega t)}, \quad (\text{A.0.3})$$

and is trivial to show that  $f(t) = \text{Re}[\tilde{f}(t)]$ . The correspondence between the two ways of express the same oscillation function is given by

$$a = \text{Re}[\tilde{f}(0)] = A \cos \phi, \quad b = \text{Im}[\tilde{f}(0)] = A \sin \phi, \quad (\text{A.0.4})$$

$$A = \sqrt{a^2 + b^2}, \quad \phi = \arctan[b/a]. \quad (\text{A.0.5})$$

The simple harmonic oscillator (SHO) is at the heart of the oscillating phenomenon. Any system weakly perturbed in the surrounding of an equilibrium point will follow the same kind of SHO restoring force that will execute an oscillating motion going back and forth the equilibrium point. The Hamiltonian of a simple harmonic oscillator is

$$H = \frac{p^2}{2m} + \frac{1}{2} m \omega^2 q^2, \quad (\text{A.0.6})$$

where  $q$  is the position,  $p$  is the momentum,  $m$  is the particle mass and  $\omega$  is the oscillating frequency. From Hamilton's equations of motion we get

$$\dot{q} = p/m, \quad \text{and} \quad \dot{p} = -m\omega^2 q, \quad (\text{A.0.7})$$

that imply in  $\ddot{q} = -\omega^2 q$ . We can use a trick to eliminate the unities in our problem. Changing the energy scale as

$$E_c \mathcal{H} = \frac{p_c^2}{2m} \mathcal{P}^2 + \frac{1}{2} m \omega^2 q_c^2 \mathcal{Q}^2, \quad (\text{A.0.8})$$

by choosing the scales in the form  $E_c = p_c^2/m = m\omega^2 q_c^2$ , the Hamiltonian becomes

$$\mathcal{H} = \frac{1}{2} (\mathcal{Q}^2 + \mathcal{P}^2), \quad (\text{A.0.9})$$

which give  $\ddot{\mathcal{Q}} + \omega^2 \mathcal{Q} = 0$ , as well. The solutions to the second order differential equation will be of the form

$$\mathcal{Q}(t) = \mathcal{Q}(0) \cos \omega t + \mathcal{P}(0) \sin \omega t, \quad (\text{A.0.10})$$

$$\mathcal{P}(t) = -\mathcal{Q}(0) \sin \omega t + \mathcal{P}(0) \cos \omega t, \quad (\text{A.0.11})$$

defining

$$\alpha(t) = \frac{\mathcal{Q}(t) + i\mathcal{P}(t)}{2} = \alpha(0) e^{-i\omega t}, \quad (\text{A.0.12})$$

then, the time evolution is just a clockwise rotation of the phasor  $\alpha$  in a  $(\mathcal{Q}, \mathcal{P})$  complex plane. Note that the quadratures of this oscillating function are exactly the position and momentum of SHO; given by

$$\mathcal{Q}(t) = 2\text{Re}[\alpha(t)] = \alpha(t) + \alpha^*(t), \quad (\text{A.0.13})$$

$$\mathcal{P}(t) = 2\text{Im}[\alpha(t)] = (\alpha(t) - \alpha^*(t))/i. \quad (\text{A.0.14})$$

The phase space trajectory<sup>1</sup> is simply a constant energy circumference of radius  $r = \sqrt{\mathcal{Q}^2 + \mathcal{P}^2}$ . The Hamiltonian can also be expressed as

$$\mathcal{H} = 2\alpha^* \alpha \quad (\text{A.0.15})$$

we call the pair  $\{\alpha, \alpha^*\}$  the *normal variables* of the oscillator.

## A.0.2 Classical electromagnetical waves

A well behaved oscillating signal  $f(t)$  can always be decomposed using Fourier's theorem as

$$f(t) = \int_{-\infty}^{\infty} \tilde{f}(\omega) e^{-i\omega t} \frac{d\omega}{2\pi}, \quad \text{with} \quad \tilde{f}(\omega) = \int_{-\infty}^{\infty} f(t) e^{i\omega t} dt, \quad (\text{A.0.16})$$

turns out that if the signal is real we have the following relation:  $\tilde{f}^*(\omega) = \tilde{f}(-\omega)$ . This will allow us to decompose the integral and consider only positive frequencies ( $\omega > 0$ ). Decomposing the Fourier integral and using the reality of the signal we can write

$$f(t) = \underbrace{\int_0^{\infty} \tilde{f}(\omega) e^{-i\omega t} \frac{d\omega}{2\pi}}_{\text{positive frequency component}} + \underbrace{\int_0^{\infty} \tilde{f}^*(\omega) e^{i\omega t} \frac{d\omega}{2\pi}}_{\text{negative frequency component}}, \quad (\text{A.0.17})$$

the positive frequency component is denoted by  $f^{(+)}(t)$  and the negative frequency component by  $f^{(-)}(t)$ . Now  $f(t)$  is the sum

$$f(t) = f^{(+)}(t) + f^{(-)}(t) = \text{Re}[2f^{(+)}(t)], \quad (\text{A.0.18})$$

<sup>1</sup>For a system with  $N$  degrees of freedom and  $2N$   $q$ 's and  $p$ 's canonical variables the phase space is a  $2N$ -dimensional space in which  $\{q_1, p_1, \dots, q_N, p_N\}$  are plotted as variables.

where  $f^{(+)}(t) = [f^{(-)}(t)]^*$  and  $f^{(+)}(t)$  is called the “analytic signal” in the literature. From the wave equation

$$\left( \frac{\partial^2}{\partial z^2} - \frac{1}{v^2} \frac{\partial^2}{\partial t^2} \right) \psi(z, t) = 0, \quad (\text{A.0.19})$$

where  $v$  is the speed of propagation of the wave, the boundary condition  $\psi(z = 0, t) = f(t)$  gives the solution at all  $(z, t)$  coordinates by applying a translation

$$\psi(z, t) = \begin{cases} f(t - z/v) & (v > 0) \\ f(t + z/v) & (v < 0) \end{cases}, \quad (\text{A.0.20})$$

if our signal is  $f(t) = \text{Re}[\tilde{f}e^{-i\omega t}]$  we get

$$\psi(z, t) = \text{Re}[\tilde{f}e^{i(\pm kz - \omega t)}], \quad (\text{A.0.21})$$

where  $k = \omega/v$ . For a polychromatic signal

$$\psi = \underbrace{\int_0^\infty d\omega [\tilde{f}(\omega) + \tilde{f}^*(\omega)] e^{i(kz - \omega t)}}_{\text{forwards}} + \underbrace{\int_0^\infty d\omega [\tilde{f}(\omega) + \tilde{f}^*(\omega)] e^{i(-kz - \omega t)}}_{\text{backwards}}, \quad (\text{A.0.22})$$

the “full wave” (forwards + backwards) can be described as

$$\psi(z, t) = \int_{-\infty}^\infty dk \tilde{f}(\omega_k) e^{i(kz - \omega_k t)} + \int_{-\infty}^\infty dk \tilde{f}^*(\omega_k) e^{-i(kz - \omega_k t)}. \quad (\text{A.0.23})$$

We can apply the same formalism for an electromagnetic (EM) wave, starting with Maxwell’s equations, we will have

$$\mathbf{E}(\mathbf{r}, t) = \sum_{\mu} \int d^3\mathbf{k} \tilde{\mathbf{E}}(\omega_k) \epsilon_{\mu} e^{i(\mathbf{k} \cdot \mathbf{r} - \omega_k t)} + \sum_{\mu} \int d^3\mathbf{k} \tilde{\mathbf{E}}^*(\omega_k) \epsilon_{\mu} e^{-i(\mathbf{k} \cdot \mathbf{r} - \omega_k t)}, \quad (\text{A.0.24})$$

where  $\mathbf{E}(\mathbf{r}, t)$  is the electric field vector in a given position  $\mathbf{r}$  and instant  $t$ . The above equation is the standard Fourier decomposition.  $\epsilon_{\mu}$  is the polarization vector and  $\mathbf{k}$  the wave vector. Is easy to see that  $\epsilon_{\mu} \cdot \mathbf{k} = 0$  means that the EM wave is transverse.

### A.0.3 Light modulation

Consider a perfect monochromatic linearly polarized light wave propagating in positive  $z$ -axis, with oscillating frequency  $\omega_0$ . The field can be fully characterized by the strength of the electric field  $E(t - z/c)$ , which can be written in three equivalent forms:

$$E(\zeta) = \mathcal{E}_0 \cos[\omega_0 \zeta - \phi_0] \equiv \mathcal{E}^c \cos \omega_0 \zeta + \mathcal{E}^s \sin \omega_0 \zeta \equiv \frac{\mathcal{E} e^{-i\omega_0 \zeta} + \mathcal{E}^* e^{i\omega_0 \zeta}}{\sqrt{2}}, \quad (\text{A.0.25})$$

now we want to describe how modulation in the amplitude or phase affects the light wave, this will be very important to understand the concept of *sidebands* and for quantum optics in continuous variables is the starting point of many experimental descriptions, especially at out lab.

Lets assume that our wave has amplitude  $\mathcal{E}_0$  and initial phase  $\phi_0 = 0$

$$E_{\text{car}}(t) = \mathcal{E}_0 \cos \omega_0 t = \text{Re}[\mathcal{E}_0 e^{-i\omega_0 t}], \quad (\text{A.0.26})$$

we will call the above field the *carrier wave*. Imagine now that one is able to modulate the amplitude in a modulation frequency  $\Omega$  slow compared to the carrier frequency,  $\Omega \ll \omega_0$ , then the resultant wave will be

$$E_{AM}(t) = \mathcal{E}_0[1 + \epsilon_m \cos(\Omega t + \phi_m)] \cos \omega t, \quad (\text{A.0.27})$$

where the constants  $\epsilon_m$  and  $\phi_m$  are called modulation depth and relative phase, respectively. The complex amplitude of this modulated wave is equals to

$$\mathcal{E}_{AM}(t) = \frac{\mathcal{E}_0}{\sqrt{2}}[1 + \cos(\Omega t + \phi_m)], \quad (\text{A.0.28})$$

and comparing with the carrier quadrature we have the transformation

$$\mathcal{E}_{AM}^c(t) = \mathcal{E}_0[1 + \cos(\Omega t + \phi_m)], \quad \text{and} \quad \mathcal{E}_{AM}^s(t) = 0. \quad (\text{A.0.29})$$

The effect of amplitude modulation, in this simple case, shows up only in the quadrature that is in phase with the carrier wave. This fact is responsible for the usually adopted terminology in literature *amplitude quadrature*. From now on, we will use this terminology. From the spectrum point of view, there is also a change, is straightforward to show that the single-frequency amplitude modulation can be written

$$E_{AM}(t) = \text{Re} \left[ \mathcal{E}_0 e^{-i\omega_0 t} + \frac{\mathcal{E}_0}{2} \epsilon_m e^{-i\phi_m} e^{-i(\omega_0 + \Omega)t} + \frac{\mathcal{E}_0}{2} \epsilon_m e^{i\phi_m} e^{-i(\omega_0 - \Omega)t} \right], \quad (\text{A.0.30})$$

the spectrum acquires two new frequencies equally spaced in relation to the carrier, they are called *sidebands*.

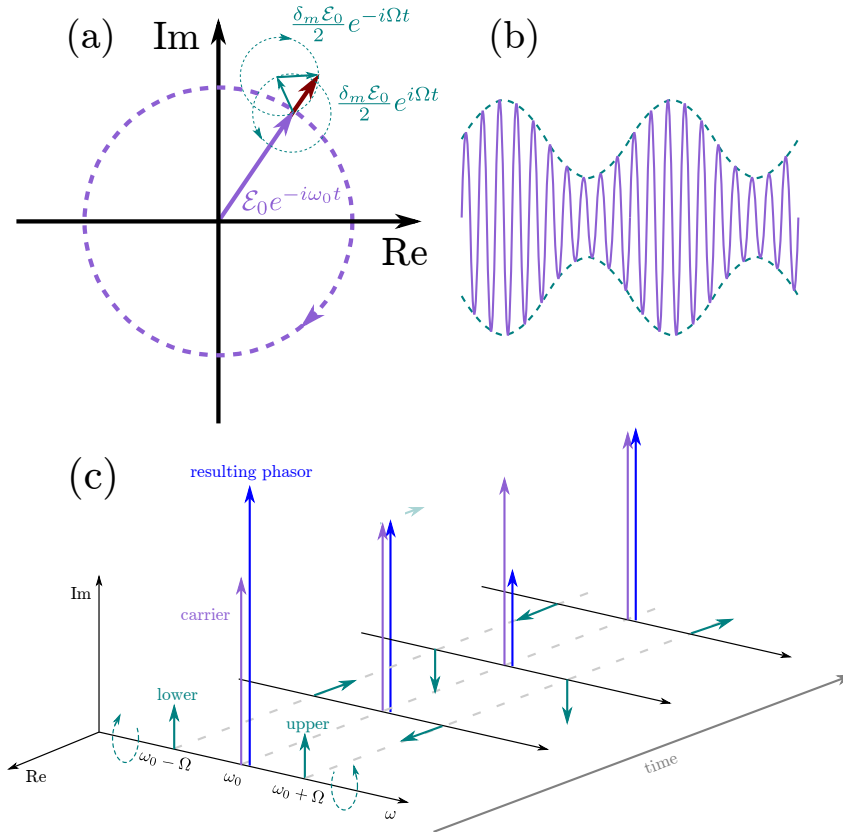


Figure A.1: Representations of amplitude modulation. (a) Phase space. (b) Wave picture. (c) Phase space evolution in the  $\omega_0$  rotating frame.

Modulation in the phase of a wave is also an important case. The simplest case is given by

$$E_{\text{PM}}(t) = \mathcal{E}_0 \cos[\omega_0 t + \delta_m \cos(\Omega t + \phi_m)], \quad (\text{A.0.31})$$

where  $\Omega \ll \omega_0$ , and the phase deviation  $\delta_m$  is much smaller than 1. The complex amplitude of the phase-modulated light is

$$\mathcal{E}_{\text{PM}}(t) = \frac{\mathcal{E}_0}{\sqrt{2}} e^{i\delta_m \cos(\Omega t + \phi_m)}, \quad (\text{A.0.32})$$

and the quadratures in the weak modulation limit ( $\delta_m \ll 1$ ), the approximated expression can be written

$$\mathcal{E}_{\text{PM}}^c \simeq \mathcal{E}_0, \quad \text{and} \quad \mathcal{E}_{\text{PM}}^s(t) \simeq \delta_m \mathcal{E}_0 \cos(\Omega t + \phi_m), \quad (\text{A.0.33})$$

now only the sine quadrature contain the modulation signal, contrary to amplitude modulation is the  $\pi/2$  out-of-phase with respect to the carrier that is changing over time. That is the reason the sine quadrature is usually referred as *phase quadrature*. To understand the spectrum change, we express the field as

$$E_{\text{PM}}(t) \simeq \text{Re} \left[ \mathcal{E}_0 e^{i\omega_0 t} + i \frac{\delta_m \mathcal{E}_0}{2} \left( e^{i[(\omega_0 + \Omega)t + \phi_m]} + e^{i[(\omega_0 - \Omega)t - \phi_m]} \right) \right], \quad (\text{A.0.34})$$

and again we see the modulation giving as result the creation of sidebands around the carrier frequency.

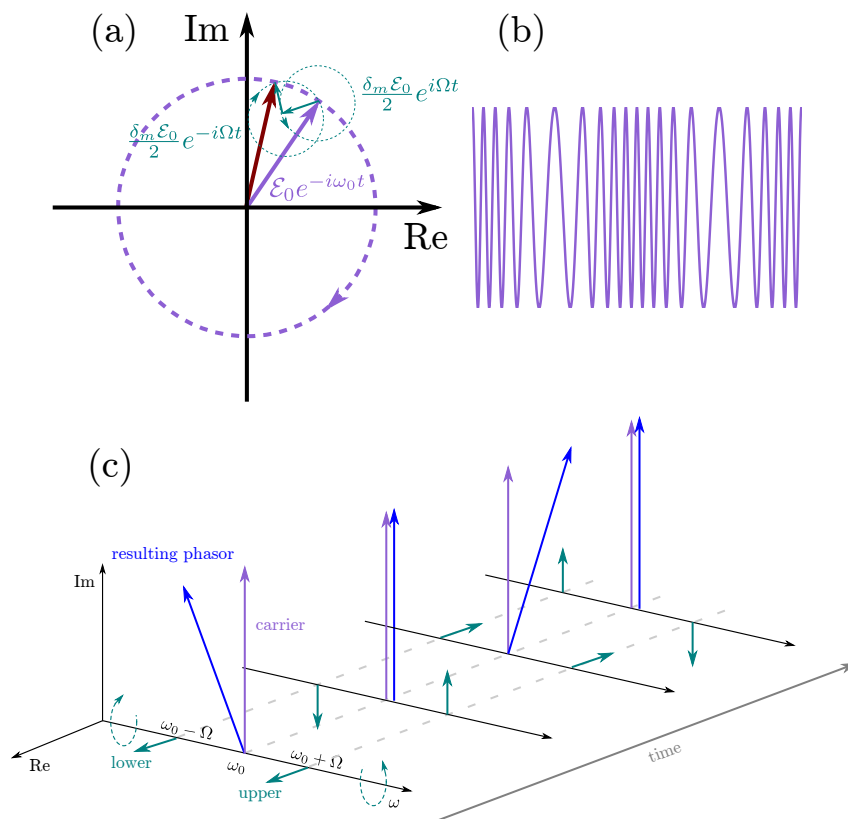


Figure A.2: Representations of phase modulation. (a) Phase space. (b) Wave picture. (c) Phase space evolution in the  $\omega_0$  rotating frame.





## Appendix B

# Gaussian beams and resonators

In the laboratory we usually work with light propagating in a given direction, for example, along the  $z$ -axis. Then the spatial mode function can be written as  $u(\mathbf{r}) = \Phi(\mathbf{r})e^{-ikz}$ . Assuming the paraxial approximation [62], the Helmholtz equation takes the form

$$\frac{\partial^2 \Phi}{\partial x^2} + \frac{\partial^2 \Phi}{\partial y^2} + 2ik \frac{\partial \Phi}{\partial z} = 0, \quad (\text{B.0.1})$$

with general solution given by the expression

$$\Phi_{mn}(\mathbf{r}) = \mathcal{N} \frac{w_0}{w(z)} \exp\left[-\frac{x^2 + y^2}{w^2(z)}\right] \exp\left[-ik \frac{x^2 + y^2}{2R(z)}\right] H_m\left[\frac{x\sqrt{2}}{w(z)}\right] H_n\left[\frac{y\sqrt{2}}{w(z)}\right] e^{i\phi_{mn}(z)}, \quad (\text{B.0.2})$$

where  $\mathcal{N}$  is an arbitrary constant. In (B.0.2)  $w$  is the beam width,  $R$  is the radius of curvature of the wave front and  $\phi_{mn}(z)$  is called the *Gouy phase*. They are function of  $z$  given by

$$w(z) = w_0 \sqrt{1 + \left(\frac{z}{z_R}\right)^2}, \quad (\text{B.0.3})$$

$$R(z) = z \left[1 + \left(\frac{z}{z_R}\right)^2\right], \quad (\text{B.0.4})$$

$$\phi_{mn}(z) = (m + n + 1) \arctan\left(\frac{z}{z_R}\right). \quad (\text{B.0.5})$$

The constant  $w_0$  describes the minimum beam width and is called *beam waist*. The *Rayleigh length*  $z_R \equiv \pi w_0^2/\lambda$ . These solutions are called *Hermite-Gauss* modes. They form a discrete basis of solutions of equation (B.0.1) and usually denoted  $\text{TEM}_{mn}$ . Figure B.1 shows 8 examples of intensity distribution of the firsts TEM modes. Is important to note that all  $\text{TEM}_{mn}$  modes have the same phase transverse dependence and differ only by the Gouy phase propagation and transverse amplitude profile. The  $\text{TEM}_{00}$  mode is called the *fundamental Gaussian* mode, with intensity

$$I_{00} \propto \left[\frac{w_0}{w(z)}\right]^2 \exp\left[-\frac{2(x^2 + y^2)}{w^2(z)}\right], \quad (\text{B.0.6})$$

the intensity profile is Gaussian with respect to transverse distance from the propagation axis. The width grows with increase the absolute value of  $z$ . For  $|z| \gg 1$  the opening angle stay fixed at  $\theta = \arctan(2/kw_0)$ , see Figure B.2.

In day-to-day lab work, the spatial degree of freedom of laser beams has to be carefully manipulated. Usually one needs to shape an given beam to a specific spatial mode because inference effects depend

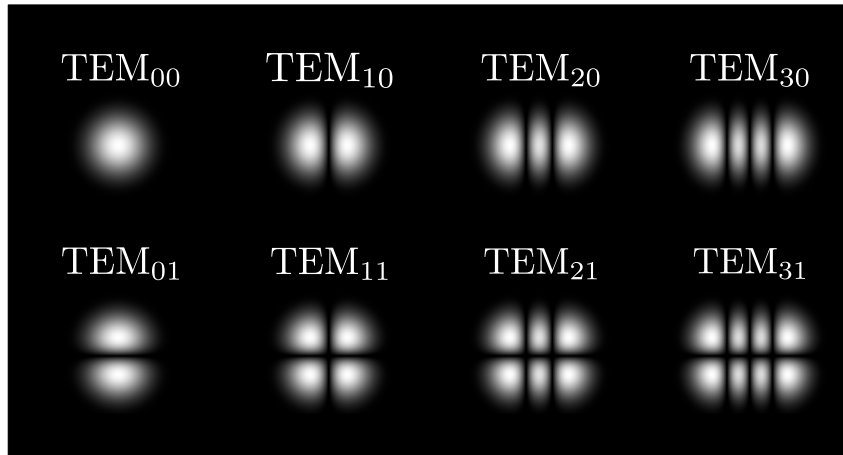


Figure B.1: Intensity distribution of few Hermite-Gauss modes.

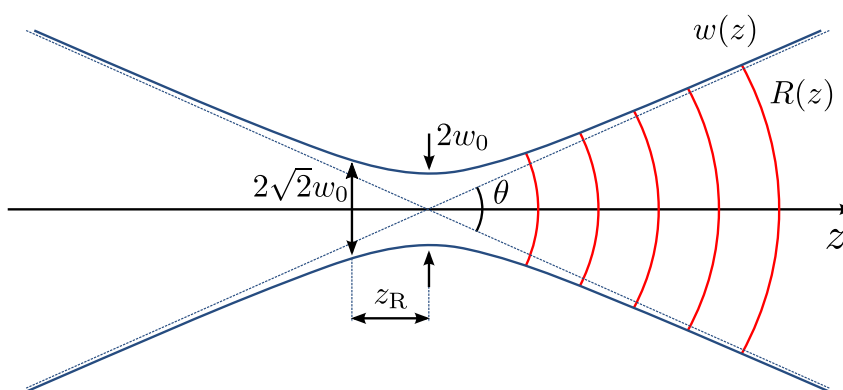


Figure B.2: Graphical description of the main parameters of the fundamental mode as function of propagation.

strongly of spatial-mode overlap. Therefore, in order to couple different beams is necessary to match the spatial modes. This process is called *mode matching*, which is usually done propagating the beam that is going to be matched through lenses, spherical mirrors and the free space. This technique is very important in the context of optical cavities. In our experiment it is necessary to make the mode matching of our pump laser beam with waist  $w_0$  to the resonant mode in the cavity of the OPO of waist  $w_{\text{OPO}}$ , Figure B.3. The calculations are done using the ABCD matrix formalism [62, 127, 154] and the domain of this technique is of fundamental importance when working with optical cavities. In the context of optical parametric oscillators, this technique is well described in other group thesis [112, 113]. We are not going to give details of mode matching calculations in this text. Later, the proprieties of Gaussian beams will be important to understand the theory of OPO efficiency due to mode confinement.



Figure B.3: Mode matching example.



## Appendix C

# Nonlinear Optics

We know that at first approximation, the induced polarization in a dielectric medium is proportional to the electric field acting on the material [62]. However, if the field is strong enough, the linear response regime is overcome, and effects due to nonlinear contributions are observed. When powers of electric fields are included in the expression of polarization, energy can be exchanged between different input fields at different frequencies. In the nonlinear regime, the relationship between the electric field and the induced polarization is given by

$$P_i = \sum_j \chi_{ij}^{(1)} E_j + \sum_j \sum_k \chi_{ijk}^{(2)} E_j E_k + \sum_j \sum_k \sum_l \chi_{ijkl}^{(3)} E_j E_k E_l + \dots, \quad (\text{C.0.1})$$

where  $P_i$ ,  $E_i$ ,  $E_j$  and  $E_k$  are the Cartesian components of vectors  $\mathbf{P}$  and  $\mathbf{E}$  and the indexes take the values  $\{x, y, z\}$ . The proportionality coefficients of each term of the sum (C.0.1) define the linear and nonlinear susceptibilities, where we disregard its dependence with frequency. The linear susceptibility  $\chi_{ij}^{(1)}$  is a tensor of order 2 with 9 components, the second-order nonlinear susceptibility  $\chi_{ijk}^{(2)}$  is a tensor of order 3 with 27 components, while the third-order nonlinear susceptibility  $\chi_{ijkl}^{(3)}$  is a tensor of order 4 with 64 components, and so on. For typical laser intensities the nonlinear terms go to zero very fast [126], and it is sufficient to take only the first nonlinear terms. In centrosymmetric materials, where the polarization is not altered when the system undergoes the transformation ( $\mathbf{r} \Rightarrow -\mathbf{r}$ ) the second-order nonlinear susceptibility is null and  $\chi^{(3)}$  should be taken into account as the first correction factor. We will focus on nonlinear effects involving only  $\chi^{(2)}$ .

The wave equation in a dielectric medium can be written from Maxwell's equations splitting the linear polarization of the nonlinear  $\mathbf{P} = \mathbf{P}_L + \mathbf{P}_{NL}$ , we have

$$\nabla^2 \mathbf{E} - \frac{n^2}{c^2} \frac{\partial^2 \mathbf{E}}{\partial t^2} = -\frac{1}{\epsilon_0 c^2} \frac{\partial^2 \mathbf{P}_{NL}}{\partial t^2}, \quad (\text{C.0.2})$$

where  $n^2 = 1 + \chi^{(1)}$  is the refractive index. The role of nonlinear polarization is to act as a source of radiation that may contain terms oscillating at frequencies different from those of the input electric field. Writing the field in terms of a sum of monochromatic waves

$$E(\mathbf{r}, t) = \sum_l \mathcal{E}_l e^{i(\mathbf{k}_l \cdot \mathbf{r} - \omega_l t)} + c.c., \quad (\text{C.0.3})$$

and to simplify the treatment of (C.0.2) we will consider only waves propagating in the slowly variable envelope approximation [62], for this condition, we have the propagation equation to become

$$\sum_l 2ik_l \frac{d\mathcal{E}_l(z)}{dz} e^{i(k_l z - \omega_l t)} + c.c. = \frac{1}{\epsilon_0 c^2} \frac{\partial^2 P_{NL}}{\partial t^2}, \quad (\text{C.0.4})$$

decomposing  $P_{NL}$  into monochromatic components

$$P_{NL}(z, t) = \sum_l \mathcal{P}_{NL}^{\omega_l}(z) e^{-i\omega_l t} + c.c., \quad (\text{C.0.5})$$

we obtain a set of equations that relate the amplitudes with the components  $\mathcal{P}_{NL}$  of the polarization vector

$$\frac{\mathcal{E}_l(z, t)}{dz} e^{ik_l z} = i \frac{\omega_l}{2\epsilon_0 n_l c} \mathcal{P}_{NL}^{\omega_l}(z). \quad (\text{C.0.6})$$

All we need to do is to express  $\mathcal{P}_{NL}$  in the terms of the amplitudes  $\mathcal{E}_m(z, t)$  at point  $z$  to obtain a set of coupled differential equations that can be solved obtaining the amplitudes  $\mathcal{E}_l(z)$  for the different waves involved in the process. We end up with the closed system of coupled differential equations:

$$\frac{d\mathcal{E}_0}{dz} = i \frac{\omega_0}{n_0 c} \chi^{(2)} \mathcal{E}_1(z) \mathcal{E}_2(z) e^{-i\Delta k}, \quad (\text{C.0.7})$$

$$\frac{d\mathcal{E}_1}{dz} = i \frac{\omega_1}{n_1 c} \chi^{(2)} \mathcal{E}_0(z) \mathcal{E}_2^*(z) e^{i\Delta k}, \quad (\text{C.0.8})$$

$$\frac{d\mathcal{E}_2}{dz} = i \frac{\omega_2}{n_2 c} \chi^{(2)} \mathcal{E}_0(z) \mathcal{E}_1^*(z) e^{i\Delta k}, \quad (\text{C.0.9})$$

where  $\Delta k = k_0 - k_1 - k_2$ . This system therefore couples the three processes. This is called *three-wave mixture*, and is the basis for understanding the optical parametric oscillator.

### C.0.1 Introduction to phase matching

Take equations C.0.7 and C.0.9, but the same discussion can be extended to the equations (C.0.7) and (C.0.8). We can rewrite C.0.9 in the form

$$\frac{d\mathcal{E}_2}{dz} e^{ik_2 z} = i \frac{\omega_2}{n_2 c} \chi^{(2)} \mathcal{E}_0(z) \mathcal{E}_1^*(z) e^{i(k_0 - k_1) z}, \quad (\text{C.0.10})$$

the term  $e^{ik_2 z}$  on the left side of the equation has a wavelength of  $2\pi/k_2$  and the oscillating term on the right side of the equation has a wavelength of  $2\pi/(k_0 - k_1)$ . The right term is related to the induced polarization, and the left term with the optical field generated. We know from Poynting's theorem that the direction of the energy flow is related to the signal of  $\langle \mathbf{E} \cdot \partial \mathbf{P} / \partial t \rangle$ . Thus, if the polarization and field wavelengths are not the same, the phase relationship between field and polarization changes continuously during propagation through the nonlinear medium, which results in periodic energy exchange between field and polarization. The spatial period in which the energy goes to the field and back to the polarization is the coherence length. If the two phases are equal, we say that the process is in *phase matching*. In this situation, the coherence length becomes infinite; that is, the energy is transferred to the field and does not return to the polarization. Typically the coherence length is too small for an appreciable intensity of the generated field. It is necessary to satisfy the condition  $\Delta k = 0$  to achieve the maximum conversion efficiency.

The processes of interaction between fields are given respecting the laws of conservation of energy and momentum. This imposes that the exchange of energy between the modes of the field must obey certain restrictions. Thinking in terms of photons, we can imagine that in a given nonlinear process, an initial amount of photons  $n$  is converted into another integer  $m$  of photons and must respect

$$\hbar \sum_i^n \omega_i = \hbar \sum_f^m \omega_f, \quad \text{and} \quad \hbar \sum_i^n \mathbf{k}_i = \hbar \sum_f^m \mathbf{k}_f, \quad (\text{C.0.11})$$

where indexes  $i$  and  $f$  in the sums represent the initial and final photons, respectively. In the Figure

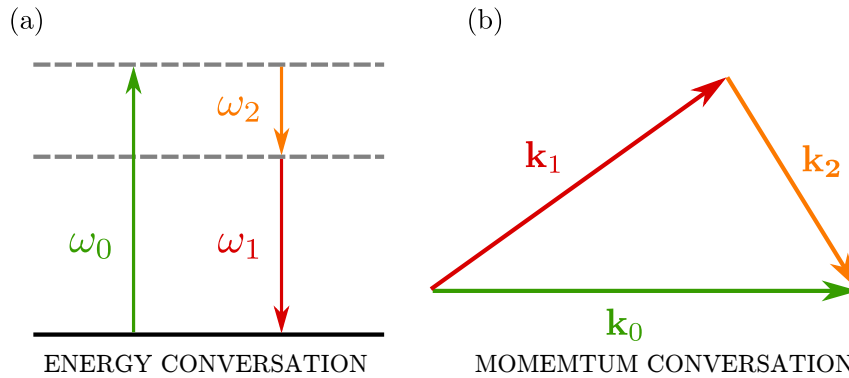


Figure C.1: Graphic representations of the phase matching in a three-wave mixing process. (a) Energy conservation, the gray dotted line represent virtual levels. No absorption/emission occur. (b) Momentum conservation.

C.1, we can see a visual representation of energy conservation and momentum in a three-wave mixing process, which we will discuss below. Imagine the situation where three waves, of frequencies  $\omega_0$ ,  $\omega_1$  and  $\omega_2$  propagating collinearly in a medium having second-order nonlinearity and nondispersive, such that for these waves:

$$\omega_0 = \omega_1 + \omega_2, \quad k_0 = k_1 + k_2. \quad (\text{C.0.12})$$

In a nondispersive medium, the phase-matching condition is automatically satisfied if  $\omega_0 = \omega_1 + \omega_2$  because the refractive index is the same for all three wavelengths. However, since all materials have dispersion effects, waves with different frequencies will have different refractive indexes leading to the general condition

$$\omega_0 = \omega_1 + \omega_2, \quad n_0\omega_0 = n_1\omega_1 + n_2\omega_2. \quad (\text{C.0.13})$$

These two conditions must be met simultaneously, one being independent of the other. In most cases, such a condition is challenging to be satisfied, and the birefringence of some anisotropic materials is used to compensate for the dispersion. Accurate control of refractive indexes can be achieved using light polarization, crystal orientation, or temperature control.

Consider a process of frequency-difference generation at the limit where the conversion efficiency is small and there are virtually no changes in the input fields. A wave  $\omega_0$  and another  $\omega_1$  focus on a nonlinear crystal with second-order nonlinear susceptibility. The fields  $\mathcal{E}_0$  and  $\mathcal{E}_1$  are considered constant and the equations (C.0.7) and (C.0.8) are disregarded. Only the equation (C.0.6) can be directly integrated

$$\mathcal{E}_2 = i \frac{\omega_2}{n_2 c} \chi^{(2)} \mathcal{E}_0 \mathcal{E}_1^* \int_0^L e^{i\Delta k z} dz = i 2 \frac{\omega_2}{n_2 c \Delta k} \chi^{(2)} \mathcal{E}_0 \mathcal{E}_1^* e^{i\Delta k z/2} \text{senc} \left( \frac{\Delta k L}{2} \right), \quad (\text{C.0.14})$$

where  $L$  is the length of the crystal. The intensity of the generated field is <sup>1</sup>

$$I_2 = \left( \frac{\omega_2 L}{n_2 c} \chi^{(2)} \right)^2 |\mathcal{E}_0|^2 |\mathcal{E}_1|^2 \text{senc}^2 \left( \frac{\Delta k L}{2} \right). \quad (\text{C.0.15})$$

In the expressions for the amplitude and intensity of the field, we see a beat with a periodicity and amplitude dependence on  $\Delta k$ . For the equation (C.0.15) the periodicity is  $2\pi\Delta k$  and defines the *coherence length*  $L_c$ , defined by

$$L_c \equiv \frac{\pi}{|\Delta k|}, \quad (\text{C.0.16})$$

<sup>1</sup>The sine cardinal function is defined as  $\text{senc}(x) \equiv \text{sen}(x)/x$ .



the coherence length becomes infinite when  $\Delta k \rightarrow 0$ . Clearly, the condition  $\Delta k = 0$  is the best possible case for choosing a set of input waves. The phase-matching dictates whether maximum efficiency is achievable and the system's tolerance to variables such as temperature.

### C.0.2 Quasi-phase matching

It is possible to achieve the phase matching condition efficiently without the use of birefringence. This technique is called quasi-phase matching (QPM). It was actually the first proposal to achieve phase matching in nonlinear crystals [155].

Basically, QPM techniques introduce a periodic shift in the phase of nonlinear polarization, maintaining the energy transfer between polarization and the fields generated by nonlinear interaction. As we have seen, if the phase-matching condition is not satisfied, periodic exchange of energy between the polarization and the generated fields takes place. The coherence length  $L_c$  is linked to the spatial period in which this exchange repeats. If the crystal is reoriented so that the phase of polarization is always reversed before the field strength decreases, it is possible to cause the intensity to increase continuously. Allowing the generation of intense fields without the use of birefringence.

Certain types of material reorientation alter their linear properties. However, operations such as inversion leave the materials' linear properties unchanged but lead to a change of sign in the nonlinear coefficient. Imagine that we have a crystal with second-order nonlinearity. Its nonlinear coefficient is a function of position and has the property of periodically inverting sign at a given length (see Figure C.2). Using the same example that we used to introduce the effects of phase matching, we consider two intense fields that remain essentially constant propagating in this crystal, again equation (C.0.11), however,  $\chi^{(2)} \rightarrow \chi^{(2)}(z)$ . We have

$$\frac{d\mathcal{E}_2}{dz} = i \frac{\omega_2}{n_2 c} \chi^{(2)}(z) \mathcal{E}_0 \mathcal{E}_1^* e^{i\Delta k}, \quad (\text{C.0.17})$$

which can be directly integrated

$$\mathcal{E}_2 = i \frac{\omega_2}{n_2 c} \mathcal{E}_0 \mathcal{E}_1^* \int_0^L \chi^{(2)}(z) e^{i\Delta k} dz. \quad (\text{C.0.18})$$

For such periodic structure, the function  $\chi^{(2)}(z)$  can be represented by a Fourier series of the form

$$\chi^{(2)}(z) = \chi \sum_m Q_m e^{-ik_m z}. \quad (\text{C.0.19})$$

Substituting the above expression into (C.0.18) we get

$$\mathcal{E}_2 = i \frac{\omega_2}{n_2 c} \mathcal{E}_0 \mathcal{E}_1^* \chi \sum_m Q_m \int_0^L e^{i(\Delta k - k_m) z} dz, \quad (\text{C.0.20})$$

and the parallel with what we have already seen about phase matching can be done by defining

$$\Delta k'_m \equiv \Delta k - k_m. \quad (\text{C.0.21})$$

That can be understood as a new term of phase matching. Since the coefficients  $Q_m$  do not depend on  $z$  it can be taken from the integral and the result obtained is

$$\mathcal{E}_2 = i \frac{\omega_2}{n_2 c} \mathcal{E}_0 \mathcal{E}_1^* \chi l \sum_m Q_m e^{i\Delta k'_m l/2} \text{senc}(\Delta k'_m l/2). \quad (\text{C.0.22})$$

Noting that only a value for  $m$  will return  $\Delta k'_m = 0$ , that is,

$$\Delta k'_m = \Delta k - \frac{2\pi}{\Lambda} m = 0, \quad (\text{C.0.23})$$

the sum of  $m$  can be eliminated as contributions to other  $m$  values will be small. Thus, the obtained result is the amplitude

$$\mathcal{E}_2 = i \frac{\omega_2}{n_2 c} \mathcal{E}_0 \mathcal{E}_1^* \chi l Q_m e^{i \Delta k'_m l / 2} \text{senc}(\Delta k'_m l / 2), \quad (\text{C.0.24})$$

which differs by a multiplication factor from the form found for the normal phase matching (with a phase matching  $\Delta k'_m$ ). For  $\Delta k'_m = 0$ , the generation of the  $\mathcal{E}_2$  field is efficient. In fact, a QPM structure leads to an amplitude reduced by a factor  $Q_m$  and intensity for a factor  $Q_m^2$  compared to (C.0.14), Figure C.2. It is easy to show that in a material in which the nonlinear coefficient is inverted

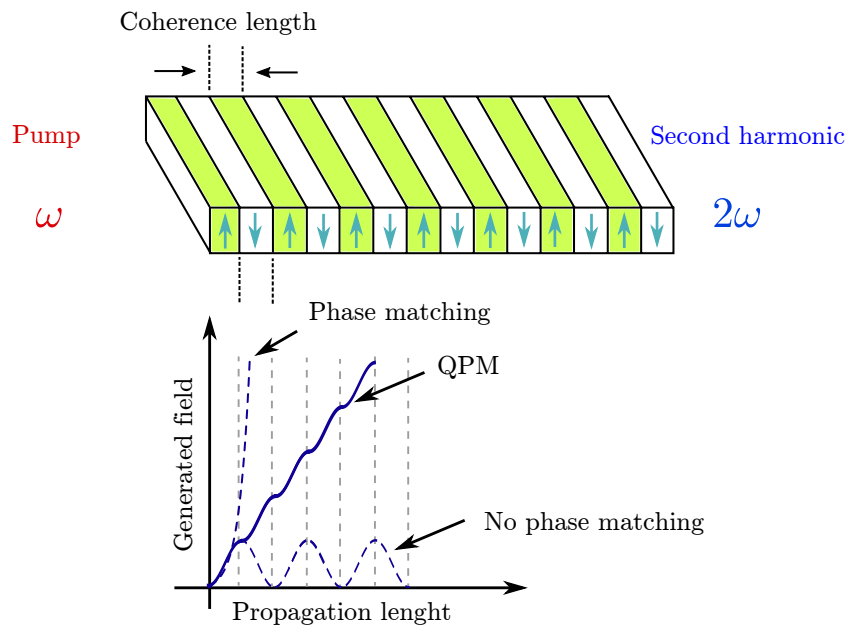


Figure C.2: Illustration of a crystal with QPM in a second harmonic generation process. The periodic inversion of the polarization vector in a coherence length makes the process efficient.

periodically for  $m = 1$  we have

$$\mathcal{E}_2 = \frac{2}{\pi} \mathcal{E}_2(\text{birrefringence}), \quad (\text{C.0.25})$$

and the periodicity required for QPM,  $\Delta k'_m = 0$ , will be

$$\Lambda = \frac{2\pi}{\Delta k} m. \quad (\text{C.0.26})$$

Any difficulty in using this technique lies in the correct construction of a “almost periodic” structure in the crystal. In principle, this enables any wave mixing process once the periodic structure can be implemented. As an example, consider the input waves propagating on the  $xy$  plane, with polarization in the direction of the  $z$ -axis, for a first-order quasi-phase matching ( $m = 1$ ), the required periodicity is given by

$$\Lambda = \frac{2\pi}{\Delta k} = \frac{1}{(n_{z0}/\lambda_0) - (n_{z1}/\lambda_1) - (n_{z2}/\lambda_2)}, \quad (\text{C.0.27})$$

where  $n_{iz}(\lambda_i) = n_i$  can be found by the Sellmeier equation [62].

## C.1 Kleinman–Boyd parameters

We saw that the conversion efficiency depends on the intensity of the pump beam. In practice, we have to take into account the finite transverse spatial extent of the wave. One can imagine that for a fixed input power more tightly confine the beam more efficient the process will be, but dealing with Gaussian beams more confinement means that it will more rapidly diffract. Consequently, the confinement can not be maintained over a long length decreasing the effective interaction length. In fact, there is an optimum waist size that is a compromise between confinement and interaction length. How to calculate this optimum spatial mode to improve the conversion efficiency is what we are going to discuss in this section.

Assuming that a fundamental Gaussian beam with field distribution  $e^{-r^2/w_0^2}$  is focused to a waist  $w_0$  at the center of a nonlinear medium, Kleinman and Boyd studied the optimum focusing for maximum efficiency [150]. The fundamental parameter that characterize the beam is  $b = 2\pi n w_0^2 / \lambda_p$ , where  $n$  is the refractive index of the crystal at pump wavelength  $\lambda_p$ . This imply in a divergent far-field angle  $\theta_0 = \lambda / \pi n w_0$ . Defining the parameters  $\xi \equiv l/b$  and  $B \equiv \rho \sqrt{\xi} / \theta_0$ , where  $l$  is the crystal length,  $\rho$  is the angle between the generated beams. For type-I phase matching the overall confinement effect is described by the function  $h_m(B, \xi)$ , Figure C.3 shows plots of  $h_m$  for various values of  $B$  in function of  $\xi$ . In the case of  $\rho = 0$  (our case), we need to consider only  $B = 0$  this is the no “walk-off” case. The maximum value  $h_m$  is achieved for  $B = 0$  and  $\xi = 2.84$  meaning that maximum conversion happens when the parameter  $b = l/2.84$ . The threshold power of a parametric process like OPO calculated to interacting Gaussian beams  $P_{th,G}$  is changed

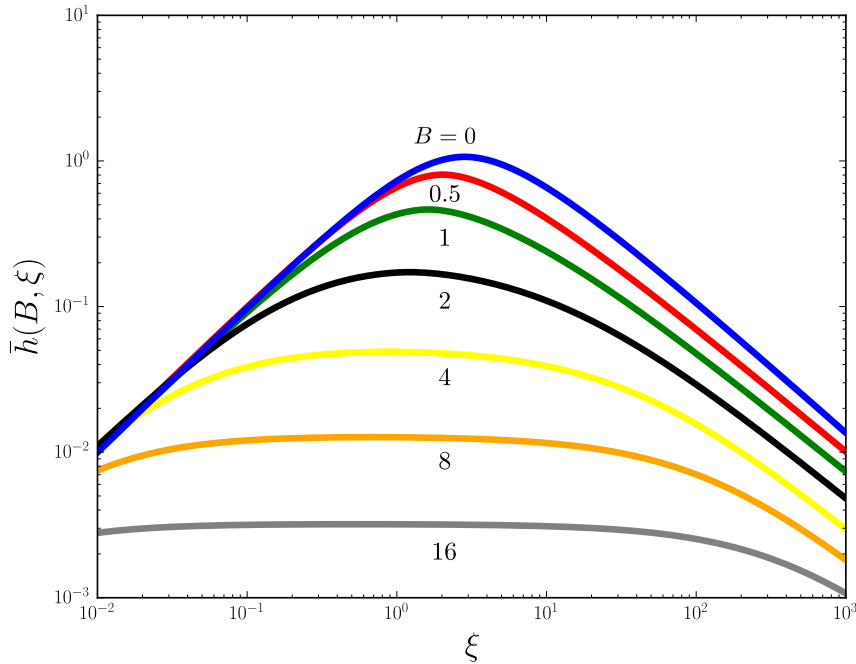


Figure C.3: Kleinman–Boyd function  $h_m(B, \xi)$  for different values of  $B$  as function of  $\xi$ .

$$P_{th,G} \longrightarrow P_{th,KB} = \frac{P_{th,G}}{h_m(B, \xi)}, \quad (\text{C.1.1})$$

where  $P_{th,G}$  is the real situation threshold. This is a convenient expression for making oscillation threshold real predictions. We can write analytic functions for the Kleinman–Boyd functions as described in [156] and insert it in the expressions for the OPO oscillation threshold in any pump focusing situation. )

# Bibliography

- [1] F. Ya Khalili and E. S. Polzik. Overcoming the Standard Quantum Limit in Gravitational Wave Detectors Using Spin Systems with a Negative Effective Mass. *Physical Review Letters*, 121(3):031101, jul 2018.
- [2] Y. Aharonov and D. Rohrlich. *Quantum Paradoxes: Quantum Theory for the Perplexed*. Physics textbook. Wiley, 2008.
- [3] C. Cohen-Tannoudji, B. Diu, and F. Laloë. *Quantum mechanics*. Quantum Mechanics. Wiley, 1977.
- [4] A. Einstein, B. Podolsky, and N. Rosen. Can Quantum-Mechanical Description of Physical Reality Be Considered Complete? *Physical Review*, 47(10):777–780, May 1935.
- [5] David Bohm. A suggested interpretation of the quantum theory in terms of "hidden" variables. I. *Physical Review*, 85(2):166–179, jan 1952.
- [6] J. S. Bell. On the Einstein-Podolsky-Rosen paradox. *Physica Physique Fizika*, 1:195–200, 1964.
- [7] Nicolas Brunner, Daniel Cavalcanti, Stefano Pironio, Valerio Scarani, and Stephanie Wehner. Bell nonlocality. *Reviews of Modern Physics*, 86(2):419–478, apr 2014.
- [8] J. F. Clauser and Abner Shimony. Bell's theorem. Experimental tests and implications. *Reports on Progress in Physics*, 41(12):1881–1927, dec 1978.
- [9] Alain Aspect, Philippe Grangier, and Gérard Roger. Experimental tests of realistic local theories via Bell's theorem. *Physical Review Letters*, 47(7):460–463, aug 1981.
- [10] Z. Y. Ou and L. Mandel. Violation of bell's inequality and classical probability in a two-photon correlation experiment. *Physical Review Letters*, 61(1):50–53, jul 1988.
- [11] B. Hensen, H. Bernien, A. E. Dreaú, A. Reiserer, N. Kalb, M. S. Blok, J. Ruitenberg, R. F.L. Vermeulen, R. N. Schouten, C. Abellán, W. Amaya, V. Pruneri, M. W. Mitchell, M. Markham, D. J. Twitchen, D. Elkouss, S. Wehner, T. H. Taminau, and R. Hanson. Loophole-free Bell inequality violation using electron spins separated by 1.3 kilometres. *Nature*, 526(7575):682–686, oct 2015.
- [12] Ribordy G. Gisin, N., W. Tittel, and H. Zbinden. Quantum Cryptography. *Rev. Mod. Phys.*, 74(January):145, 2002.
- [13] S. Pirandola, J. Eisert, C. Weedbrook, A. Furusawa, and S. L. Braunstein. Advances in quantum teleportation. *Nature Photonics*, 9(10):641–652, 2015.
- [14] M. A. Nielsen and I. L. Chuang. *Quantum Computation and Quantum Information: 10th Anniversary Edition*. Cambridge University Press, 2010.

- [15] Vittorio Giovannetti, Seth Lloyd, and Lorenzo MacCone. Advances in quantum metrology. *Nature Photonics*, 5(4):222–229, 2011.
- [16] Sheng Kai Liao, Wen Qi Cai, Wei Yue Liu, Liang Zhang, Yang Li, Ji Gang Ren, Juan Yin, Qi Shen, Yuan Cao, Zheng Ping Li, Feng Zhi Li, Xia Wei Chen, Li Hua Sun, Jian Jun Jia, Jin Cai Wu, Xiao Jun Jiang, Jian Feng Wang, Yong Mei Huang, Qiang Wang, Yi Lin Zhou, Lei Deng, Tao Xi, Lu Ma, Tai Hu, Qiang Zhang, Yu Ao Chen, Nai Le Liu, Xiang Bin Wang, Zhen Cai Zhu, Chao Yang Lu, Rong Shu, Cheng Zhi Peng, Jian Yu Wang, and Jian Wei Pan. Satellite-to-ground quantum key distribution. *Nature*, 549(7670):43–47, 2017.
- [17] Sheng Kai Liao, Wen Qi Cai, Johannes Handsteiner, Bo Liu, Juan Yin, Liang Zhang, Dominik Rauch, Matthias Fink, Ji Gang Ren, Wei Yue Liu, Yang Li, Qi Shen, Yuan Cao, Feng Zhi Li, Jian Feng Wang, Yong Mei Huang, Lei Deng, Tao Xi, Lu Ma, Tai Hu, Li Li, Nai Le Liu, Franz Koidl, Peiyuan Wang, Yu Ao Chen, Xiang Bin Wang, Michael Steindorfer, Georg Kirchner, Chao Yang Lu, Rong Shu, Rupert Ursin, Thomas Scheidl, Cheng Zhi Peng, Jian Yu Wang, Anton Zeilinger, and Jian Wei Pan. Satellite-Relayed Intercontinental Quantum Network. *Physical Review Letters*, 120(3):30501, 2018.
- [18] P. W. Shor. Algorithms for quantum computation: discrete logarithms and factoring. In *Proceedings 35th Annual Symposium on Foundations of Computer Science*, pages 124–134, 1994.
- [19] T. E. Northup and R. Blatt. Quantum information transfer using photons. *Nature Photonics*, 8(5):356–363, April 2014.
- [20] H J Kimble. The quantum internet. *Nature*, 453(7198):1023–30, June 2008.
- [21] A. Furusawa and P. van Loock. *Quantum Teleportation and Entanglement: A Hybrid Approach to Optical Quantum Information Processing*. Wiley, 2011.
- [22] Ulrik L. Andersen, Jonas S. Neergaard-Nielsen, Peter Van Loock, and Akira Furusawa. Hybrid discrete- and continuous-variable quantum information. *Nature Physics*, 11(9):713–719, sep 2015.
- [23] D. F. Walls and G. J. Milburn. *Quantum Optics*. Springer, 2008.
- [24] Zweizig J. Buikema, A. [...]. Sensitivity and performance of the Advanced LIGO detectors in the third observing run. *Physical Review D*, 102(6):62003, 2020.
- [25] V.B. Braginsky, F.Y. Khalili, and K.S. Thorne. *Quantum Measurement*. Cambridge University Press, 1992.
- [26] Carlton M. Caves. Quantum-mechanical radiation-pressure fluctuations in an interferometer. *Physical Review Letters*, 45(2):75–79, jul 1980.
- [27] Rodney Loudon. Quantum limit on the michelson interferometer used for gravitational-wave detection. *Physical Review Letters*, 47(12):815–818, sep 1981.
- [28] Emil Zeuthen, Eugene S. Polzik, and Farid Ya Khalili. Gravitational wave detection beyond the standard quantum limit using a negative-mass spin system and virtual rigidity. *Physical Review D*, 100(6):062004, sep 2019.
- [29] Christoffer B. Møller, Rodrigo A. Thomas, Georgios Vasilakis, Emil Zeuthen, Yeghishe Tsaturyan, Mikhail Balabas, Kasper Jensen, Albert Schliesser, Klemens Hammerer, and Eugene S. Polzik. Quantum back-Action-evading measurement of motion in a negative mass reference frame. *Nature*, 547(7662):191–195, 2017.

- [30] W. K. Wootters and W. H. Zurek. A single quantum cannot be cloned. *Nature*, 299(5886):802–803, 1982.
- [31] L. M. Duan, M. D. Lukin, J. I. Cirac, and P. Zoller. Long-distance quantum communication with atomic ensembles and linear optics. *Nature*, 414(6862):413–418, 2001.
- [32] Nicolas Sangouard, Christoph Simon, Hugues de Riedmatten, and Nicolas Gisin. Quantum repeaters based on atomic ensembles and linear optics. *Reviews of Modern Physics*, 83(1):33–80, mar 2011.
- [33] Klemens Hammerer, Anders S. Sørensen, and Eugene S. Polzik. Quantum interface between light and atomic ensembles. *Reviews of Modern Physics*, 82(2):1041–1093, apr 2010.
- [34] Jianwei Wang, Fabio Sciarrino, Anthony Laing, and Mark G. Thompson. Integrated photonic quantum technologies. *Nature Photonics*, 14(5):273–284, 2020.
- [35] Ali W. Elshaari, Wolfram Pernice, Kartik Srinivasan, Oliver Benson, and Val Zwiller. Hybrid integrated quantum photonic circuits. *Nature Photonics*, 14(5):285–298, 2020.
- [36] T. J. Kippenberg, S. M. Spillane, and K. J. Vahala. Kerr-nonlinearity optical parametric oscillation in an ultrahigh-Q toroid microcavity. *Physical Review Letters*, 93(8):18–21, 2004.
- [37] Mark A. Foster, Amy C. Turner, Jay E. Sharping, Bradley S. Schmidt, Michal Lipson, and Alexander L. Gaeta. Broad-band optical parametric gain on a silicon photonic chip. *Nature*, 441(7096):960–963, 2006.
- [38] P. Del’Haye, A. Schliesser, O. Arcizet, T. Wilken, R. Holzwarth, and T. J. Kippenberg. Optical frequency comb generation from a monolithic microresonator. *Nature*, 450(7173):1214–1217, 2007.
- [39] Jacob S. Levy, Alexander Gondarenko, Mark A. Foster, Amy C. Turner-Foster, Alexander L. Gaeta, and Michal Lipson. CMOS-compatible multiple-wavelength oscillator for on-chip optical interconnects. *Nature Photonics*, 4(1):37–40, 2010.
- [40] L. Razzari, D. Duchesne, M. Ferrera, R. Morandotti, S. Chu, B. E. Little, and D. J. Moss. CMOS-compatible integrated optical hyper-parametric oscillator. *Nature Photonics*, 4(1):41–45, 2010.
- [41] Xingchen Ji, Felipe A. S. Barbosa, Samantha P. Roberts, Avik Dutt, Jaime Cardenas, Yoshitomo Okawachi, Alex Bryant, Alexander L. Gaeta, and Michal Lipson. Ultra-low-loss on-chip resonators with sub-milliwatt parametric oscillation threshold. *Optica*, 4(6):619, 2017.
- [42] N. Bohr. Can Quantum-Mechanical Description of Physical Reality be Considered Complete? *Physical Review*, 48(8):696–702, October 1935.
- [43] Otfried Gühne and Géza Tóth. Entanglement detection. *Physics Reports*, 474(1–6):1–75, April 2009.
- [44] Ryszard Horodecki, Michał Horodecki, and Karol Horodecki. Quantum entanglement. *Reviews of Modern Physics*, 81(2):865–942, June 2009.
- [45] P. van Loock and A. Furusawa. Detecting genuine multipartite continuous-variable entanglement. *Physical Review A*, 67(5):052315, May 2003.
- [46] Lu-Ming Duan, G. Giedke, J. I. Cirac, and P. Zoller. Inseparability Criterion for Continuous Variable Systems. *Physical Review Letters*, 84(12):2722–2725, March 2000.

- [47] R. Simon. Peres-horodecki separability criterion for continuous variable systems. *Physical review letters*, 84(12):2726–9, 2000.
- [48] M. D. Eisaman, J. Fan, A. Migdall, and S. V. Polyakov. Invited review article: Single-photon sources and detectors. *Review of Scientific Instruments*, 82(7):071101, 2011.
- [49] A. I. Lvovsky and M. G. Raymer. Continuous-variable optical quantum-state tomography. *Rev. Mod. Phys.*, 81:299–332, Mar 2009.
- [50] D. F. Walls. Squeezed states of light. *Nature*, 306(5939):141–146, 1983.
- [51] Gerd Leuchs. Squeezing the quantum fluctuations of light. *Contemporary Physics*, 29(3):299–314, 1988.
- [52] C. Fabre. Squeezed states of light. *Physics Reports*, 219(3-6):215–225, oct 1992.
- [53] H. Kimble. Squeezed states of light: an (incomplete) survey of experimental progress and prospects. *Physics Reports*, 219(3-6):227–234, oct 1992.
- [54] R. E. Slusher, L. W. Hollberg, B. Yurke, J. C. Mertz, and J. F. Valley. Observation of squeezed states generated by four-wave mixing in an optical cavity. *Physical Review Letters*, 55(22):2409–2412, nov 1985.
- [55] R. M. Shelby, M. D. Levenson, S. H. Perlmutter, R. G. Devoe, and D. F. Walls. Broad-band parametric deamplification of quantum noise in an optical fiber. *Physical Review Letters*, 57(6):691–694, aug 1986.
- [56] Carlton Caves. Quantum-mechanical noise in an interferometer. *Physical Review D*, 23(8):1693–1708, April 1981.
- [57] Min Xiao, Ling-An Wu, and H. J. Kimble. Precision measurement beyond the shot-noise limit. *Physical Review Letters*, 59(3):278–281, July 1987.
- [58] E. Wigner. On the Quantum Correction For Thermodynamic Equilibrium. *Physical Review*, 40(5):749–759, June 1932.
- [59] W. Schleich. *Quantum Optics in Phase Space*. Wiley-VCH, 2001.
- [60] Alessio Serafini. *Quantum Continuous Variables: A Primer of Theoretical Methods*. CRC Press, 2017.
- [61] Christian Weedbrook, Stefano Pirandola, Raúl García-Patrón, Nicolas J. Cerf, Timothy C. Ralph, Jeffrey H. Shapiro, and Seth Lloyd. Gaussian quantum information. *Reviews of Modern Physics*, 84(2):621–669, may 2012.
- [62] B. E. A. Saleh and M. C. Teich. *Fundamentals of Photonics*. Wiley Series in Pure and Applied Optics. Wiley, 2007.
- [63] Roy Glauber. The Quantum Theory of Optical Coherence. *Physical Review*, 130(6):2529–2539, June 1963.
- [64] L. Mandel and E. Wolf. *Optical Coherence and Quantum Optics*. Cambridge University Press, 1995.
- [65] H. A. Bachor and T. C. Ralph. *A Guide to Experiments in Quantum Optics*. Physics textbook. Wiley, 2004.

- [66] Ulf Leonhardt. Quantum physics of simple optical instruments. *Rep. Prog. Phys.*, 66:1207, 2003.
- [67] Charles H. Bennett, Gilles Brassard, Claude Crépeau, Richard Jozsa, Asher Peres, and William K. Wootters. Teleporting an unknown quantum state via dual classical and Einstein-Podolsky-Rosen channels. *Physical Review Letters*, 70(13):1895–1899, mar 1993.
- [68] S. Pirandola and S. Mancini. Quantum teleportation with continuous variables: A survey. *Laser Physics*, 16(10):1418–1438, oct 2006.
- [69] Sandu Popescu. Bell’s inequalities versus teleportation: What is nonlocality? *Physical Review Letters*, 72(6):797–799, 1994.
- [70] Mitsuyoshi Yukawa, Hugo Benichi, and Akira Furusawa. High-fidelity continuous-variable quantum teleportation toward multistep quantum operations. *Physical Review A - Atomic, Molecular, and Optical Physics*, 77(2):1–5, 2008.
- [71] Samuel L. Braunstein. Quantum information with continuous variables. *Reviews of Modern Physics*, 77(2):513–577, June 2005.
- [72] Christian Weedbrook, Stefano Pirandola, Raúl García-Patrón, Nicolas J. Cerf, Timothy C. Ralph, Jeffrey H. Shapiro, and Seth Lloyd. Gaussian quantum information. *Reviews of Modern Physics*, 84(2):621–669, May 2012.
- [73] W. H. Louisell, A. Yariv, and A. E. Siegman. Quantum fluctuations and noise in parametric processes. I. *Physical Review*, 124(6):1646–1654, dec 1961.
- [74] J. P. Gordon, W. H. Louisell, and L. R. Walker. Quantum fluctuations and noise in parametric processes. II. *Physical Review*, 129(1):481–485, jan 1963.
- [75] H. Takahasi. *Advances in communication systems*, volume 1. Academic Press, 1965.
- [76] B. R. Mollow and R. J. Glauber. Quantum theory of parametric amplification. I. *Physical Review*, 160(5):1076–1096, aug 1967.
- [77] B. R. Mollow and R. J. Glauber. Quantum theory of parametric amplification. II. *Physical Review*, 160(5):1097–1108, aug 1967.
- [78] G. Milburn and D. F. Walls. Production of squeezed states in a degenerate parametric amplifier. *Optics Communications*, 39(6):401–404, nov 1981.
- [79] K. J. McNeil and C. W. Gardiner. Quantum statistics of parametric oscillation. *Physical Review A*, 28(3):1560–1566, sep 1983.
- [80] Ling An Wu, H. J. Kimble, J. L. Hall, and Huifa Wu. Generation of squeezed states by parametric down conversion. *Physical Review Letters*, 57(20):2520–2523, nov 1986.
- [81] A. Heidmann, R. J. Horowicz, S. Reynaud, E. Giacobino, C. Fabre, and G. Camy. Observation of quantum noise reduction on twin laser beams. *Physical Review Letters*, 59(22):2555–2557, nov 1987.
- [82] M. D. Reid and P. D. Drummond. Quantum Correlations of Phase in Nondegenerate Parametric Oscillation. *Physical Review Letters*, 60(26):2731–2733, jun 1988.
- [83] M. D. Reid. Demonstration of the Einstein-Podolsky-Rosen paradox using nondegenerate parametric amplification. *Physical Review A*, 40(2):913–923, 1989.



- [84] M. D. Reid and P. D. Drummond. Correlations in nondegenerate parametric oscillation: Squeezing in the presence of phase diffusion. *Physical Review A*, 40(8):4493–4506, oct 1989.
- [85] P. D. Drummond and M. D. Reid. Correlations in nondegenerate parametric oscillation. II. below threshold results. *Physical Review A*, 41(7):3930–3949, apr 1990.
- [86] Z. Y. Ou, S. F. Pereira, and H. J. Kimble. Realization of the Einstein–Podolsky–Rosen paradox for continuous variables in nondegenerate parametric amplification. *Applied Physics B Photophysics and Laser Chemistry*, 55(3):265–278, sep 1992.
- [87] Z. Y. Ou, S. F. Pereira, H. J. Kimble, and K. C. Peng. Realization of the Einstein–Podolsky–Rosen paradox for continuous variables. *Physical Review Letters*, 68(25):3663–3666, jun 1992.
- [88] F. Kaiser, B. Fedrici, A. Zavatta, V. D’Auria, and S. Tanzilli. A fully guided-wave squeezing experiment for fiber quantum networks. *Optica*, 3(4):362, apr 2016.
- [89] M. Stefszky, R. Ricken, C. Eigner, V. Quiring, H. Herrmann, and C. Silberhorn. Waveguide Cavity Resonator as a Source of Optical Squeezing. *Physical Review Applied*, 7(4):044026, apr 2017.
- [90] F. Mondain, T. Lunghi, A. Zavatta, E. Gouzien, F. Dautre, M. de Micheli, S. Tanzilli, and V. D’Auria. Chip-based squeezing at a telecom wavelength. *Photonics Research*, 7(7):36–39, 2019.
- [91] Takahiro Kashiwazaki, Naoto Takanashi, Taichi Yamashima, Takushi Kazama, Koji Enbutsu, Ryoichi Kasahara, Takeshi Umeki, and Akira Furusawa. Continuous-wave 6-dB-squeezed light with 2.5-THz-bandwidth from single-mode PPLN waveguide. *APL Photonics*, 5(3):036104, mar 2020.
- [92] Avik Dutt, Kevin Luke, Sasikanth Manipatruni, Alexander L. Gaeta, Paulo Nussenzveig, and Michal Lipson. On-Chip Optical Squeezing. *Physical Review Applied*, 3(4):044005, apr 2015.
- [93] V. D. Vaidya, B. Morrison, L. G. Helt, R. Shahrokhshahi, D. H. Mahler, M. J. Collins, K. Tan, J. Lavoie, A. Repingon, M. Menotti, N. Quesada, R. C. Pooser, A. E. Lita, T. Gerrits, S. W. Nam, and Z. Vernon. Broadband quadrature-squeezed vacuum and nonclassical photon number correlations from a nanophotonic device. *Science Advances*, 6(39):eaba9186, sep 2020.
- [94] Yun Zhao, Yoshitomo Okawachi, Jae K. Jang, Xingchen Ji, Michal Lipson, and Alexander L. Gaeta. Near-Degenerate Quadrature-Squeezed Vacuum Generation on a Silicon-Nitride Chip. *Physical Review Letters*, 124(19):193601, may 2020.
- [95] J. U. Fürst, D. V. Strekalov, D. Elser, A. Aiello, U. L. Andersen, Ch Marquardt, and G. Leuchs. Low-threshold optical parametric oscillations in a whispering gallery mode resonator. *Physical Review Letters*, 105(26):263904, dec 2010.
- [96] J. U. Fürst, D. V. Strekalov, D. Elser, A. Aiello, U. L. Andersen, Ch Marquardt, and G. Leuchs. Quantum Light from a Whispering-Gallery-Mode Disk Resonator. *Physical Review Letters*, 106(11):113901, mar 2011.
- [97] Dmitry V. Strekalov, Christoph Marquardt, Andrey B. Matsko, Harald G.L. Schwefel, and Gerd Leuchs. Nonlinear and quantum optics with whispering gallery resonators. *Journal of Optics*, 18(12):123002, dec 2016.

- [98] Alexander Otterpohl, Florian Sedlmeir, Ulrich Vogl, Thomas Dirmeier, Golnoush Shafiee, Gerhard Schunk, Dmitry V. Strekalov, Harald G. L. Schwefel, Tobias Gehring, Ulrik L. Andersen, Gerd Leuchs, and Christoph Marquardt. Squeezed vacuum states from a whispering gallery mode resonator. *Optica*, 6(11):1375, nov 2019.
- [99] A. S. Villar, L. S. Cruz, K. N. Cassemiro, M. Martinelli, and P. Nussenzveig. Generation of bright two-color continuous variable entanglement. *Physical Review Letters*, 95(24):243603, dec 2005.
- [100] A. S. Coelho, F. A. S. Barbosa, K. N. Cassemiro, A S Villar, M. Martinelli, and P. Nussenzveig. Three-color entanglement. *Science (New York, N.Y.)*, 326(5954):823–6, November 2009.
- [101] Luis F. Muñoz-Martínez, Felipe Alexandre Silva Barbosa, Antônio Sales Coelho, Luis Ortiz-Gutiérrez, Marcelo Martinelli, Paulo Nussenzveig, and Alessandro S. Villar. Exploring six modes of an optical parametric oscillator. *Physical Review A*, 98(2):023823, aug 2018.
- [102] F. A. S. Barbosa, A. S. Coelho, L. F. Muñoz-Martínez, L. Ortiz-Gutiérrez, A. S. Villar, P. Nussenzveig, and M. Martinelli. Hexapartite Entanglement in an above-Threshold Optical Parametric Oscillator. *Physical Review Letters*, 121(7):073601, aug 2018.
- [103] Hans J. Briegel and Robert Raussendorf. Persistent entanglement in arrays of interacting particles. *Phys. Rev. Lett.*, 86:910–913, Jan 2001.
- [104] Moran Chen, Nicolas C. Menicucci, and Olivier Pfister. Experimental realization of multipartite entanglement of 60 modes of a quantum optical frequency comb. *Phys. Rev. Lett.*, 112:120505, Mar 2014.
- [105] Jun-ichi Yoshikawa, Shota Yokoyama, Toshiyuki Kaji, Chanond Sornphiphatphong, Yu Shiozawa, Kenzo Makino, and Akira Furusawa. Invited article: Generation of one-million-mode continuous-variable cluster state by unlimited time-domain multiplexing. *APL Photonics*, 1(6):060801, 2016.
- [106] C. Gardiner and P. Zoller. *Quantum Noise: A Handbook of Markovian and Non-Markovian Quantum Stochastic Methods with Applications to Quantum Optics*. Springer Series in Synergetics. Springer, 2010.
- [107] Marcelo Martinelli. *Emaranhamento em Variáveis Contínuas, Morte Súbita, e Além*. Tese de livre-docência, Universidade de São Paulo, 2011.
- [108] Alessandro S. Villar, Katiúscia N. Cassemiro, Kaled Dechoum, Antonio Z. Khoury, Marcelo Martinelli, and Paulo Nussenzveig. Entanglement in the above-threshold optical parametric oscillator. *Journal of the Optical Society of America B*, 24(2):249, 2007.
- [109] Serge Reynaud and Antoine Heidmann. A semiclassical linear input output transformation for quantum fluctuations. *Optics Communications*, 71(3-4):209–214, May 1989.
- [110] C. Fabre, E. Giacobino, A. Heidmann, L. Lugiato, S. Reynaud, M. VDACCHINO, and Wang Kaige. Squeezing in detuned degenerate optical parametric oscillators. *Quantum Optics: Journal of the European Optical Society Part B*, 2(2):159–187, April 1990.
- [111] A. S. Villar, M. Martinelli, and P. Nussenzveig. Testing the entanglement of intense beams produced by a non-degenerate optical parametric oscillator. 242:551–563, 2004.
- [112] Marcelo Martinelli. *Compressão de ruído quântico e efeitos transversos em osciladores paramétricos óticos*. Tese de doutorado, Universidade de São Paulo, 2002.

- [113] Alessandro De Sousa Villar. *Estudo de Emaranhamento no oscilado paramétrico ótico Não-degenerado acima do limiar*. Dissertação de mestrado, Universidade de São Paulo, 2004.
- [114] T. Debuisschert, A. Sizmann, E. Giacobino, and C. Fabre. Type-II continuous-wave optical parametric oscillators oscillation and frequency-tuning characteristics. *Journal of the Optical Society of America B*, 10(9):1668, September 1993.
- [115] G. Jiangrui K. Kasai and C. Fabre. Observation of squeezing using cascaded nonlinearity. *Europhysics Letters (EPL)*, 40(1):25–30, October 1997.
- [116] A. S. Villar, M. Martinelli, C. Fabre, and P. Nussenzveig. Direct Production of Tripartite Pump-Signal-Idler Entanglement in the Above-Threshold Optical Parametric Oscillator. *Physical Review Letters*, 97(14):140504, October 2006.
- [117] E. G. Cavalcanti, S. J. Jones, H. M. Wiseman, and M. D. Reid. Experimental criteria for steering and the einstein-podolsky-rosen paradox. *Physical Review A - Atomic, Molecular, and Optical Physics*, 80(3):1–16, 2009.
- [118] P. Hyllus and J. Eisert. Optimal entanglement witnesses for continuous-variable systems. *New Journal of Physics*, 8(4):51, 2006.
- [119] R. Y. Teh and M. D. Reid. Criteria for genuine N -partite continuous-variable entanglement and Einstein-Podolsky-Rosen steering. *Physical Review A - Atomic, Molecular, and Optical Physics*, 90(6):1–17, 2014.
- [120] Natalia Korolkova, Gerd Leuchs, Rodney Loudon, Timothy C. Ralph, and Christine Silberhorn. Polarization squeezing and continuous-variable polarization entanglement. *Physical Review A - Atomic, Molecular, and Optical Physics*, 65(5):523061–5230612, 2002.
- [121] Alfredo Luis and Natalia Korolkova. Polarization squeezing and nonclassical properties of light. *Physical Review A - Atomic, Molecular, and Optical Physics*, 74(4):1–7, 2006.
- [122] Alfredo Luis. Chapter five - polarization in quantum optics. volume 61 of *Progress in Optics*, pages 283 – 331. Elsevier, 2016.
- [123] J. César, A. Coelho, K. Cassemiro, A. Villar, M. Lassen, P. Nussenzveig, and M. Martinelli. Extra phase noise from thermal fluctuations in nonlinear optical crystals. *Physical Review A*, 79(6):063816, June 2009.
- [124] K. N. Cassemiro, A. S. Villar, M. Martinelli, and P. Nussenzveig. The quest for three-color entanglement: experimental investigation of new multipartite quantum correlations. *Optics Express*, 15(26):18236, dec 2007.
- [125] C. Kittel. *Introduction to Solid State Physics*. Wiley, 2004.
- [126] R. W. Boyd. *Nonlinear Optics*. Nonlinear Optics Series. Elsevier Science, 2008.
- [127] A. E. Siegman. *Lasers*. University Science Books, 1986.
- [128] R. M. Shelby, M. D. Levenson, and P. W. Bayer. Resolved forward Brillouin scattering in optical fibers. *Physical Review Letters*, 54(9):939–942, mar 1985.
- [129] R. M. Shelby, M. D. Levenson, and P. W. Bayer. Guided acoustic-wave Brillouin scattering. *Physical Review B*, 31(8):5244–5252, apr 1985.

- [130] Nicolai B. Grosse. *Harmonic entanglement & photon anti-bunching*. PhD thesis, Australian National University, 2009.
- [131] Alistair J. Poustie. Bandwidth and mode intensities of guided acoustic-wave Brillouin scattering in optical fibers. *Journal of the Optical Society of America B*, 10(4):691, apr 1993.
- [132] Rayssa Bruzaca de Andrade. *An optical parametric oscillator for a light-atomic media interface*. PhD thesis, University of São Paulo, 2018.
- [133] Christian Schori, Jens L. Sørensen, and Eugene S. Polzik. Narrow-band frequency tunable light source of continuous quadrature entanglement. *Phys. Rev. A*, 66:033802, Sep 2002.
- [134] S. F. Pereira Z. Y. Ou and H. J. Kimble. Realization of the einstein-podolsky-rosen paradox for continuous variables in nondegenerate parametric amplification. *Appl. Phys. B*, 55:265–278, 1992.
- [135] E. Oelker, G. Mansell, M. Tse, J. Miller, F. Matichard, L. Barsotti, P. Fritschel, D. E. McClelland, M. Evans, and N. Mavalvala. Ultra-low phase noise squeezed vacuum source for gravitational wave detectors. *Optica*, 3(7):682, jul 2016.
- [136] Henning Vahlbruch, Moritz Mehmet, Karsten Danzmann, and Roman Schnabel. Detection of 15 dB Squeezed States of Light and their Application for the Absolute Calibration of Photoelectric Quantum Efficiency. *Physical Review Letters*, 117(11):110801, sep 2016.
- [137] Kirk McKenzie, Nicolai Grosse, Warwick P. Bowen, Stanley E. Whitcomb, Malcolm B. Gray, David E. McClelland, and Ping Koy Lam. Squeezing in the audio gravitational-wave detection band. *Physical Review Letters*, 93(16):161105, oct 2004.
- [138] Henning Vahlbruch, Simon Chelkowski, Boris Hage, Alexander Franzen, Karsten Danzmann, and Roman Schnabel. Coherent control of vacuum squeezing in the gravitational-wave detection band. *Physical Review Letters*, 97(1):011101, jul 2006.
- [139] Simon Chelkowski, Henning Vahlbruch, Karsten Danzmann, and Roman Schnabel. Coherent control of broadband vacuum squeezing. *Physical Review A - Atomic, Molecular, and Optical Physics*, 75(4):043814, apr 2007.
- [140] Zweizig J. Abadie, [...]. A gravitational wave observatory operating beyond the quantum shot-noise limit. *Nature Physics*, 7(12):962–965, 2011.
- [141] Zweizig J. Aasi, [...]. Enhanced sensitivity of the LIGO gravitational wave detector by using squeezed states of light. *Nature Photonics*, 7(8):613–619, 2013.
- [142] H. Grote, K. Danzmann, K. L. Dooley, R. Schnabel, J. Slutsky, and H. Vahlbruch. First long-term application of squeezed states of light in a gravitational-wave observatory. *Physical Review Letters*, 110(18):181101, may 2013.
- [143] Danzmann Karsten Acernese, F. [...]. Increasing the Astrophysical Reach of the Advanced Virgo Detector via the Application of Squeezed Vacuum States of Light. *Physical Review Letters*, 123(23):231108, dec 2019.
- [144] Zweizig J. Tse, M. [...]. Quantum-Enhanced Advanced LIGO Detectors in the Era of Gravitational-Wave Astronomy. *Physical Review Letters*, 123(23):231107, dec 2019.
- [145] Inc. Coherent. Mephisto lasers – ultra-low noise and narrow linewidth. [https://www.coherent.com/assets/pdf/COHR\\_MephistoNPRO\\_WP\\_9\\_24\\_19.pdf](https://www.coherent.com/assets/pdf/COHR_MephistoNPRO_WP_9_24_19.pdf).

- [146] Nufern. 1064 - 1110 nm single frequency, pm, fiber amplifiers. [http://www.nufern.com/filestorage/fiber\\_amplifiers/PSFA-1064~1084~1100-%D0%A5\\_spec.pdf?6039](http://www.nufern.com/filestorage/fiber_amplifiers/PSFA-1064~1084~1100-%D0%A5_spec.pdf?6039).
- [147] Arlee Smith. Snlo free version. <https://as-photonics.com/products/snlo/>.
- [148] Gerald T. Moore. Resonant sum-frequency generation. *IEEE Journal of Quantum Electronics*, 38(1):12–18, jan 2002.
- [149] W. P. Risk, T. R. Gosnell, and A. V. Nurmikko. *Compact Blue-Green Lasers*. Cambridge University Press, 2003.
- [150] G. D. Boyd. Parametric Interaction of Focused Gaussian Light Beams. *Journal of Applied Physics*, 39(8):3597, November 1968.
- [151] R. W.P. Drever, J. L. Hall, F. V. Kowalski, J. Hough, G. M. Ford, A. J. Munley, and H. Ward. Laser phase and frequency stabilization using an optical resonator. *Applied Physics B Photophysics and Laser Chemistry*, 31(2):97–105, 1983.
- [152] Eric D. Black. An introduction to Pound–Drever–Hall laser frequency stabilization. *American Journal of Physics*, 69(1):79–87, 2001.
- [153] L. Neuhaus. Pyrpl (python redpitaya lockbox). <https://github.com/lneuhaus/pyrpl>.
- [154] H. Kogelnik and T. Li. Laser beams and resonators. *Applied optics*, 5(10):1550–67, October 1966.
- [155] J. Armstrong, N. Bloembergen, J. Ducuing, and P. Pershan. Interactions between Light Waves in a Nonlinear Dielectric. *Physical Review*, 127(6):1918–1939, sep 1962.
- [156] Y. F. Chen and Y. C. Chen. Analytical functions for the optimization of second-harmonic generation and parametric generation by focused Gaussian beams. *Applied Physics B*, 76(6):645–647, 2003.